Pulse shape discrimination studies in a liquid Argon scintillation detector

This diploma thesis has been carried out by Tina Pollmann at the
Max-Planck-Institut für Kernphysik
under the supervision of
Prof. Dr. Wolfgang Hampel

Abstract

Liquid rare gases have been gaining popularity as detector media in rare event searches, especially dark matter experiments, and one factor driving their adoption is the possibility to recognise different types of ionizing radiation by the pulse shapes they evoke. This work on pulse shape discrimination in a liquid argon scintillation detector was done in the framework of the GERDA experiment, where liquid argon scintillation signals may be used for background suppression purposes.

Liquid argon scintillation signals were measured using the LArGe@MPI-K setup and in addition, signals were simulated by Monte Carlo methods. Two discrimination algorithms, the "fast to total" and the Gatti filter, are tested on both experimental and simulated pulse shapes with respect to the discrimination power they afford. The discrimination power between photon and neutron induced events achieved with the "fast to total" filter on simulated pulse shapes with 70 detected photons is $2.5 \cdot 10^{-6}$ at over 99% acceptance, while on the measured pulse shapes at a threshold of 72 photo electrons a discrimination power of $\leqslant 4.3{\cdot}10^{-4}$ was achieved at more than 85% acceptance.

The light yield, pulse shapes and discrimination power in xenon doped argon are also studied. A theoretical model describing the pulse shape changes is developed and evidence is found that xenon is not distributed homogeneously in the liquid argon.

Zusammenfassung

Flüssige Edelgase werden als Detektormedien in Experimenten, die nach seltenen Ereignissen suchen, immer populärer. Die Möglichkeit verschiedene Arten ionisierender Strahlung anhand ihrer Pulsformen zu erkennen ist ein wichtiger Grund dafür. Diese Arbeit über Pulsformanalyse in einem flüssig-Argon Szintillationsdetektor wurde im Rahmen des GERDA Experimentes durchgeführt, wo flüssig-Argon Scintillationssignale möglicherweise zur Untegrundunterdrückung verwendet werden.

Flüssig-Argon Szintillationssignale wurden mit dem LArGe@MPI-K Versuchsaufbau gemessen, und darüberhinaus wurden Signale mit Hilfe von Monte Carlo Methoden simuliert. Zwei Diskriminationsalgorithmen, der "schnell zu gesamt" und der Gatti Filter, wurden sowohl an den gemessenen als auch an den simulierten Pulsformen getested, im Hinblick darauf wie gut sie die Pulse trennen können. Zwischen Photon- und Neutroninduzierten Pulsen wurde bei 70 detektierten Photonen eine Diskriminationskraft von $2.5 \cdot 10^{-6}$ gefunden, bei einer Akzeptanz von über 99%. Bei den gemessenen Pulsen ab einer Schwelle von 72 Photoelectronen wurde mit über 85% Akzeptanz eine Diskriminationskraft von $\leqslant 4.3{\cdot}10^{-4}$ erreicht.

Lichtausbeute, Pulseformen und Diskriminationskraft in mit Xenon gedoptem Argon wurden auch untersucht. Ein theoretisches Modell zur Beschreibung der Veränderung der Pulseformen wurde entwickelt und Hinweise dafür, dass Xenon sich nicht homogen im Detektor verteilte, wurden gefunden.

Contents

Chapter 1

Introduction

Non-accelerator particle-physics experiments have been gaining importance for the study of fundamental particles and processes, as reaching higher energies with accelerators is becoming increasingly difficult and naturally occurring processes provide insight into energy regions not currently or in the near future reached with particle accelerators. Prominent examples are the solar[10], atmospheric and reactor neutrino experiments[7] through which it could be established that neutrinos have a mass.

Non-accelerator experiments typically search for very rare events and thus require an ultra-low background level. If the events of interest additionally deposit very little energy in a detector, as is the case with dark-matter searches, the requirements on the background level are even stricter.

In this work, the possibility of background analysis and reduction by pulse shape analysis of liquid argon scintillation signals is studied by Monte Carlo simulation as well as by experiment. How good a discrimination power is achievable does not only depend on inherent properties of the scintillation signals, but also on the algorithm used to differentiate between them. Therefore, two different algorithms are studied and their performances compared. The properties of the pulse shapes themselves were altered by doping the liquid argon with small amounts of xenon, and the discrimination power in the modified scintillator is also investigated.

The work was done in the framework of the GERDA (GERmanium Detector Array) experiment, which is designed to search for the neutrinoless double beta decay ($0\nu\beta\beta$) in ^{76}Ge and which is a prime example for a rare event search neutrino experiment. The studies performed are however not specific to the requirements of the GERDA experiment, but are of general interest when considering liquid argon as a shield or as the detector medium in a rare-event search experiment.

The following section will give an overview over the role double beta decay plays in studying neutrino properties, and how liquid argon plays a role in the GERDA experiment. Afterwards, the dark matter problem and the advantages and challenges of using liquid argon as a detector medium for dark matter experiments are reviewed.

1.1 Double beta decay

The search for neutrinoless double beta decay is motivated by theoretical predictions concerning the nature of the neutrino. Most extensions to the Standard Model of particle physics require the neutrino to be a so called Majorana particle, which among other things means that it is identical to its own anti-particle. The observation of neutrinoless double beta decay would directly prove this to be the case and clear the path to extend the current Standard Model of particle physics, which is already known to be incomplete. (For further reading about neutrino properties see for example ref.[17, 14], and for double beta decay ref.[3].)

Double beta decay and neutrino properties The process equation for a regular beta decay is

$$(A, Z) \rightarrow (A, Z + 1) + e^{-} + \overline{\nu}_e. \tag{1.1}$$

This decay can take place whenever the original nucleus (A,Z) has a smaller binding energy than the daughter nucleus (A, Z+1). The daughter nucleus can itself undergo beta decay if the binding energy of the new daughter nucleus (A, Z+2) is higher yet. These transitions happen between isobaric nuclei. In the case where A is even, it can happen that the decay to (A, Z+1) is energetically forbidden; the nuclei can then with a very small probability still decay directly to (A, Z+2) by two neutrino double beta decay:

$$(A, Z) \rightarrow (A, Z + 2) + 2e^{-} + 2\overline{\nu}_e. \tag{1.2}$$

This means that two nucleons from (A, Z) decay at the same time but independently of each other. This kind of decay is allowed by the rules of the Standard Model and has been observed for the following isotopes[17]:

- ^{48}Ca, ^{76}Ge, ^{82}Se, ^{96}Zr, ^{100}Mo, ^{116}Cd, ^{128}Te, ^{130}Te, ^{150}Nd and ^{238}U

In the Standard Model of particle physics neutrinos are considered as mass-less left-handed Dirac particles. However, from neutrino oscillations we already know that they posses a mass and adding a mass term to the Dirac Lagrangian requires a left- as well as a right-handed spinor. If we accept that both kinds of neutrinos exist, then other combinations of left- and right-handed spinors can be constructed as well and may be considered part of the theory as long as they behave like Lorentz scalars. The additional mass term that arises then is associated with the so-called Majorana mass. In it, the right-handed anti-neutrino is identified with the left-handed neutrino and vice versa. The general neutrino Lagrangian then contains both mass terms.

If the neutrino is a Majorana particle, that is if the Lagrangian contains the Majorana mass term, it is possible for the anti-neutrino emitted in the one nucleon's beta decay to be absorbed as a neutrino in the other nucleon's beta decay, so that no neutrino leaves the nucleus:

$$(A, Z) \rightarrow (A, Z + 2) + 2e^{-}. \tag{1.3}$$

Observing this $0\nu\beta\beta$ decay would not only confirm the Majorana nature of neutrinos, but also provide important information - in the form of the transition amplitude - for determining the effective Majorana mass. Furthermore, it would show that the lepton number is not a conserved quantity.

GERDA[15] The lifetimes of nuclei towards two neutrino double beta decay are in the range of $6 \cdot 10^{18}$ to $2 \cdot 10^{21}$ years. The current best limit for the lifetime of ^{76}Ge towards neutrinoless double beta decay is $1.9 \cdot 10^{25}$ years[16]. Lifetimes of that magnitude translate to very small event rates, which necessitate large sample masses, long detection times and an ultra low radioactivity background to see a signal at all. All this is planned to be realized in the GERDA experiment.

The GERDA collaboration chose to look for the neutrinoless double beta decay in the Germanium isotope ^{76}Ge. This has the advantage that natural germanium crystals can be enriched with ^{76}Ge and subsequently made into a germanium detector. The energy of the two electrons from the double beta decay of ^{76}Ge is then directly deposited within the crystal and can be measured; the signature of a $0\nu\beta\beta$ event is an energy deposit of 2.04 MeV. This eliminates the need for other detector media and encasings which might introduce much radioactivity into the system. Also, much experience with the handling and operation of germanium detectors exists and they have the excellent energy resolution necessary to recognize the neutrinoless double beta decay signature.

An ultra low background level is necessary to probe beyond the current best limit; the aim is at 10^{-3} counts/kg/keV/year which would probe down to a lifetime of $2 \cdot 10^{26}$ years. The detector design and setup were done with this requirement in mind, providing for maximum shielding to external radiation and minimizing the introduction of radioactive materials through detector parts. This is achieved by an "onion layer" design where the germanium crystals are in the center, surrounded by liquid argon which cools the crystals and at the same time shields against residual radioactivity of the cryostat that contains the cryogenic liquid. The whole cryostat is submersed in ultra pure water which moderates neutron radiation and acts as a Cherenkov detector thus providing an active muon veto. To that end the walls of the water tank are equipped with photo multipliers. All materials used are extremely radio-pure and the amount of matter which could contain impurities close to the crystals is further reduced by operating bare germanium crystals, with only a minimal mechanical structure to hold them in place.

Liquid argon will be used as the cryogenic liquid instead of liquid Nitrogen because with its higher density it makes a better passive shielding against external radiation, and its scintillation can be used in an additional active veto system if the inside of the cryostat is equipped with photo multipliers as well. The liquid argon scintillation can then not only be used to detect that some kind of ionizing radiation is coming through, but by pulse shape analysis it is possible to determine the nature of this radiation. This information would be helpful to find out what isotope or reaction the background is coming from so that mitigation strategies can be developed.

1.2 Dark matter

Over 70 years ago, Fritz Zwicky found that most of the matter in galaxy clusters does not emit light. Today, the nature of this "dark matter" is still a mystery. While the existence of it is no longer in doubt, it could not yet be detected directly.

The presence of dark matter is inferred from its gravitational effects on visible matter[9]. Many candidates of ordinary matter have been suggested to account for the excess gravity, but since COBE and WMAP[12] it is generally accepted that more than 80 % of the unaccounted for matter is non-baryonic in nature, and thus unlike anything we know.

Various extensions to the Standard Model of particle physics predict the existence of as yet unobserved new particle kinds. The most favoured one of those with respect to a dark matter candidate is the neutralino, which arises in some super symmetrical extensions. Axions and heavy neutrinos also rank highly on the suspect list[5]. The subset of possible particles which could explain the astronomical observations, i.e. such that are heavy, cold (non relativistic) and interact only through gravitation and possibly another very weak force, are generically called WIMPs (Weakly Interacting Massive Particles).

The only lever we have on detecting these WIMPs directly is their weak interaction, which should make it possible for them to scatter from a regular (baryonic) matter target nucleus. The kinetic energy imparted on the target nucleus can then be measured. Such experiments are not sensitive to the nature of the force, it could be the regular "weak interaction" known from, for example, the beta decay, or an unknown kind of force. Of practical interest for experiments is then the expected event rate and the expected energy deposit in the detector. Since nothing is known about WIMPs, there can be only speculations on those points:

In order to be consistent with astrophysical and high energy physics observations, WIMPs should have a mass larger than about 100 GeV. Their density and velocity distributions in the galaxy are unknown, so a simple spherically symmetric non-rotating model is assumed, where the particles are in equilibrium and have a maxwellian velocity distribution, cut off at the escape velocity of the galaxy. It can furthermore be expected that the WIMPs are clustered around heavy objects like the Sun and the Earth.

The value of the scattering cross section is model dependant and affords uncertainties over at least 4 orders of magnitude, between 10^{-40} and 10^{-44} cm^2/nucleon. This is not only due to the inherent ignorance about the WIMP properties, but also due to uncertainties in the form factors of the possible target nuclei.

The predicted values for the event rate reflect the uncertainties in local number density, velocity, mass and cross section; they vary in a range of 10^{-4} to 10 events/kg/day[4]. The energy deposited by a WIMP scattering one is looking for is typically in the range of 10 to 100 keV. The lower limit is given by detector thresholds, the upper limit by the requirement of having a sizable event rate.

Small event rates and small energy deposition necessitate large detector volumes and a low energy threshold. Since natural radioactivity is omnipresent and populates

the energy region of interest, it is mandatory to operate the detector in an ultra low radioactivity environment, including going underground and using radio-pure materials. The underground suppression can be improved considerably if, in addition to these precautions, the detector is able to discriminate between energy deposition through nuclear recoils and through interaction with shell electrons. In that case, the background from beta and gamma radiation is mitigated. Background from neutrons however is unchanged, since neutrons also interact through nuclear recoils.

For further reading refer to ref.[4] for expected dark matter properties and ref.[8] for an overview over current experimental efforts.

Liquid rare gas detectors perform well in all areas important for dark matter detection, in particular they allow nuclear recoils to be differentiated from other events, therefore many experiments that look for dark matter utilizing liquid rare gases have been propsed. Among those are WARP[11], where a 100 l liquid argon detector will be employed, XENON[13] with a 22 kg liquid xenon detector, DEAP with currently 7 kg of liquid argon as the detector medium but planning for a ton-scale experiment and ArDM[2], as well with liquid argon as the detector medium.

The possibility to recognize background of a certain kind is not only important for external background reduction, but also to mitigate the presence of the radioactive isotope ^{39}Ar in natural argon, which is a beta emitter with a half-life of 369 years. The concentration of ^{39}Ar in natural argon is $8.1 \pm 0.3 \cdot 10^{-16}$, leading to an activity of $1.783 \pm 0.006 \cdot 10^{-3}$ Bq/l[6]. Without an effective means of recognising these events, liquid argon would be of limited use to dark-matter experiments, though for GERDA the ^{39}Ar is not a problem because with a Q-Value of 565 keV it is far below the energy region of interest.

The number of electron induced events from ^{39}Ar is about $3 \cdot 10^7$ per kg and year. Many of those can be discarded based on their energies; only about 2% of events deposit an energy between 10 and 25 keV. this means that in a 2 kg liquid argon detector, $1.26 \cdot 10^6$ events have to be suppressed[1].

Chapter 2

Theory and literature review

2.1 Argon properties

Argon is a noble gas with atomic number 28. It is the third most abundant gas in the atmosphere, can be purified easily and has a relatively high stopping power for ionizing radiation, making it suitable as a detection medium. Table 2.1 lists some basic properties of argon that will be of use.

Table 2.1: argon properties.

melting point (at 1 bar)	-189.35 C (83.80 K)
boiling point (at 1 bar)	-185.9 C (87.30 K)
density at 0 C	1.784 g/l
density at -186 C	1.4 kg/l
expansion ratio liquid to gas	1:840
ionization potential (gas)	15.7 eV
ionization potential (liquid)	13.4 eV
electron configuration	$[\mathrm{Ne}](3s)^2(3p)^6$
crystal structure	fcc
W value (gas)	26.4 eV
W value (liquid)	$23.6^{+0.5}_{-0.3}$eV [27]

The electron configuration of an ordinary argon atom is $[\mathrm{Ne}](3s)^2(3p)^6$, resulting in a $^1S_0$ state. The lowest excited states are obtained by lifting an electron from the 3p shell up to the 4s shell, where its spin can be parallel or anti-parallel to the resulting spin of the rest of the atom. In the case of anti-parallel spins, the atom is in a singlet

state: $^1P_1$. In the case of parallel spins, a triplet state arises and the possibilities are: $^3P_0$, $^3P_1$ and $^3P_2$. Refer to table 2.2 for a summary and for energy levels.

Table 2.2: The argon atom's lowest excited states. [41]

configuration	state	energy [eV]
$[\mathrm{Ne}](3s)^2(3p)^6$	$^1S_0$	0.0
$[\mathrm{Ne}](3s)^2(3p)^5 \uparrow (4s) \downarrow$	$^1P_1$	11.82
$[\mathrm{Ne}](3s)^2(3p)^6 \uparrow (4s) \uparrow$	$^3P_0$	11.72
	$^3P_1$	11.62
	$^3P_2$	11.54

2.2 Scintillation mechanism

Basics The passage of ionizing radiation through liquid argon does not produce any permanent chemical change in the argon. It does however ionize and excite argon atoms, which in such a state become highly reactive. Argon atoms would not usually form stable molecules, but in certain states of excitation, or when ionized, they can form strong bonds with regular argon atoms, leading to excited dimers (so called excimers) Ar_2^* and to ionized dimers Ar_2^+[23]. Of the four low lying atomic states, the potential well necessary for excimer formation occurs for the $^3P_2$ and the $^3P_1$ state, so that two distinct excimer states arise: A singlet state $^1\Sigma_u \quad (^3P_1 +^1 S_0)$ and a triplet state $^3\Sigma_u \quad (^3P_2 +^1 S_0)$[23]. The decay of those two states into the repulsive ground state is the origin of argon scintillation light not only in the liquid, but also in the solid and in the gas (compare figure 2.2), as shown by spectroscopy. The peaks from the singlet and the triplet excimer decay are not resolved, because various rotational energy levels in both excimer states overlap, so that only one broad peak can be seen at a peak wavelength of 128 nm and with a FWHM of 10 nm.

This scintillation by excimer decay makes liquid argon usable as a scintillator in the first place, since the photons from the direct decay of the Ar^* are resonance trapped in the liquid[1] and thus hardly reach the detector. The photons from the excimer decay do not have enough energy to be resonance absorbed by argon atoms, and Ar_2, which could in principle absorb them, is not present[2], so they can reach the detector unhindered.

[1] The photon from the Ar^* decay has just the right energy to excite another argon atom into that state, so the photon will be absorbed and re-emitted many times before reaching the boundary of the detector.

[2] There have been indications that in xenon gas under high pressure, Xe_2 could be present and lend itself to direct excitation into Xe_2^*[30], and there are speculations that this could also happen in liquid argon.

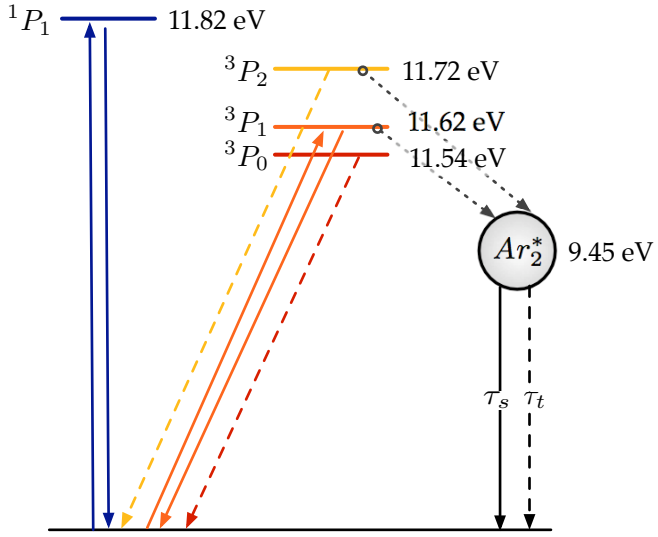

Figure 2.1: argon atom excited states. Dashed lines represent dipole forbidden transitions (this part follows [43]). The states that can form argon excimers with a ground state atom are marked with pointers to a lower lying Ar_2^* level.

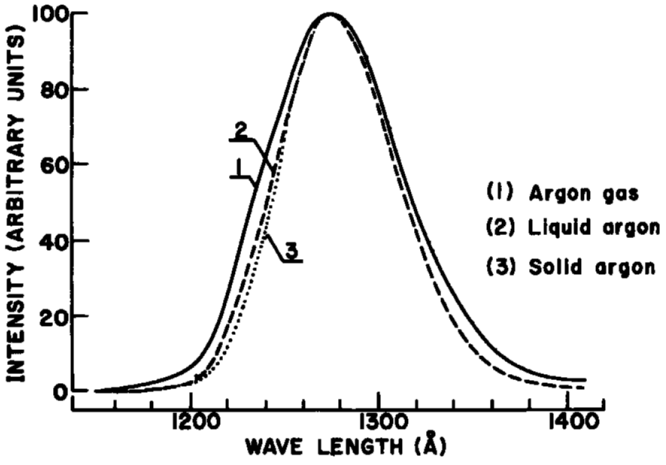

Figure 2.2: The Ar_2^* emission peaks in the emission spectra of pure argon gas (at 200°K), liquid (at 87°K) and solid (at 80°K) argon. Taken from ref.[40].

Two characteristics of the excimers will prove to be the key to pulse shape discrimination. First, their lifetimes: The dipole allowed transition of the singlet excimer to the ground state has a lifetime in the order of several nano seconds, while the triplet excimer has a much longer lifetime in the order of one micro second. This decay is made possible by spin-orbit coupling. The second characteristic concerns the effect of different particle kinds on the number ratio of excimers produced in the two states. If N_s and N_t are the number of excimers in the singlet state and in the triplet state, and

$$R = \frac{N_s}{N_t} \tag{2.1}$$

the ratio between them, then the value of R crucially depends on the linear energy transfer dE/dx (LET) of the penetrating radiation[54][58][56]. The more energy is dissipated per unit track length, the bigger R becomes. The lifetimes of the excimers however are independent of the exciting radiation.

Table 2.2 serves as an overview over the experimental values obtained for lifetimes and R values. See [48] for a more complete list of lifetimes measured.

Property	photon excitation	alpha excitation	fission fragment excitation
$\tau_{singlet}$	$6 \pm 2ns$[57] $6ns$ [35]	$7.1 \pm 1.0ns$	$6.8 \pm 1.0ns$
$\tau_{triplet}$	$1590 \pm 100ns$[57] $1000ns$ [35]	$1660 \pm 100ns$	$1550 \pm 100ns$
R	0.3 [57]	1.3	3.0

From excitation to photon emission It will be useful to have a closer look at the processes that lead to formation of argon excimers, since this is not so straight-forward.

The atomic states in liquid argon form energy bands similar to those in the solid, including valence and conduction bands with a band-gap of approximately 10 eV[38]. The energy bands in the liquid however do not have sharply defined edges, due to the lack of strict translational symmetry.

The exciton states that correspond to the low lying atomic states can be adequately described using the Frenkel Model, where the electron is tightly bound to its parent atom. Higher exciton states approach the Wannier-Mott picture, where the electron belongs to a large number of atoms, so that the excitons in liquid argon are considered "intermediate", lying somewhere between those two extremes. It is not yet clear how excitons can form at all in a medium lacking spacial symmetry, but some theories have been developed to explain their existence[50][52].

The processes that eventually lead to photon emission are closely connected to the formation of excitons and are sketched in figure 2.3. In step A, an exciton is formed directly. It may initially be in one of the higher energy states, but cools down quickly

through collisions (B). Once it is in one of the lowest energy states, it becomes self-trapped. The self-trapped exciton can be looked at in the single-atom picture, where it corresponds to the formation of an excimer (C). This excimer, which can be either in the singlet or in the triplet state, decays under emission of a photon (D).

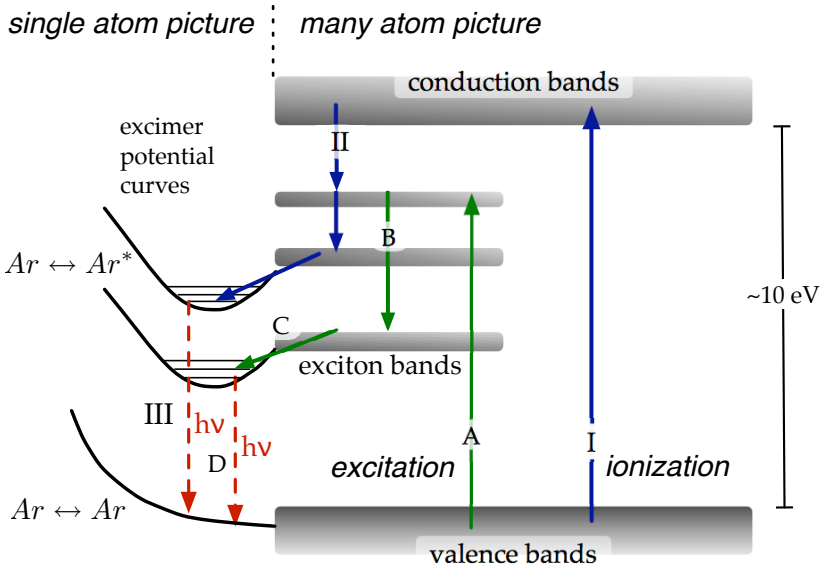

Figure 2.3: They processes that eventually lead to emission of a photon.

This can be summarized with the following scheme:[55][49]

$$Ar^* + Ar + Ar \xrightarrow{1-10ps} Ar_2^* + Ar \tag{2.2}$$

$$Ar_2^* \xrightarrow{\sim 10ns/\sim 1\mu s} Ar + Ar + \gamma(128nm) \tag{2.3}$$

where the additional Ar takes away excess energy and angular momentum.

Another possible path begins with step I, where an electron from the valence band is excited into the conduction band. While it is up there losing energy through collisions, the ion it leaves behind bonds with another argon atom. Eventually the electron is pulled back by the Coulomb force of the positive charge and they recombine (II). If the electron recombines into a state without an attractive inter-atom potential, the dimer breaks apart, only to bond again when the electron loses more energy and ends up in a state that possesses such a potential (B and C again). The question whether the electron recombines with the very ion it came from or with just any ion in the track of the incident particle is not settled yet,[28, 22, 20] but whichever way, one ends up with an excimer in either the singlet or the triplet state. Finally that excimer decays under emission of a photon (III).

The reaction scheme is:[54][55][26]

$$Ar + Ar + Ar^+ + e^- \rightarrow Ar_2^+ + e^- \tag{2.4}$$

$$Ar_2^+ + e^- \xrightarrow{\sim 900ps} Ar + Ar^{**} + \text{heat} \tag{2.5}$$

$$Ar^{**} \xrightarrow{\sim 4ps} Ar^* + \text{heat} \tag{2.6}$$

$$Ar^* + Ar + Ar \rightarrow Ar_2^* + Ar \tag{2.7}$$

$$Ar_2^* \rightarrow Ar + Ar + \gamma(128nm) \tag{2.8}$$

The ratio between the number of excitations N_{ex} and the number of ionizations N_i is

$$\frac{N_{ex}}{N_i} = 0.21 \qquad [55] \tag{2.9}$$

The reaction schemes show that next to scintillation photons, free charge carriers and heat are produced, but those effects will not be utilized here.

Photon reducing processes In the absence of any photon reducing processes, every excimer is expected to emit one photon, because the energy gap between the excimer and the ground state is too big for non-radiative transitions[55].In the absence of an electric field, all the free electrons will recombine with an ion and a photon will be emitted. It looks like there will be one photon for every excitation or ionization, but that is not the case.The following photon reducing processes play a role in liquid argon:[55][56][54]

Biexcitonic quenching happens in the high LET[3] region where a large number of excitons are produced, so that the chance of two of them colliding is considerable. They undergo the reaction

$$Ar^* + Ar^* \rightarrow Ar + Ar^+ + e^-.$$

The ion and electron will then recombine and only one photon is emitted instead of two.

Escaping electrons account for photon loss in the low LET region where only few atoms are ionized. If the electron becomes thermalised beyond a critical radius, it will not recombine – at least not in the time-window of the measurement.

Charge carrier trapping is the attachment of electrons to electronegative impurities, most notably oxygen, preventing recombination of electron and argon ion.

Electronic energy transfer to impurity atoms is a very effective process in liquid argon by which the excitation energy of an argon atom is transferred to an impurity atom[34][41]. Impurities such as Nitrogen or water, which relax non-radiatively, considerably quench the scintillation light[59]. Sometimes, however, this process can prove useful, namely when the impurity emission has more favorable properties

[3] LET = Linear Energy Transfer (dE/dx)

than the argon emission does, for example if it has a shorter lifetime or if it has a wavelength that makes it easier to detect. A special case where excitation energy is transferred to xenon atoms which then decay radiatively is discussed in chapter 7 on page 68.

Table 2.3: Liquid argon properties.

W value	$23.6^{+0.5}_{-0.3}$eV [27]
scintillation wavelength (peak value)	128 nm
attenuation length (own scintillation light)	66± 3 cm [21]

The average energy needed to produce one electron-ion pair, the so called "W-value", was measured by Doke et al. [27] who found

$$W = 23.6^{+0.5}_{-0.3} eV \tag{2.10}$$

for excitation under conversion electrons. With the known ratio of excitations to ionizations (eq. 2.9), the average energy needed to produce one scintillation photon can be estimated as

$$W_{ph} = \frac{W}{1 + N_{ex}/N_i} \tag{2.11}$$

$$= 19.5 \pm 0.4 eV \tag{2.12}$$

Alpha quenching The number of emitted photons is proportional to the energy deposit. The more energy is deposited, the more scintillation photons will be produced. This scintillation photon yield per deposited energy is however not the same for particles with different LETs, and since the LET can be a function of particle velocity, it might not even be the same for the same particle kind over all velocities. This is because two of the photon reducing processes directly depend on the LET (see also section 6.3.1 on page 56).

In liquid argon, the higher the LET (and thus the higher the ratio R), the less scintillation photons will be emitted per deposited energy. Alpha quenching refers to the fact that at the same energy deposit in the detector, less photons will be emitted under alpha particle excitation than under photon excitation. Under neutron excitation even less energy is visible in the scintillation because their LET is even bigger than that of alpha particles.

Chapter 3

Pulse shape discrimination study on simulated data

The goal of this chapter is to study how well discrimination between alpha, beta/gamma[1] and neutron/fission-fragment radiation signals is possible in liquid argon under ideal conditions. Neither electronic nor any other practical limitations will be taken into account; only the intrinsic argon scintillation properties are considered.

Disregarding detector effects implies disregarding detection efficiencies. It will be assumed that every photon produced is actually registered. This approach does not pose a problem for later comparison with experimental data, since the results obtained for a number of produced photons N_{ph}^{theo} will stay the same when replacing N_{ph}^{theo} with the usually much smaller number of detected photons N_{ph}^{exp}. Or even more realistically, when it is replaced by the number of detected photo electrons.

The pulses to be studied will be generated via a Monte Carlo simulation. This is a useful thing to do, because using experimental data poses some challenges. First of all, experimental pulse shapes incorporate many detector effects which are to be disregarded for now. Then, in order to study how well the pulses can be told apart from each other, one has to know a priori what particle kind generated the pulse. Then one can look at how many of them a given algorithm assigns correctly. In an experiment, it is very hard to get a "clean" data sample, one where it is certain that only pulses of one single kind of particle are present. Even when known sources are used to generate events, it is nearly impossible to exclude the presence of unwanted radiation. That is why this study will be done using simulated data.

Discrimination between different particle kinds is possible because the pulse shapes they evoke are not identical. In liquid argon, the pulse shape, that is the time dependence

[1] Beta and gamma radiation signals are indistinguishable in liquid argon, since gamma radiation manifests itself by producing electrons, so it looks just like beta radiation. The same goes for neutron and fission fragment radiation, which both show through nuclear recoils and are also indistinguishable here.

of the measured signal intensity, varies with the LET of the ionizing radiation. Namely, the LET determines the ratio R between excimers produced in the singlet and in the triplet state, so that the differences between the pulse shapes stem from the different relative strengths of emission from those two states.

3.1 The pulse shape

Mathematically, the pulse shapes we are interested in can be described by a probability density function (PDF). It expresses the probability for a photon to be emitted at a time t after its excimer was formed. If N photons are emitted by N excimers independently of each other, the average number of them emitted at any specific time t, and thus the signal intensity at that time, is

$$I(t) = p(t) \cdot N_{ph} \tag{3.1}$$

with $p(t)$ the appropriate PDF.

Excimer relaxation follows an exponential decay law. The (normalized) PDF for the decay of a singlet/triplet excimer is thus:

$$p_{s,t}(t) = \frac{1}{\tau_{s,t}} \cdot e^{-\frac{t}{\tau_{s,t}}}. \tag{3.2}$$

The pulse shape is a superposition of photons from the singlet and the triplet excimer decay, so the complete PDF has to be the sum of the singlet and the triplet excimer PDFs, with the summands weighted by the relative strengths of their respective contributions.

Let f_s and f_t be those relative weights of the singlet and the triplet contributions. They can be written as:

$$f_s = \frac{N_s}{N_s + N_t} \tag{3.3}$$

$$f_t = \frac{N_t}{N_s + N_t} \tag{3.4}$$

With

$$\frac{N_s}{N_t} = R \quad \text{and} \tag{3.5}$$

$$f_s + f_t = 1 \tag{3.6}$$

it follows that

$$f_s = R/(R+1) \quad \text{and} \tag{3.7}$$

$$f_t = 1/(R+1) \tag{3.8}$$

.

One can now write the complete PDF, depending on the ratio R and the lifetimes of the excimers, as:

$$\begin{aligned} p(t) &= f_s \cdot p_s(t) + f_t \cdot p_t(t) \\ &= \frac{R}{R+1} \cdot \frac{1}{\tau_s} \cdot e^{-\frac{t}{\tau_s}} + \frac{1}{R+1} \cdot \frac{1}{\tau_t} \cdot e^{-\frac{t}{\tau_t}} \end{aligned} \tag{3.9}$$

The PDFs for each particle kind, $p_\gamma(t)$, $p_\alpha(t)$ and $p_n(t)$, are obtained by plugging in R_α, R_γ and R_n for R in $p(t)$. It is shown for photons in figure 3.1.

This means the pulse shapes are purely ideal ones, the parameters R, τ_s and τ_t however are taken from fits to actual measured pulse shapes. There is no other way to do this if the simulation is to be comparable to the measurement.

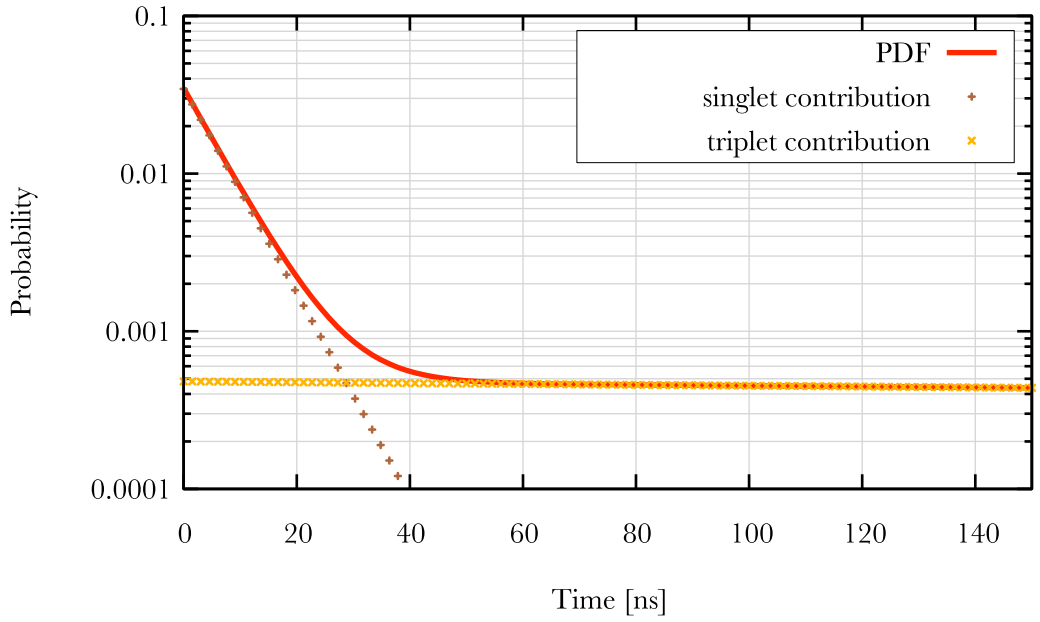

Figure 3.1: Probability density function for the emission of a photon under excitation with photons.

3.2 Pulse shape discrimination methods

Discrimination is usually done by running an algorithm over a pulse that yields a discrimination parameter D, whose value depends on the shape of the pulse. Then those pulses with the same value of D were evoked by the same kind of particle.

If all pulses consisted of an infinite amount of photons, thus exactly reproducing the shape of the PDF, there would be one unique value of the discrimination parameter for each particle kind. But since there is only a finite number of photons in a pulse shape, and their emission is a statistical process, the D values of the pulses from the same

particle species have some spread around a mean value. So for each particle species there will be an ideal value, say D^γ or D^α, and a spread (σ^γ and σ^α) around these values.

This means that there is a possible overlap between the D values from the various particle species, which imposes a limit on the achievable discrimination power. Those pulse shapes with a D value in the overlap region cannot be assigned to their particles with absolute certainty. One has to choose a "border value" D^{border} in between each set of D^j and D^k, then say that every pulse with a D on one side of the border is from particle kind j, while those on the other side of D^{border} are from particle kind k. Thus an error is introduced into the discrimination; a certain percentage of the pulses are assigned to the wrong kinds of particles. The smaller this error is, the better the discrimination power.

The achievable discrimination power depends of course on the pulse shapes; if they are very similar, the discrimination parameters will be close together, allowing for a big overlap. It also depends on the algorithm used to calculate D and how well it takes into account the differences between the pulse shapes. Finally, the number of available photons plays a role. The more photons there are in the pulse shape, the less do statistical fluctuations play a role, and the more accurately can the discrimination be done. Since the number of photons in a pulse is proportional to the energy the particle leaves in the argon, one can expect the discrimination to work better for high energy radiation than it does for low energy radiation.

Two algorithms will be employed to assign pulse shapes to the particle kind from which they stem: a simple "fast to total" ratio and the so-called Gatti filter. Their respective performances, advantages and disadvantages will be discussed.

3.2.1 "Fast to total" filter

Concept The "fast to total"[2] algorithm is a commonly used discrimination method in liquid scintillation detectors. It uses the feature, often found in such detectors, that the percentage of photons emitted in a certain time window depends on the exciting radiation. This feature is very prominent in liquid argon, owing to the large difference between the lifetimes of the two excimer states, and keeping in mind that the relative number of excitons in each state is a function of LET and thus an indicator of the exciting particle identity.

The different lifetimes make the separation of the singlet and the triplet excimer contribution to the pulse possible to a certain extend: The singlet excimer with its 6.7 ns lifetime emits 99% of its photons within the first 32 ns, while only 2.4% of the triplet photons are emitted during that time. The fraction of photons that arrive before

[2] As in "The number of photons that arrive within a short time window after the onset of the pulse, divided by the total amount of photons in the pulse"

a time T_{cut}, where T_{cut} is in the area of 32 ns, thus reflects the relative number of excitons in the two states.

As an example, the fraction of photons emitted during the first 40 ns under excitation of the three particle kinds of interest is shown in table 3.1. It is exactly that fraction, albeit not necessarily with the same choice of T_{cut}, that is used as discrimination parameter in the "fast to total" algorithm.

Particle	R[57]	Fraction of photons emitted during the first 40 ns
gamma	0.3	0.25
alpha	1.3	0.57
neutron	3.0	0.75

Table 3.1: The dependence of the fraction of photons in a time slot $T_{cut} = 40ns$ on the ratio R of fast to slow component intensities (from ref.[57]). Also compare figure 3.2.

The idea is further illustrated in figure 3.2, which shows the photon PDFs for alpha, gamma and neutron radiation. Their emission probabilities in the fast time slot follow the order of their R values.

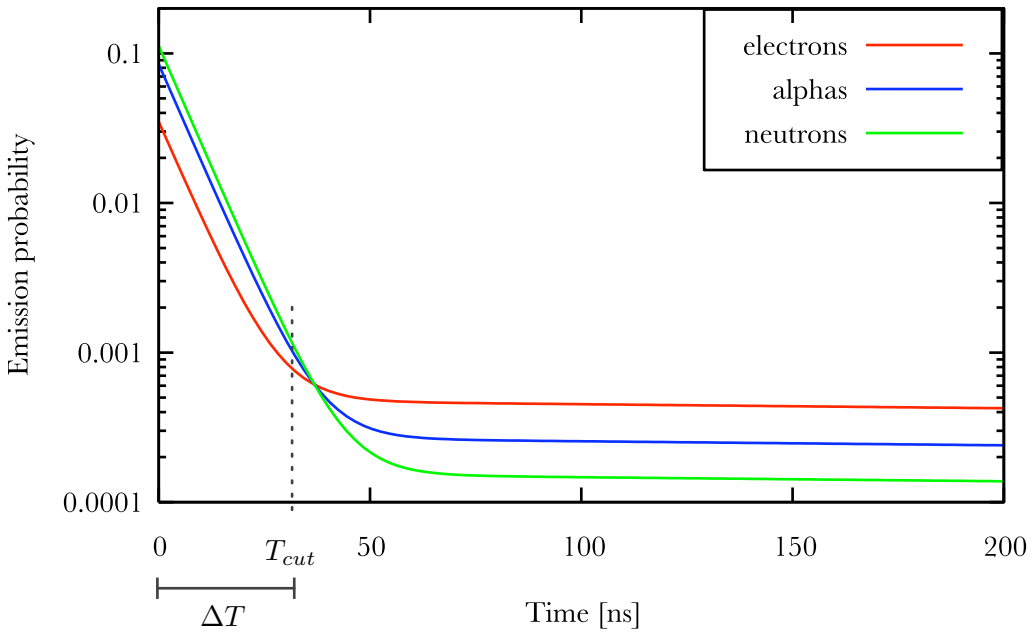

Figure 3.2: Comparison of the photon emission PDF under alpha, gamma and neutron excitation.

The discrimination parameter D_{ft} (fast to total) is defined as:

$$D_{ft} = \frac{\int_0^{T_{cut}} I(t)\mathrm{d}t}{\int_0^{\infty} I(t)\mathrm{d}t} \tag{3.10}$$

It is equivalent to D_{fs} (fast to slow):

$$D_{fs} = \frac{\int_0^{T_{cut}} I(t)\mathrm{d}t}{\int_{T_{cut}}^{\infty} I(t)\mathrm{d}t} \tag{3.11}$$

There should be an ideal choice of T_{cut}, for which the distance between the expected values of D_{ft}^{γ}, D_{ft}^{α} and D_{ft}^{n} is maximal. For the pulse shapes considered here, $T_{cut} = 37ns$ is this best choice, because that is where the three pulse shapes cross each other. Before 37 ns the pulse shapes become increasingly different. After 37 ns the difference gained so far is reversed again.

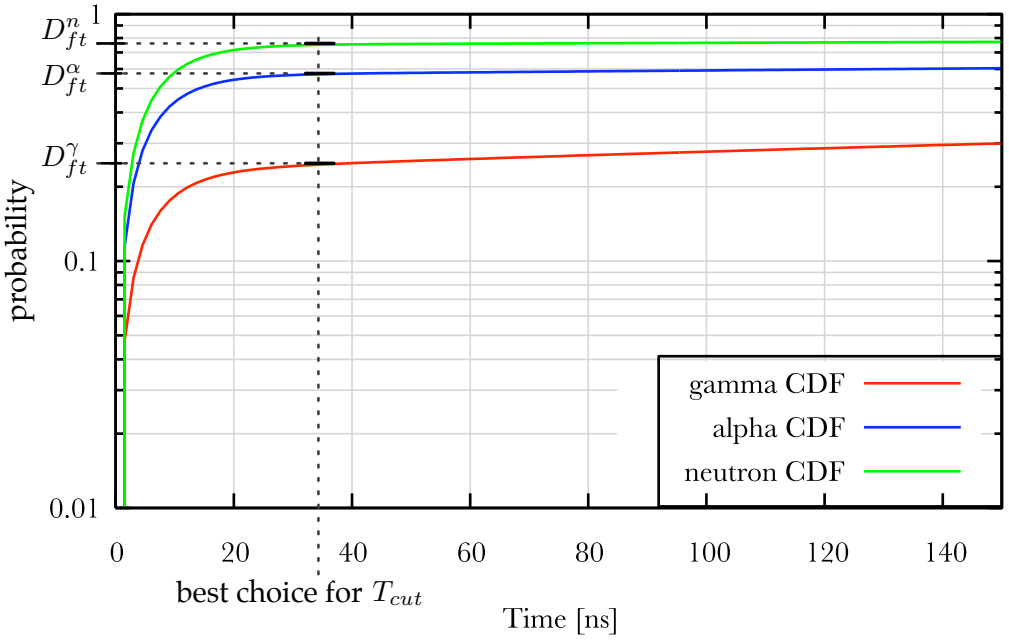

Figure 3.3: CDF functions

This can best be seen looking at the cumulative distribution functions (CDFs) in

figure 3.3. The CDF is the integral over the PDF:

$$P(t) = \int_0^t p(t')\mathrm{d}t' \tag{3.12}$$

$$= \underbrace{\frac{R}{R+1}\left(1 - e^{-t/\tau_s}\right)}_{P_s(t)} + \underbrace{\frac{1}{R+1}\left(1 - e^{-t/\tau_t}\right)}_{P_t(t)} \tag{3.13}$$

Its range is from zero to one and it describes the probability that a photon was emitted before time t, or in other words, the fraction of photons emitted in the time slot $[0, t]$. This means that the value of the CDF at any time t is nothing but the expected ratio D_{ft} at $T_{cut} = t$.

It is desirable for the ideal ratios to be as far apart from each other as possible, so the best time for T_{cut} is that where the CDFs are furthest apart from each other, and this means one is looking to maximize $P_\gamma(t) - P_\alpha(t)$:

$$P_\gamma(t) - P_\alpha(t) = max \tag{3.14}$$

$$\Rightarrow \frac{\partial}{\partial t}\left(P_\gamma(t) - P_\alpha(t)\right) = 0 \tag{3.15}$$

$$\Rightarrow p_\gamma(t) - p_\alpha(t) = 0 \tag{3.16}$$

$$\Rightarrow p_\gamma(t) = p_\alpha(t) \tag{3.17}$$

Proving that the CDFs are furthest apart where the PDFs cross. The same argument applies to the combination with the neutron PDF, with the result that the best time is where all three PDFs cross.

It is also obvious from the plot of the CDFs that the choice of T_{cut} is not a crucial one. The slope in the area of the ideal value is very small, so that moving T_{cut} to either side a little will not make a big difference for the discrimination power.

This method does not require the knowledge of the exact photon emission PDFs for the particles to be discriminated; they are needed here merely to generate the pulses by Monte Carlo methods. The algorithm itself only requires a difference in some ratio between fast and slow photons; the optimal value of T_{cut} can then always be found by trial and error.

Monto Carlo simulation The MC program I wrote integrates the simulation of the pulses with the calculation of D_{ft}. Its output is - for every number of photons between zero and a variable maximum number - either a set of D_{ft} values, or an array of bins containing the counts of how many times D_{ft} fell into the bin. The former is used just for plotting, to get a visual idea of the behavior; the latter is used for quantitative studies.

To do the simulation, random numbers representing the emission times t of a photon have to be drawn in such a way as to reproduce the PDF $p(t)$. This can easily be done if the inverse of the cumulative distribution function (CDF) is available, because, drawing

a random number y from a uniform distribution over the range $[0, 1]$, one can obtain values of t distributed like $p(t)$ with

$$t = P^{-1}(y) \tag{3.18}$$

Unfortunately, it is not possible to invert $P(t)$ algebraically. The single parts, $P_s(t)$ and $P_t(t)$, however are easily inverted. The MC program therefore first chooses whether a photon was emitted by a singlet or a triplet state excimer using the known ratio R between them, then it samples the t value from the appropriate partial CDF.

The full procedure is the following:

1. The number of photons in the pulse shape is set to a start value.
2. An array is initialized where each bin represents a given range in D_{ft}.
3. With that number of photons, the simulation is repeated *loops* times:
   (a) For every photon in the pulse:
      i. A random number x in the range $[0, 1]$ decides over the excimer state. If $x < R/(R + 1)$ it is a singlet, else it is a triplet.
      ii. The emission time t is drawn from the singlet/triplet PDF as decided in the previous step, by choosing another random number $y \in [0, 1]$ and calculating
      $$t = P_{s/t}^{-1}(y)$$
      iii. Once the emission time is determined, the program just checks whether or not it falls within the fast time window ΔT. The fast time window can be set to arbitrary values.
   (b) D_{ft} is calculated and written into the binned array.
4. The array of ratios for this number of photons is written to file.
5. The number of photons is increased and everything starts over.

This can be done for every particle kind of interest by adjusting the value of R. The value of *loops* was one million for the data presented here.

Results Figure 3.4 shows a typical scatterplot of the discrimination parameter values obtained at different photon numbers. The three bands belong to gamma, alpha and neutron radiation pulses. As expected, for large photon numbers the ratios are tightly assembled around mean values D_{ft}^{γ}, D_{ft}^{α} and D_{ft}^{n} , while for small photon numbers, statistical fluctuations cause a considerable increase in spread. The distance between the groups depends on the time chosen for T_{cut}, following the separation of the CDFs in figure 3.3.

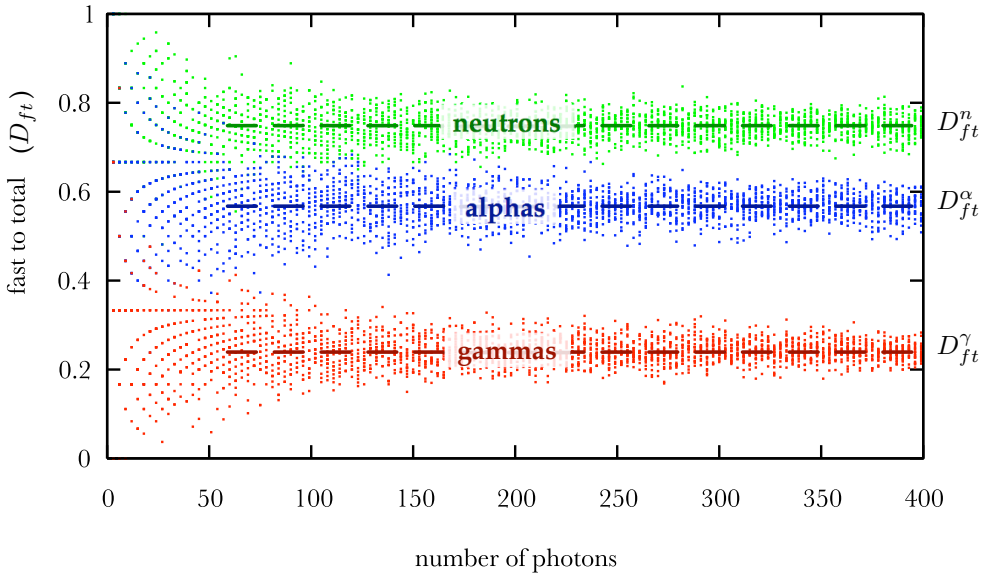

Figure 3.4: Typical scatterplot with the discrimination parameter D_{ft} as it depends on the number of photons. The line structure at small photon numbers arises because with so few photons to distribute, there is only a small number of possible ratios; all the bins in between stay empty. Sample size: $2.5 \cdot 10^5$ pulses.

Figure 3.5 shows only the alpha band of figure 3.4, blown up to 3 dimensions and in different states of rotation. The data is artificially "sliced" along the N_{ph}-axis, because values are accumulated in steps of 5 photons. These slices, however, give a good impression of the projection of the data onto the D_{ft}-axis, which will be used shortly.

The next step is to find out how many events from one band leak into another band. To do that, a value of D^{ft} between each set of two bands has to be chosen to mark the end of one and the beginning of the next band; I will call that value D^{border}. These borders divide the plot into as many regions as the number of particles considered, and all events in one region will be identified with the same particle. All that remains to do then is to count how many of the events from one band lie above the upper and below the lower border of its region.

The idea is illustrated in figure 3.6 (top), which shows a projection of figure 3.4 onto the y-axis, taking only the slice at 50 photons on the x-axis. A possible choice for D^{border} between the gamma and the alpha band, as well as between the alpha and the neutron band, is represented by the grey double lines. They divide the plot into 3 regions: γ-region, α-region and neutron-region. The areas where one band overlaps with the region of another band are colored in light red, blue and green for gammas, alphas and neutrons. The percentage of the complete band that these areas represent tells us how big an error is made. This percentage is shown in figure 3.6 (bottom) for all possible choices of D^{border}.

For gammas, only the events above the border of the γ-region matter, since there

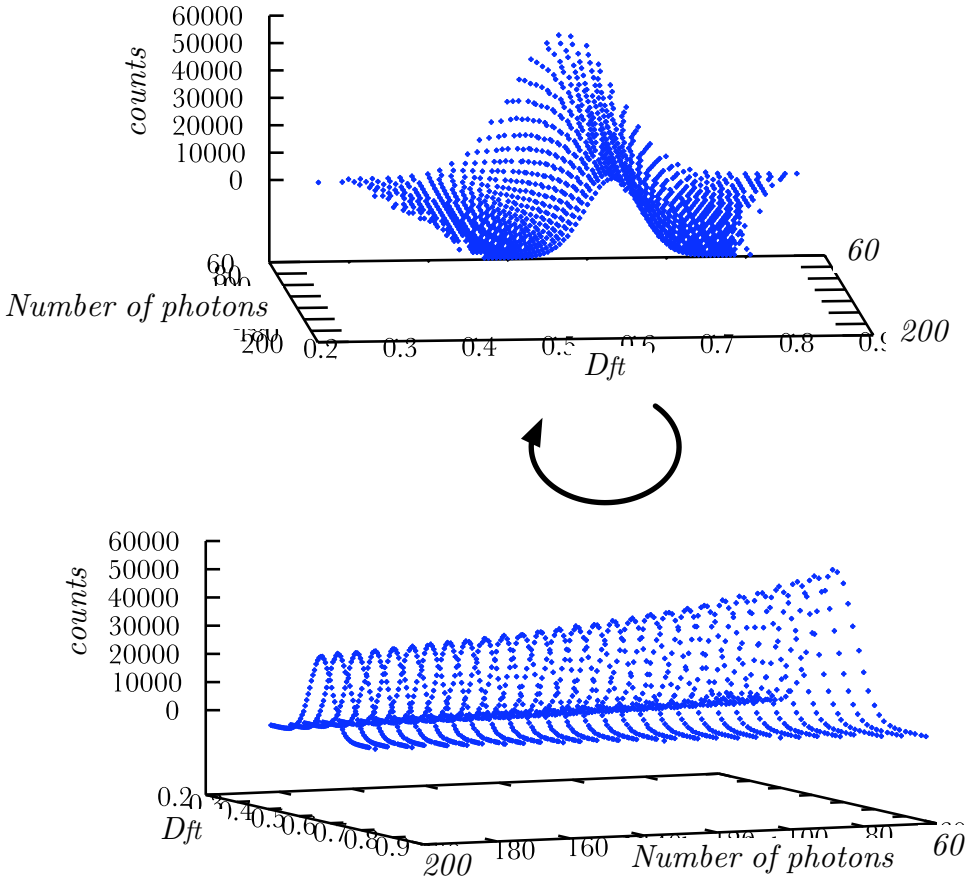

Figure 3.5: Alpha simulation result

is nothing below. This is different for alphas. Being the middle band, they leak into the γ-region below and into the neutron-region above, so that the percentage of events above as well as that below their region borders is plotted. Finally, only the neutron events below their region border are of interest, since there is no further region above.
What the best choice of D^{border} is depends on the application. Possible applications, and questions that arise from them, are the following:

- If one is interested in discriminating two or more kinds of particles against each other, one should choose D^{border} in such a way that it minimizes the misidentification probability on either side. The choice of border between the α- and the neutron-band in figure 3.7 illustrates this point. Two questions might arise:
  - How many photons are needed to guarantee a given discrimination power?
  - What discrimination power is achievable with a given number of photons?
- If one is interested in background suppression, the value of D^{border} should be moved until the desired level of suppression is achieved, even though that means losing non-background events. Consider the choice of border between the γ- and the α-band in figure 3.7. A good suppression of α events is guaranteed, but many γ events are lost, too. The question to be asked here is:
  - Where does D^{border} need to be placed to guarantee a given background suppression at a fixed number of available photons, and how many non-background events are lost?

All these questions are answered by the bottom plots of figures 3.6 and 3.7. The fraction of events above/below D^{border} is just the rejection/acceptance level reachable at the chosen D^{border}. These plots directly represent the discrimination power of the algorithm at the given number of photons.

3.2.2 Gatti's filter

Concept The Gatti filter [62] is the result of an attempt to find the best possible linear discrimination method, independent of the form of the pulse shape. It takes the pulse as a succession of equal time slots δt_i, each with a corresponding number of photons n_i in it. The discrimination parameter D_G is a weighted sum over the n_i

$$D_G = \sum_i P_i n_i \tag{3.19}$$

This algorithm lacks automatic normalization of the pulses, but only pulses made of the same number of photons can be compared. To remedy this, Gatti and Martini chose to group signals with the same number of photons N, then did the discrimination on each group separately. However, one can also just normalize everything to an arbitrary

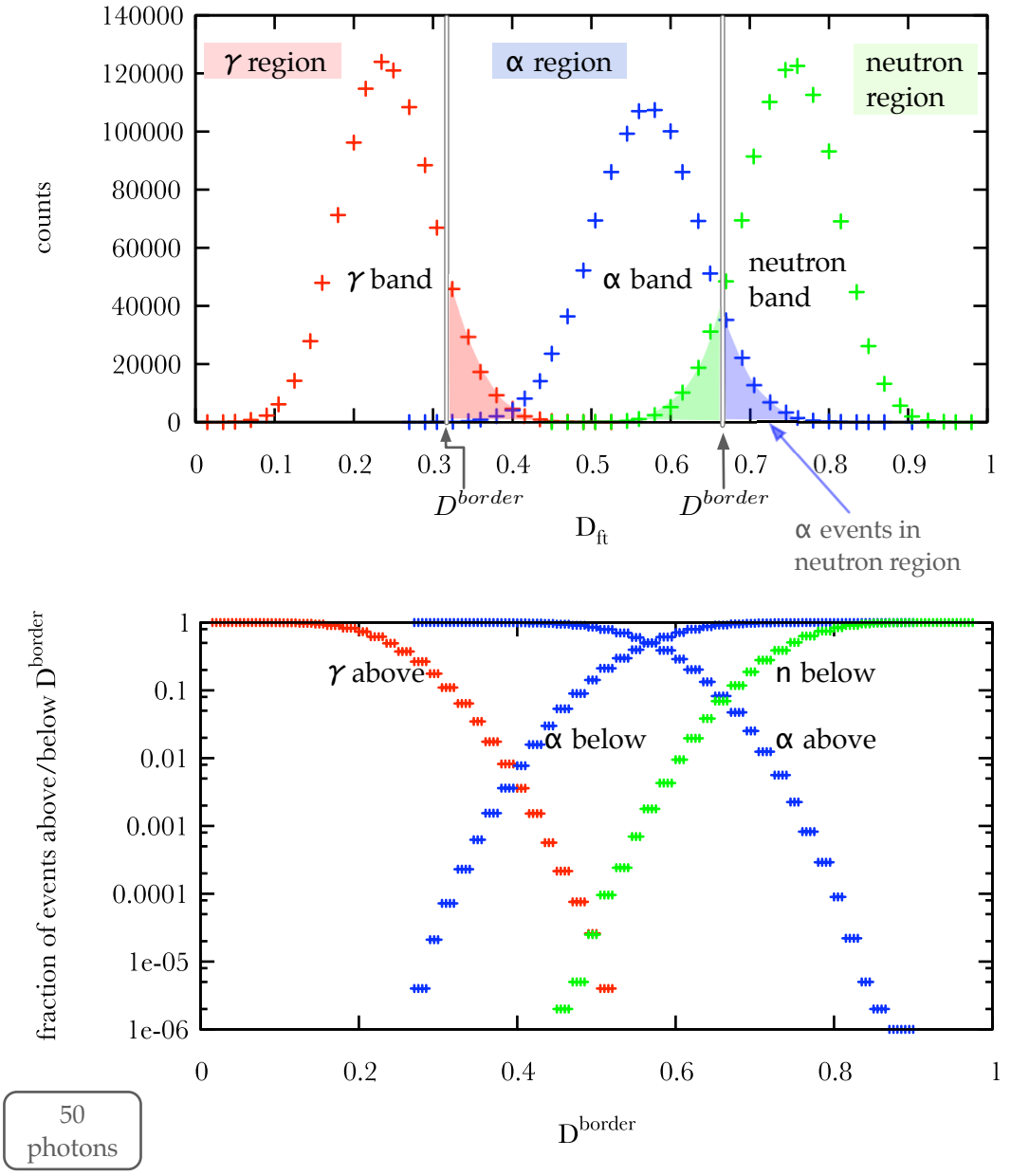

Figure 3.6: Top: The γ, α and neutron band projections at 55 photons. The choices of a D^{border} between the bands lead to regions. The events of a band that lie outside their regions are shaded in the respective color of their band. Bottom: The fraction the shaded region has of the whole band depending on the choice of D^{border}. Sample size: 10^6 pulses.

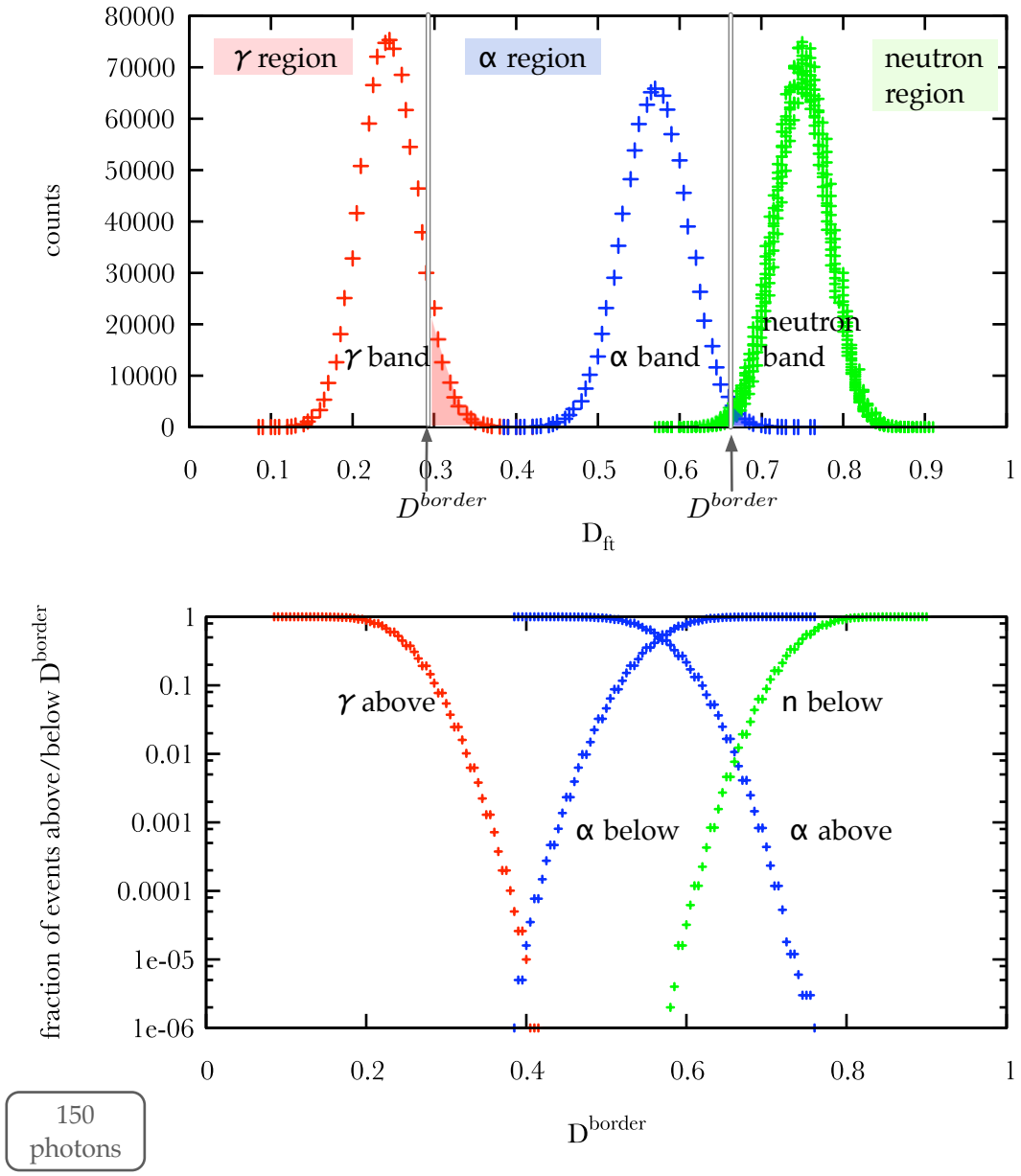

Figure 3.7: Same plot as figure 3.6, but this time at 150 photons. Sample size: 10^6 pulses.

number, which is what I chose to do, because it ensures comparability of discrimination parameters at different photon numbers. In summary, for every pulse considered here the equation

$$\sum_i n_i = 1. \tag{3.20}$$

is valid.

Say one wants to discriminate alpha from gamma pulse shapes. Given the expected number of photons in each time slot for both particle kinds, α_i and γ_i, Gatti and Martini derive for the weights

$$W_i = \frac{\alpha_i - \gamma_i}{\alpha_i + \gamma_i} \tag{3.21}$$

The weights W_i are chosen in such a way that the signals at those times where the difference between the pulse shapes is largest have the largest influence. This requires the knowledge of the ideal, or at least the average, pulse shape of each particle kind involved.

The D_G values will be spread around the two mean values

$$D_G^\gamma = \sum_i W_i \gamma_i \quad \text{and} \tag{3.22}$$

$$D_G^\alpha = \sum_i W_i \alpha_i \tag{3.23}$$

Monte Carlo simulation The Gatti filter only works on sets of two different pulse shapes, because the weights can only be calculated for pairs of two. Therefore, if one is looking to discriminate between pulse shapes from three different particles, one needs three weight functions: $W_{\gamma\leftrightarrow\alpha}$, $W_{\gamma\leftrightarrow n}$ and $W_{\alpha\leftrightarrow n}$.

In the MC program, the weights are calculated using the PDFs for the three particle species: $p_\gamma(t)$, $p_\alpha(t)$ and $p_n(t)$.

$$W_{\gamma\leftrightarrow\alpha}(t) = \frac{p_\gamma - p_\alpha}{p_\gamma + p_\alpha} \tag{3.24}$$

$$W_{\gamma\leftrightarrow n}(t) = \frac{p_\gamma - p_n}{p_\gamma + p_n} \tag{3.25}$$

$$W_{\alpha\leftrightarrow n}(t) = \frac{p_\alpha - p_n}{p_\alpha + p_n} \tag{3.26}$$

Three arrays are written such that the value $P(i \cdot 1ns)$ can be found in bin i. For simplicity, $\delta t_i = 1ns$. Three more arrays are set up to represent the pulses, one for each particle species. Each array consists of bins representing a time interval of 1 ns.

The program works just like the "fast to total" MC simulation does, except that it now counts how many times a photon's emission time falls into each of the δt_i bins, instead of just counting how many photons arrive earlier or later than a given T_{cut}. One ends up with an array that can be seen as a proper pulse shape – the intensity as it depends on time.

Once a whole pulse of one particle kind has been simulated, the pulse shape array is used to calculate two discrimination parameters D_G, according to equation 3.19, to discriminate this pulse against pulses from the other two particle kinds respectively. When, for example, alpha particles are simulated, the two discrimination parameters calculated are $D_G^{\gamma\to\alpha}$ for discrimination against gammas and $D_G^{\alpha\to n}$ for discrimination against neutrons, using the weight functions $W_{\gamma\leftrightarrow\alpha}$ and $W_{\alpha\leftrightarrow n}$ respectively.

Results One plot with three bands in it is not possible here, for the same reason three weight functions are needed: the Gatti filter works on sets of two. Further discussion will concentrate on discrimination of gamma against neutron radiation since this is of interest for dark matter detection.

Figure 3.8 shows the result of the Gatti filter applied on a sample of 10^6 pulses. The bands that arise are drawn in the top panel, the fraction of events above/below a given choice of D^{border} is drawn in the bottom panel. Compare figure 3.6 on page 24. The very same picture is shown in figure 3.9 for a pulse of 150 photons.

The evaluation method and ideas are the same as those in the "fast to total" section.

If this filter is to be used on actual data, pulses from other particle kinds than the two considered by the filter might be present. It is therefore interesting to see what happens when the Gatti filter is applied to such unaccounted for pulses. Figure 3.10 is the result of a simulation done as before, except that the discrimination parameter for the alpha pulses was calculated using the weights for the "neutron against γ" discrimination. The alpha band appears in between the neutron and the gamma band, but closer to the neutron band just like in the "fast to total" discrimination, because the alpha pulses are more similar to neutron than they are to gamma pulses.

3.2.3 Discussion

Table 3.2 lists the discrimination power "γ against *neutron*" for both discrimination methods discussed here, when D^{border} is chosen to minimize the error on each particle kind. Discrimination power here means the fraction of events in the wrong band, so smaller numbers mean better discrimination. The quoted values are at the same the acceptance levels for both types of events, because they were chosen at the intersection of the tails in the "fraction of events above/below D^{border}" plots.

The gamma-neutron discrimination power is of special interest to dark matter searches, because the WIMP signal is expected to show in the neutron band. It deposits energy the same way neutrons do – by nuclear recoils. The most abundant background to the dark matter search are gamma-like events, in liquid argon especially those caused by the beta decay of ^{39}Ar.

Another interesting plot with respect to dark matter search is figure 3.11. It shows how many percent of the neutron events are lost at a gamma rejection of 10^{-6}. Since

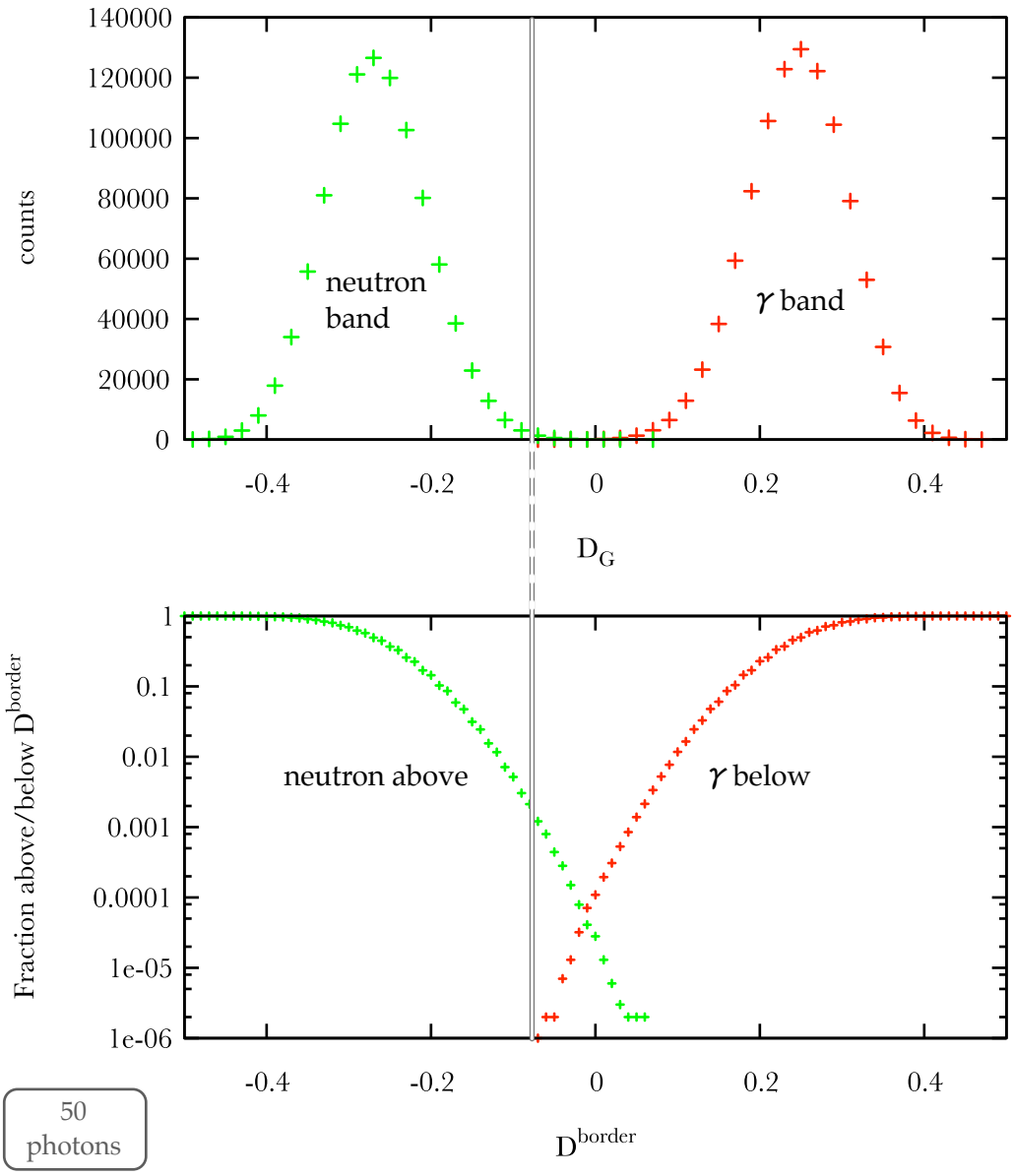

Figure 3.8: Top: The γ and neutron bands at 50 photons, using the Gatti filter. Bottom: Fraction of γ events below and neutron events above a given D^{border}. Sample size: 10^6 pulses.

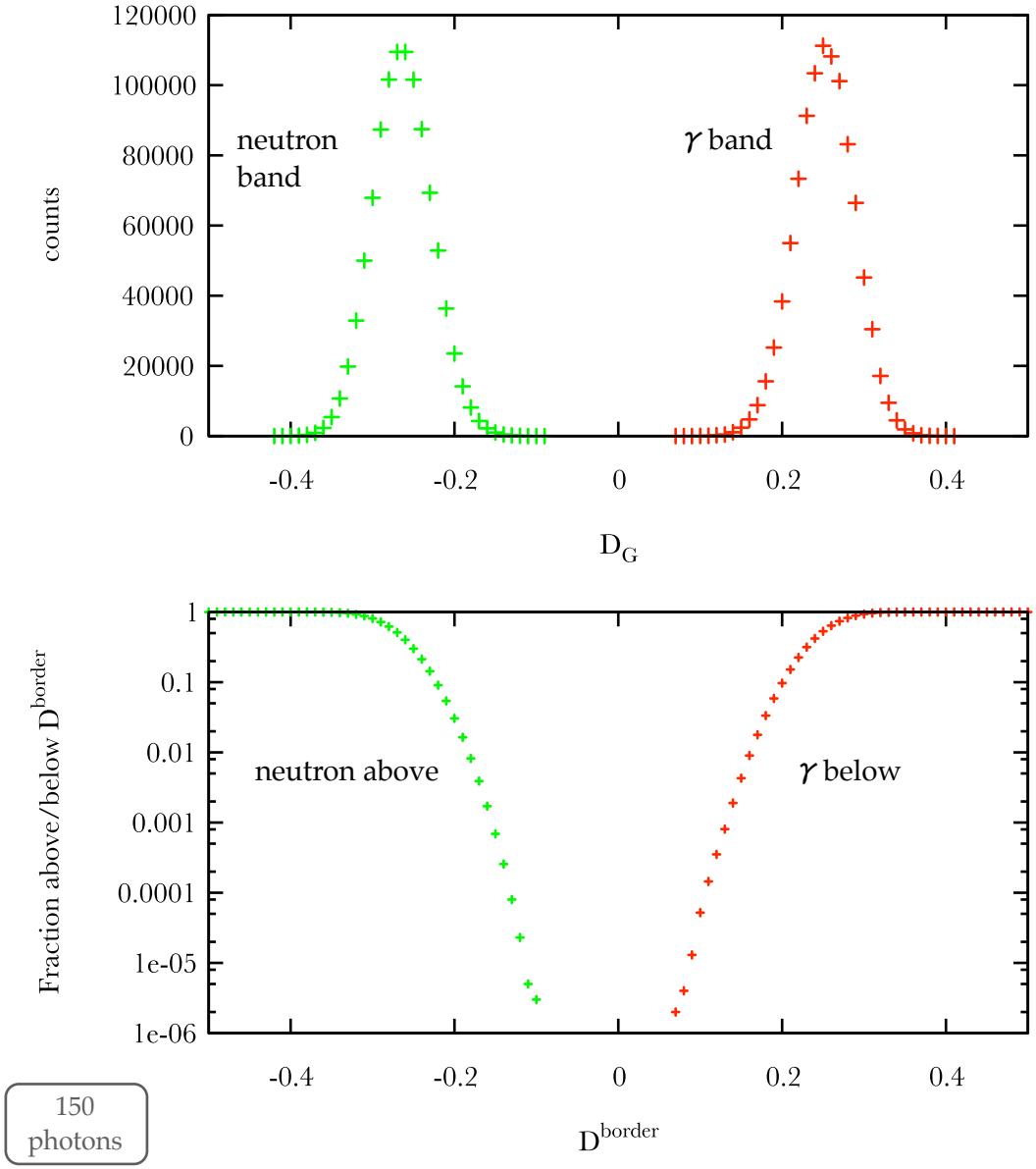

Figure 3.9: Sample size: 10^6 pulses.

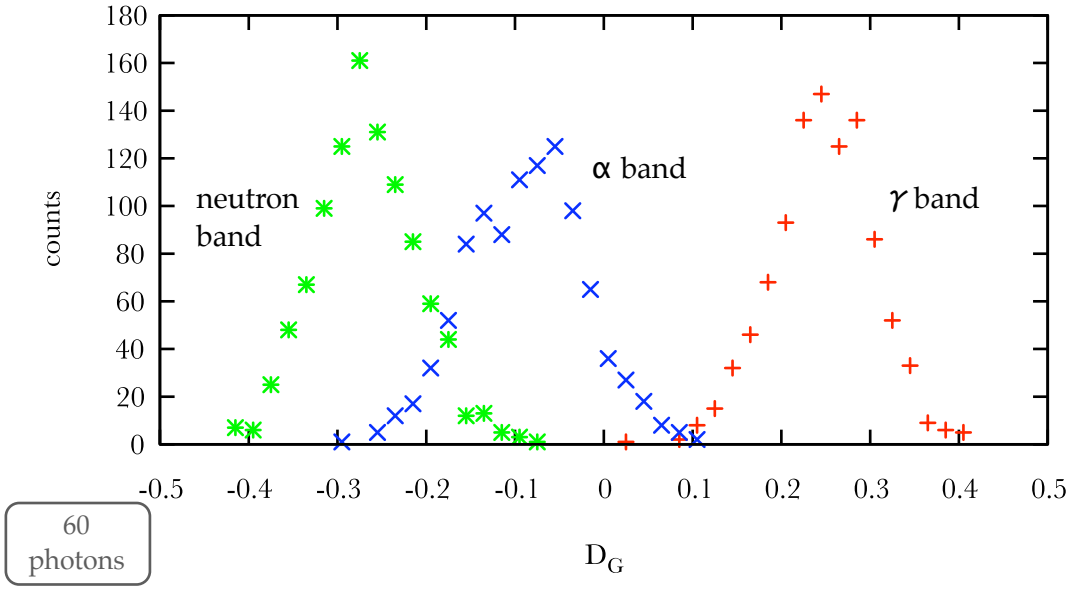

Figure 3.10: Alpha pulses evaluated with the Gatti weights for "neutron against γ" discrimination. Sample size: 1000 pulses.

N_{ph}	Gatti's filter	"fast to total" filter
40	$9.2 \cdot 10^{-5}$	$9.7 \cdot 10^{-5}$
50	$2.1 \cdot 10^{-5}$	$3.8 \cdot 10^{-5}$
60	$8.5 \cdot 10^{-6}$	$1.3 \cdot 10^{-5}$
70	$< 10^{-6}$	$2.5 \cdot 10^{-6}$

Table 3.2: The discrimination power between γ and neutron radiation signals of the two filters at different numbers of photons in the pulse. The intersection point between the distributions' tails was taken as the point of maximum discrimination. Above 70 photons, the tails of the two distributions do not overlap anymore, which means that the discrimination is better than 10^{-6}, since 10^6 events were simulated.

WIMPS deposit very little energy in the detector, it is important to know how far down in energy one can go without losing most of the signal when rejecting background.

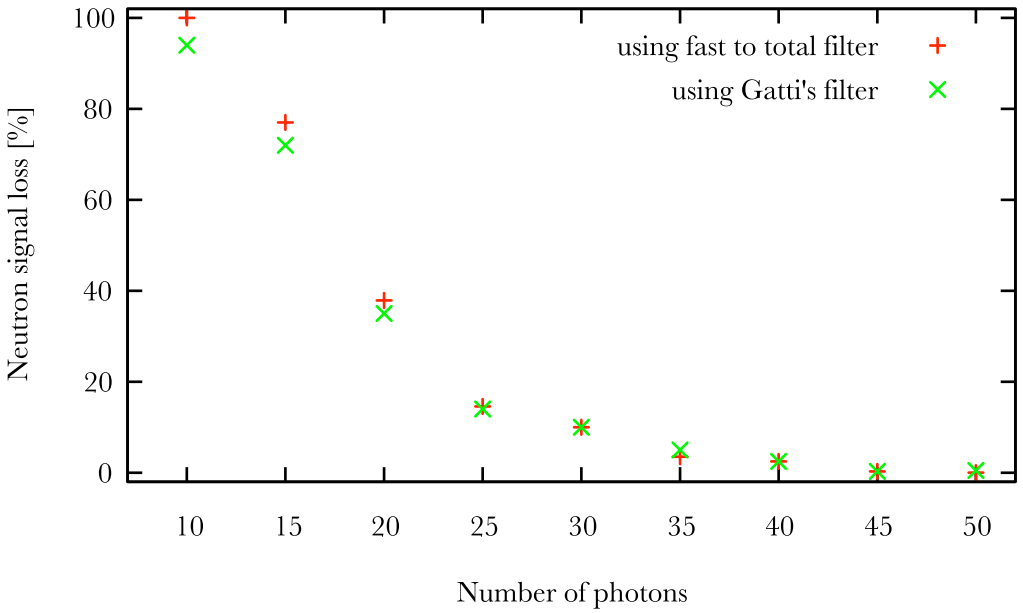

Figure 3.11: This plot shows the percentage of neutron events lost if D^{border} is chosen such that the rejection against gamma events is in the order of 10^{-6}. The points do not fall onto a smooth line because of the discrete nature of the simulated photon arrival times. Often it is not possible to have a point at the exact rejection level of $1 \cdot 10^{-6}$. The levels therefore fluctuate between 1 and 4 $\cdot 10^{-6}$ and bias the neutron loss accordingly.

The discrimination power between gamma and alpha events is smaller than that between gamma and neutron events, because the gamma and alpha pulse shapes resemble each other more closely. However, alpha events usually occur at very high energies, with a much higher number of detected photons in each event than that which was simulated here. Therefore, the separation of the alpha and the gamma band is expected to be excellent in the experiment.

In this simulated environment, the Gatti filter performs better than the simple "fast to total" ratio does, albeit not very much better. This does not necessarily mean that it is the method best suited for pulse shape discrimination in an actual experiment. There are several drawbacks in using this method, the most obvious of which is the necessity to know the expected PDF's for each particle species. This can only be achieved by calculating the average pulse shape from a large sample of measured pulses of the same particle species. The challenges involved in getting such a sample were one of the points which motivated the study of simulated data in the first place. In addition, this expected PDF can only be acquired for one specific detector. Any change to the detector requires

the renewed determination of the expected PDF. An inaccurate PDF would spoil the discrimination power of this filter.

A further challenge when using Gatti's filter on actual data is the exact determination of the pulse's onset. Since the Gatti filter compares the intensity in each time bin with the expected intensity, a slight shift of the onset means comparing the wrong time bins.

The "fast to total" ratio suffers from none of these drawbacks. The ideal time for the cut can be found out by trial and error, and the discrimination parameter does not depend crucially on the onset position. It also works on any number of particle kinds that might contribute a pulse, while the Gatti filter relies on there being pulse shapes from only two particle kinds present in the data, though other pulses also show as a separate band and could be taken into account.

The "number of photons" quoted in this chapter is always an exact number, not a threshold. Thus table 3.2 and figure 3.11 should be understood as the discrimination between pulses of exactly N_{ph} detected photons. In an experiment, one usually measures events in a certain energy range. The discrimination power at a thresh of N_{ph} detected photons is better than at exactly N_{ph} photons[3]. The values quoted are thus always lower limits.

At the background suppression power of 10^{-6} necessary to mitigate the electron induced events from the decay of ^{39}Ar it is possible to go down to 20 detected photons while keeping 60% of the signal. The energy threshold this corresponds to depends on the efficiency of the setup. This will be discussed more deeply in section 6.3 on page 56. For the LArGe setup it corresponds to an energy of 16 keV.

The results of this study are compatible with those obtained by Boulay and Hime[1] who did a similar simulation. They did the simulation taking into account a specific detector geometry and detection efficiencies, which was not done here.

[3]Because due to the discrimination power getting better with rising number of detected photons, when adding the scatterplots of discrimination parameter against energy together, the number of events in the right band grows more quickly than that outside the right band

Chapter 4

Implementation

4.1 LArGe@MPI-K

All the experiments described in this and the next chapter were carried out using the LArGe (Liquid Argon Germanium) setup at the Max Planck Institute für Kernphysik. The system was constructed to study the performance of Germanium detectors operated in liquid argon and to try out an active veto system for background suppression in the Gerda experiment using liquid argon scintillation light. It is described thoroughly in the PhD thesis by Peter Peiffer[63].

Figure 4.1 shows a schematic drawing of the LArGe detector.

Stainless steel tank The whole detector is housed in a stainless steel tank. The tank is air-tight and is kept at a constant over-pressure of 20 mbar to 30 mbar. Its lid has several feed-throughs for pipes, used for refilling liquid argon and allowing argon gas to escape, as well as the feed-throughs for the PMT's high voltage supply and data read out. There are two special feed-throughs, one for an optical fiber that points towards the photo-cathode of the PMT and another one for the source tube. The source tube is closed at the bottom but open at the top[1] and can be used to insert radioactive sources for internal irradiation.

A shield of 5 cm thick lead surrounds the stainless steel tank, leaving only the top of the detector and a 5x5 cm window in the side open. Through the side window external irradiation with radioactive sources is possible.

PMT An 8" photo multiplier tube (PMT) is immersed in the liquid argon and supported by an Aluminium lid on top of the Dewar, which also serves as a convection barrier. The spectral range of the PMT is between 275 nm and 630 nm, rendering it unfit to detect the liquid argon scintillation light at a wavelength of 128 nm. Its surface is therefore coated with a wavelength shifting dye which is also used on the reflector foil.

[1] To prevent moisture from condensing and freezing inside the pipe, it is sealed most of the time.

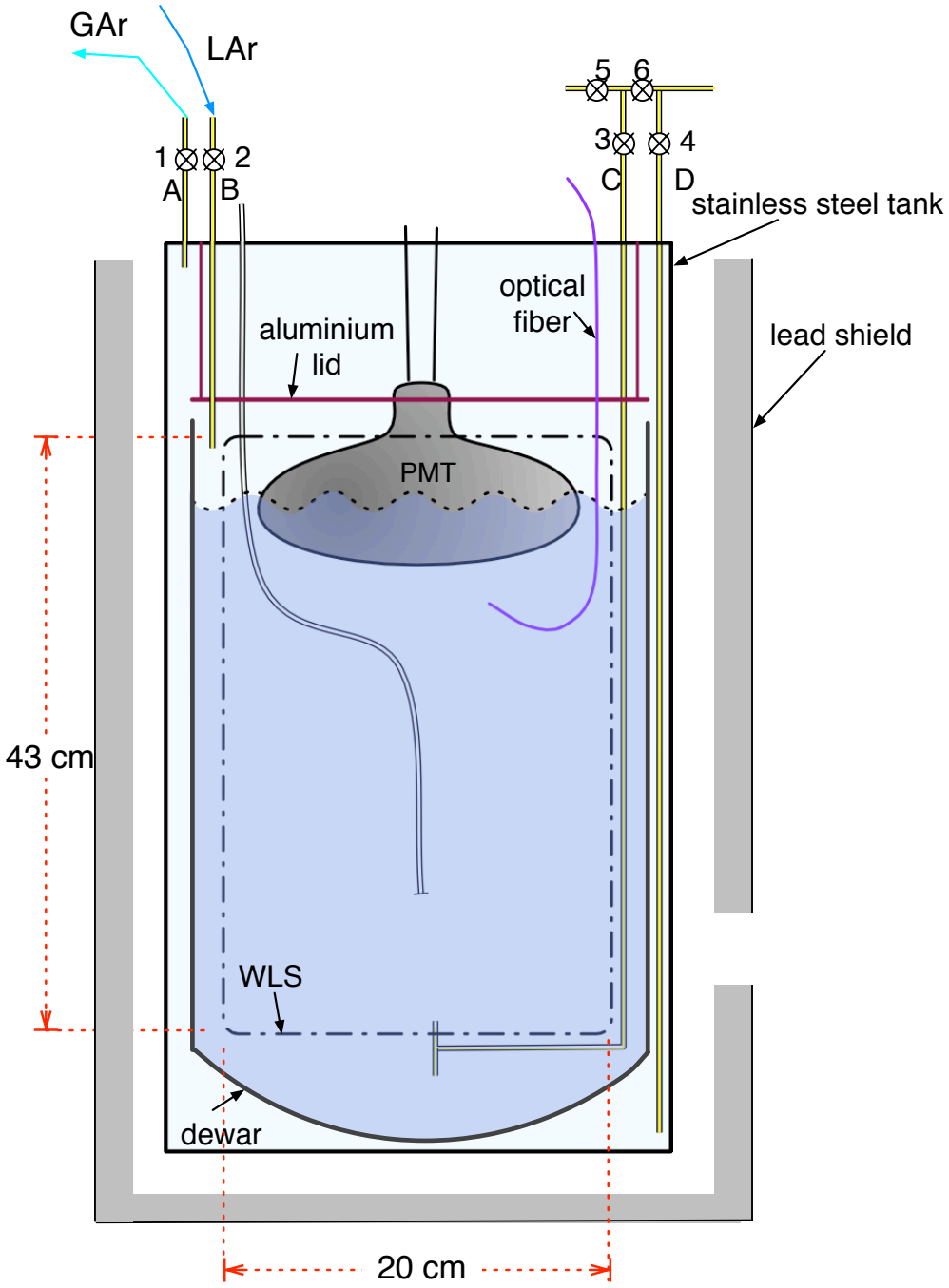

Figure 4.1: Schematic drawing of the LArGe setup (not to scale). LAr = liquid argon, GAr = gaseous argon, WLS = wave length shifter. Letters label pipes, numbers label valves.

The PMT is operated with negative high voltage of -1500 V to -1600 V. The choice of negative over positive high voltage is motivated by an improved signal quality at that setting.

Reflector foil A VM2000 reflector foil, coated with a solution of 10% TPB in polystyrene and fixed a few centimeters from the dewar walls, delimits a cylindrical volume that includes the PMT. The argon inside that foil constitutes the active volume of the detector (about 13.5 l).

The bare foil has a reflectivity of more than 99%[64] in the optical range, but wavelength shifts radiation in the UV range and reemits it isotropically, meaning that half of the photons are lost in the non-active part of the detector. The TPB coating on the inside prevents this loss by shifting the scintillation light from the vacuum ultraviolet into the optical range before it reaches the foil. The shifted light is then reflected back into the active volume by the foil and may reach the PMT.

4.2 Sources

Americium-241 and Thorium-228 were used as gamma radiation sources. Americium has one gamma line at 59.5 keV; the alpha particle it also emits is contained within the source tube. This source was chosen because its gamma has a high probability of depositing all its energy within the active volume, which makes it suitable for determining the detector's energy resolution.

The decay chain of Th-228 is shown in figure 4.2, where the lines we can see in the detector are bright red, while the lines that we can in principle see but have a small branching ratio are in dark red. The Thorium source was chosen because its many gamma lines can be used to calibrate the energy scale, especially the linear offset, and to compare gamma pulse shapes at different energies, measured under the exact same conditions.

An Americium-Beryllium source placed outside the lead shielding provided neutron radiation. The source is made of a mixture of Americium-241 and Beryllium-9, so that the alpha particles from the Americium decay can be absorbed by the Beryllium which then emits a neutron:

$$^{9}Be + \alpha \rightarrow ^{12} C + n \tag{4.1}$$

An additional 5 cm of lead turned out to be necessary to shield the system from the gamma radiation the source also emits, making it 10 cm of lead between the source and the detector.

Since alpha particles cannot penetrate any kind of shielding in our setup, Radon-222 gas was introduced into the liquid argon itself. The Radon does not disturb the argon scintillation or the other measurements at the concentration used. Its decay chain is

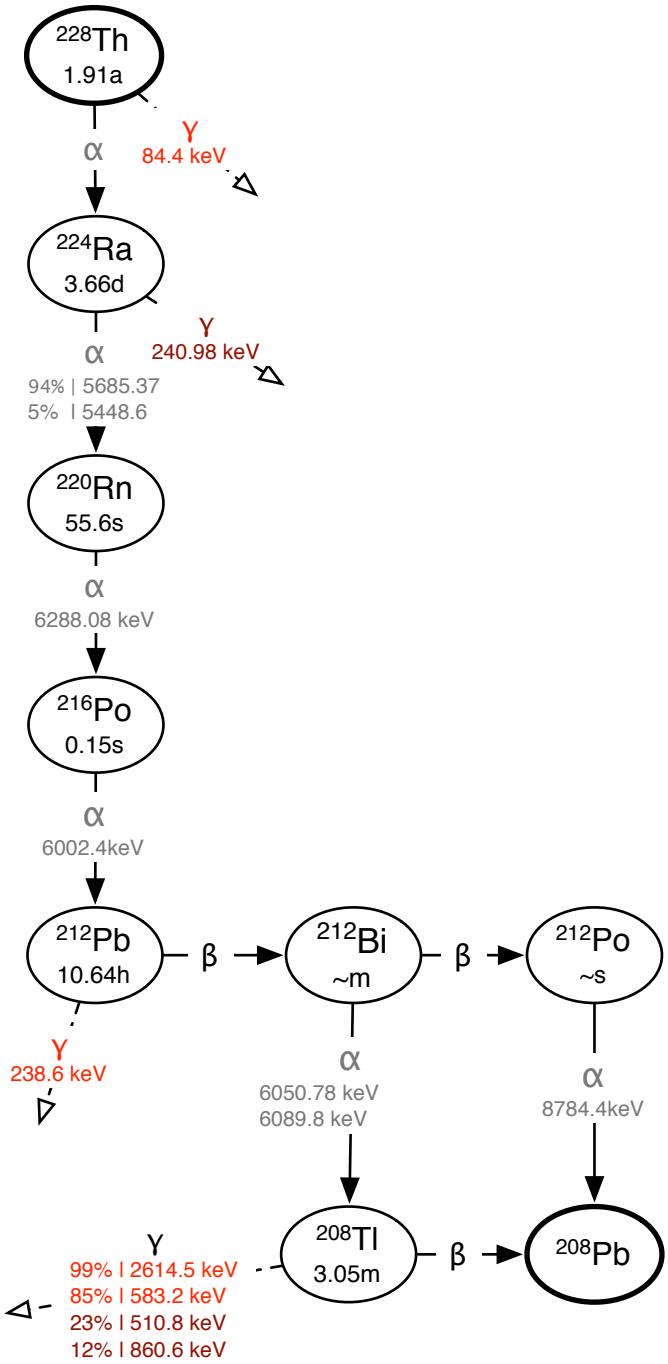

Figure 4.2: Thorium-228 decay chain. Gamma lines important to this work are drawn in light red. Gamma lines with a small branching ratio are dark red.

shown in figure 4.3 with the alphas we see in light red and the one we do not see well in dark red. In this case, the reason is not a low branching ratio, but the isotope Pb-210 with a half-life of 22.3 years interrupting the chain.

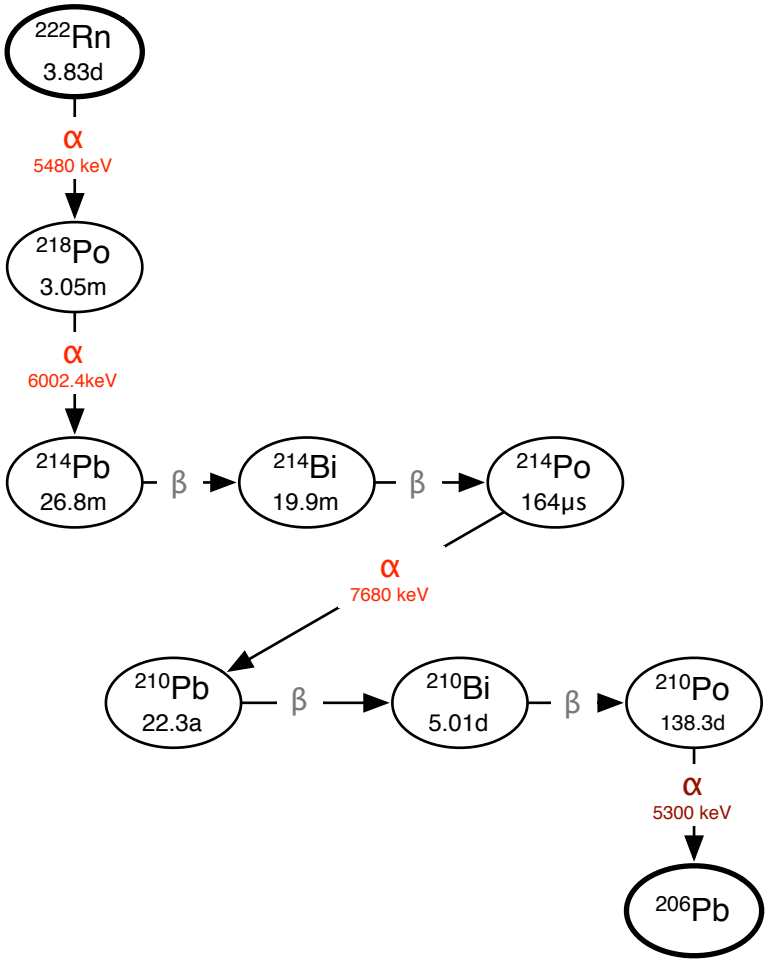

Figure 4.3: Radon-222 decay chain. Decays important to this work are drawn in light red.

4.3 Operation

During normal operation valve **1** is open while all others are closed, allowing evaporating argon to escape through pipe **A**. The pipe is connected to a bubbler filled with mineral oil to prevent air from entering the system. The overpressure of of 20 mbar to 30 mbar is automatically maintained that way.

Filling of liquid argon The detector is filled with liquid argon using pipe **B**, while gas can escape through pipe **A**, with valves **1** and **2** open and all others closed; the bubbler is disconnected from pipe **A** for the duration of the filling. The argon level is monitored using temperature sensors at known heights along the Dewar (not shown in the scheme). Refilling is necessary every three days and 12 hours after filling stable conditions are reached in the system.

Data accumulation A photon emitted in the liquid argon liberates a photo electron from the cathode of the PMT with a certain efficiency η[2]. This photo electron is accelerated from dynode to dynode where more and more electrons are liberated, so that after 10 to 12 steps an electron avalanche hits the anode and a voltage signal is measured. The signal data is read and stored with a digital oscilloscope. The anode of the PMT is connected to the oscilloscope directly, leading to a negative voltage signal. The last dynode is capacitively coupled to the oscilloscope, so its signal is positive.

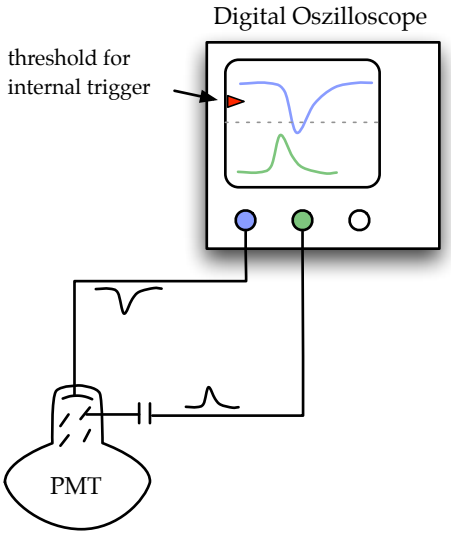

Figure 4.4: The data acquisition system.

Reading out two channels like this increases the dynamic range of the data acquisition. On the side of the PMT, it allows to operate the PMT at relatively high voltages needed for a good signal to noise ratio, while keeping all the signals in the linear range. Low energy gamma signals can be taken from the anode output which offers an amplification factor of 2.7 times the dynode signal strength. High energy alpha signals are out of the PMT's linear range then, but they can be read from the dynode. On the side of the oscilloscope, having two signal channels allows one to choose two different voltage scales. The intense fast component can be taken from a channel with say 20 V per division. The weak slow component is not visible at that scale, so it is taken from the second channel that could be set to 5 V per division, at which setting the fast component is in saturation.

Voltages are sampled with a user defined rate, in this case every 0.4 ns. The signal is recorded for 2 μs. The oscilloscope is triggered internally on either the anode or the dynode signal as soon as the signal intensity is higher than a given threshold. At a threshold of 5 mV on the anode and under about -1600 V high voltage, single photo electrons at the cathode cause a signal big enough to set off the trigger.

[2]More about this in section 6.3 on page 56.

Chapter 5

Data refinement: From the raw data to the average pulse shape

5.1 Data file format

The digitization of the signals on the oscilloscope can best be understood looking at figure 5.1. The y-(voltage-)axis of the oscilloscope is quantized by a variable of type "signed char". The y-position of a signal point is thus represented by an integer value y in the range $[-128, 127]$, independent of the voltage scale set for the channels drawn. In order to correlate a y value with the voltage it represents, it is necessary to know the voltage scale of each channel. If those scales are different for the channels drawn, then the same char value will represent different voltages for each channel.

The situation is similar on the x-(time-)axis, along which voltages are sampled with an adjustable rate. The sampled voltages $\{y_1, y_2, ..., y_n\}$ are written to file and the sampling rate is needed to correlate a voltage sample to the time it was taken at.

All the data used here was accumulated with a time resolution of 0.4 ns, so successive data points are that many nanoseconds apart in time. With 2 μ s total signal length this makes 5000 bytes per signal. The resolution on the voltage axis was adjusted to fit the height of the pulses of interest and generally lay between 5 mV and 20 mV per division.

The whole signal can be reconstructed from the array of signed chars $\{y_1, y_2, ..., y_n\}$, knowing the resolution on each axis, and the binary files the oscilloscope writes are just a succession of such signals. The method of getting an average pulse shape out of those data files is the subject of this chapter.

5.2 Baseline and onset

The first y value in a signal is not already the onset of the pulse. The oscilloscope was configured so that the first few hundred nanoseconds are just baseline, to be used to find

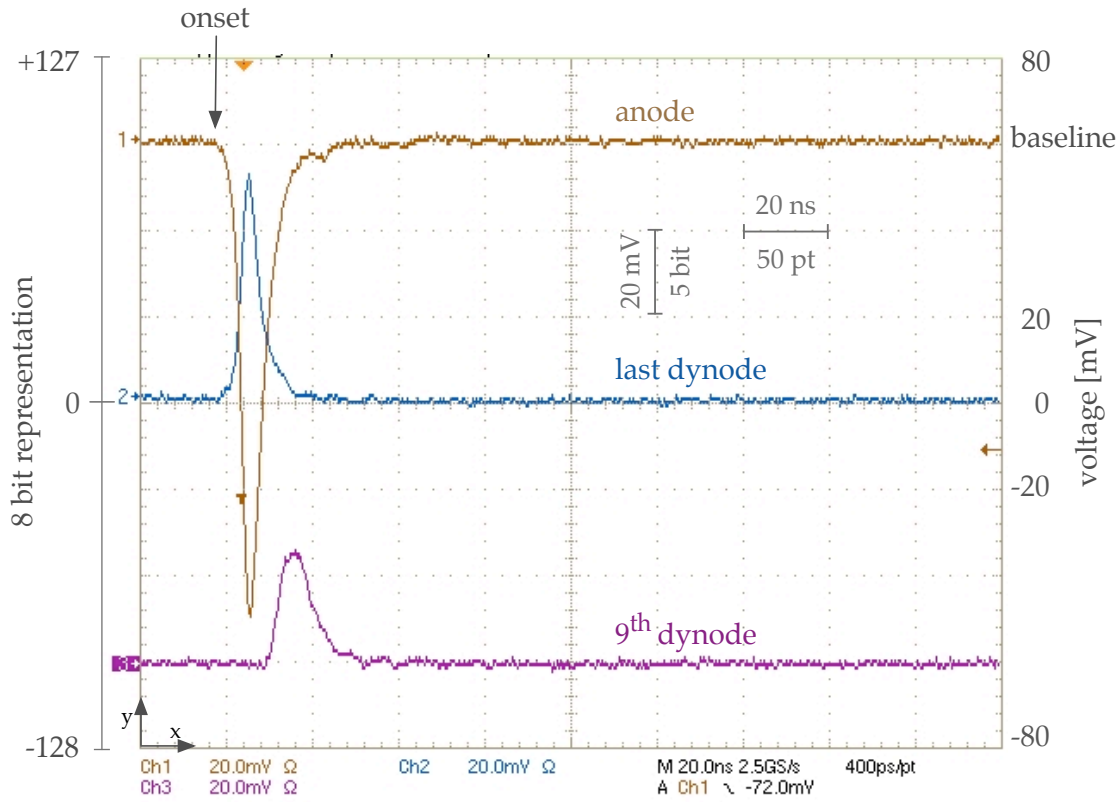

Figure 5.1: Screenshot from the digital oscilloscope, showing the signal from the anode, the last (12^{th}) dynode and the 9^{th} dynode. The axis on the right shows voltages, the axis on the left shows the char values these voltages will be represented by in the data file.

Intensity
50
60
70
80
5000
10000
15000
20000
25000
30000

its exact position. The baselines are not set on 0 V, because when a pulse's height does not fit onto the screen, it is cut off at the top (or the bottom as might be the case). It is desirable to record intact pulses over a large range of intensities, therefore the baseline of the anode signal is moved near the upper limit of the screen, while the baseline of the dynode signal is set near the bottom of the screen. Pulses from both channels then have the full range of the screen available.

In order to later calculate a spectrum from the data, which entails integrating over the pulses, all baselines should, however, be at 0 V. Furthermore, in order to calculate an average pulse shape, all the onsets should be at the same position in time.

These corrections are done offline by a C++ program that makes use of the root frameworks. It reads in one signal at a time and calculates its baseline and the onset of the pulse in it. It is not sufficient to calculate them once and then use the same values for all the signals in the file, because the baseline as well as the onset position can fluctuate from signal to signal. The fluctuation of the baseline might be caused by fluctuations in the high voltage supply, the oscilloscope or the PMT, while the fluctuation of the onset position has to do with the choice of the trigger voltage (see next section).

The baseline is calculated by taking the average value over the first few hundred data points, where no pulse is expected. The baseline value is then subtracted from all the data points, effectively shifting the baseline of the pulse to 0 V. Anode signals are in addition inverted, so that all the pulses are positive on the y-axis.

The onset of the pulse is then calculated with the following algorithm:

1. Go through the data points until one is larger than *thresh*
2. Take the average over the following hundred data points
3. If this average if also bigger than *thresh*, accept the starting point as the onset
4. Else:
   (a) If half the data points are past and no onset was found, label the signal as noise and jump to the next one
   (b) Else, continue at step 1.

thresh is adjusted manually for each data file. To do that, only a few signals are read and drawn together with the pulse onset positions. The value of *thresh* is adjusted until the onsets fit the pulses properly.

The pulse onset value in each signal is written to a root histogram.

The baseline is now calculated once more, this time taking the average over a few hundred data points before the onset. The idea is that no pulse was found in that area, so there must be only baseline. There might well have been some remains of a pulse or some noise in the area that was used to calculated the baseline before. This possibility is mostly excluded now.

The baseline value is written to a histogram, and additionally the data points from the area where the baseline was calculated are all written into another histogram.

The histograms written so far are used to diagnose possible problems with the evaluation or with the data itself. The onset and the baseline histograms should each have one narrow peak. If there is a big spread in the onset histogram, the value of *thresh* needs some more adjusting. A small spread is normal, since sometimes there are noise pulses starting earlier than the real pulse. The baseline histogram might show some spread if by accident there was still some noise in the area of baseline calculation.[1]

The histogram of 500 baseline points from each signal is interesting, because it shows the width of the baselines of the single signals as well as the baseline position spread from signal to signal. It is shown in figure 5.3.

Those histograms are also used to choose nominal values for the baseline and the onset. In the next run of the program, if a signal's baseline or onset is outside of those values, it is discarded as noise. Otherwise, its integral is calculated and written into a spectrum histogram. In addition a "fast to total" scatterplot can be drawn.

Inspection of the spectrum reveals the expected peaks from the inserted sources and usually some background muons, muon induced showers, compton scattered photons and general radioactive background. For the calculation of an average pulse shape, only those signals whose energy identifies them as belonging to the expected peak are used, with the possibility to further take only those whose "fast to total" ratio is in a certain range.

The spectrum deserves further elaboration: The unit on the x-axis is the sum over all the voltages which make the pulse, in their digital representation as they are sampled by the digital oscilloscope. I will call these numbers "channel numbers", even though the "channels" are only imposed on the data by the software evaluation. The actual voltage a channel number corresponds to is determined by the voltage scale that was set on the oscilloscope for the measurement; the conversion factor is quoted on the axis.

The channel number corresponds to a certain energy deposit in the detector, because the total measured voltage is proportional to the number of photo electrons originally liberated at the cathode of the PMT, which is proportional to the number of scintillation photons, which are in turn proportional to the energy deposit.

In the end up to four cuts are applied to the data, restricting the onset position, the baseline position, the energy and the "fast to total" ratio. Figure 5.4 shows the spectrum, onset and baseline histograms for a data file taken with an Americium-241 γ source inserted in the system. The red dashed lines represent the cut values; all pulses with a value outside of those lines are discarded.

5.3 The average pulse shape

To get the average pulse shape, the intensities at equal times (with the onset as reference) of the signals that survive the cuts are added and the result is divided by their number.

[1] The onset finding algorithm only finds pulses if their intensity is high enough, so it can still miss some noise.

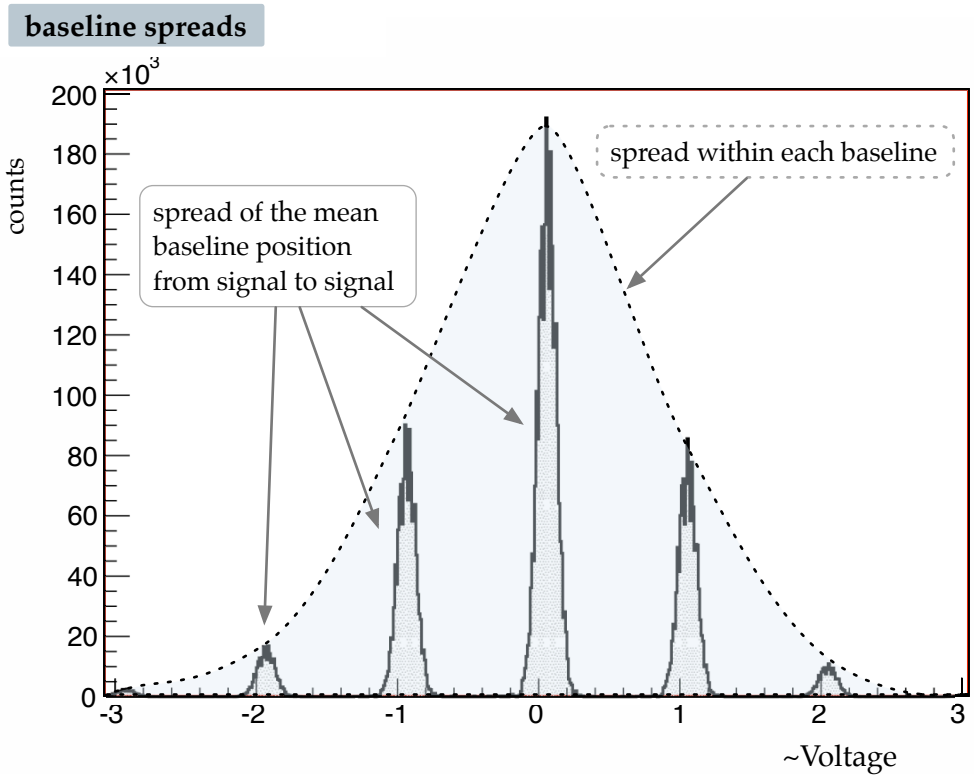

Figure 5.3: Histogram of the values of 500 baseline points from 20000 signals, after correcting the signal for the baseline position. The x-axis is proportional to a voltage as quantified by the oscilloscope's representation as number of type char. Since the entries are corrected data points from the baseline, they should all be close to zero, but the baseline is not perfectly zero, therefore there is some spread. Entering 500 baseline points from only one signal into the histogram results in discrete bars following the shape of the dotted curve. The extend to which this curve spreads above and below zero is thus the width of the baseline in a single signal. The more sets of baseline points from other signals are added, the clearer do the narrow peaks close to the integer char values manifest themselves. They are spread around integers, because the possible baseline values are recorded with numbers of type char, so they are always integer. However, after subtracting the mean value of the baseline, which is not an integer, each point is shifted by the same amount from an integer number. If the mean value of the baseline varies a lot from signal to signal, then those separate peaks grow wider. If the mean baseline value is nearly the same for every signal in the file, then the peaks are very narrow..

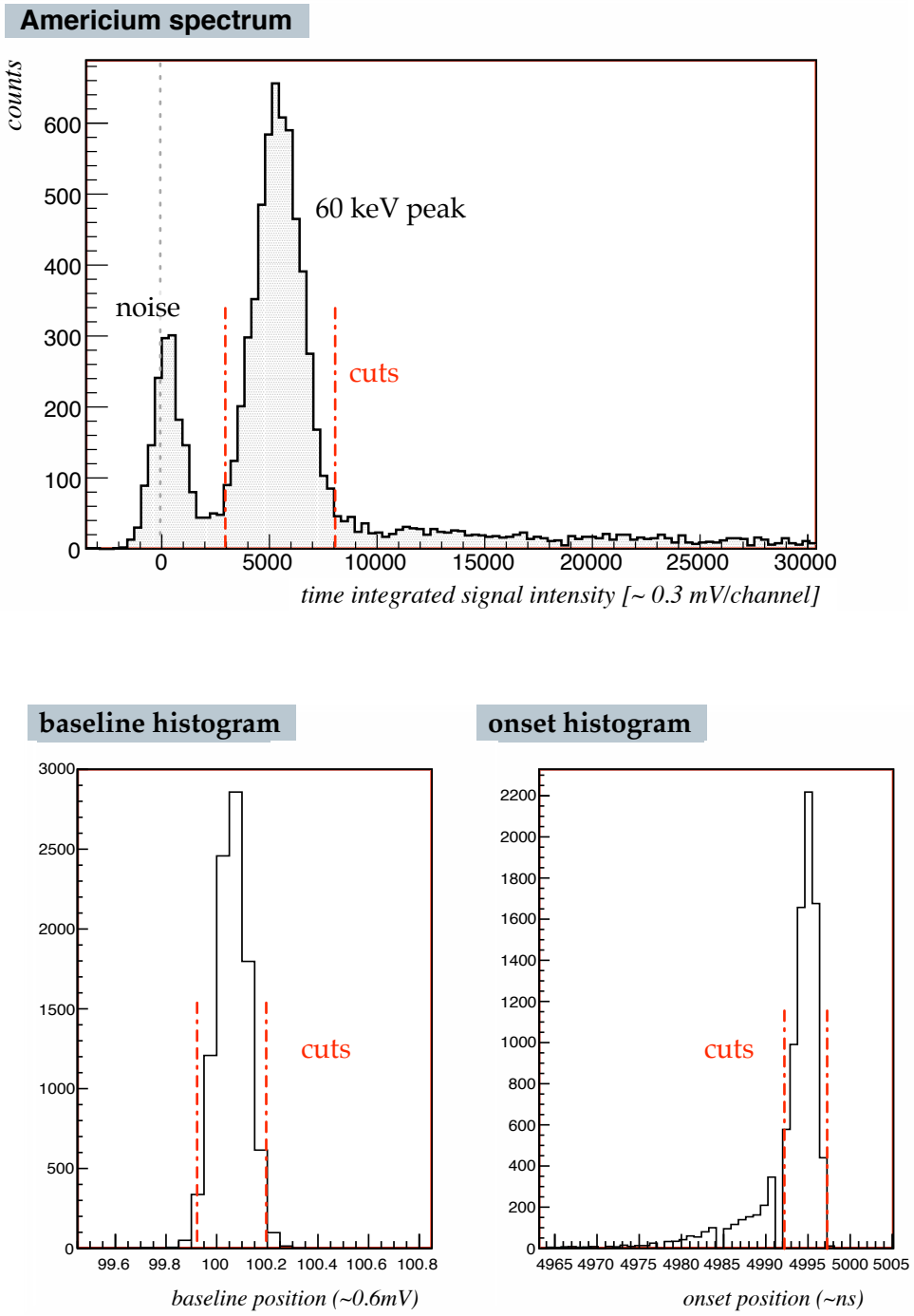

Figure 5.4: The cuts applied to a data file that was recorded with Americium-241 in the system.

A new histogram so that the first 250 time bins (equal to 100 ns) are again baseline. This serves as a safety measure, because if the baseline is not found to be at zero intensity something certainly went wrong in the data evaluation.

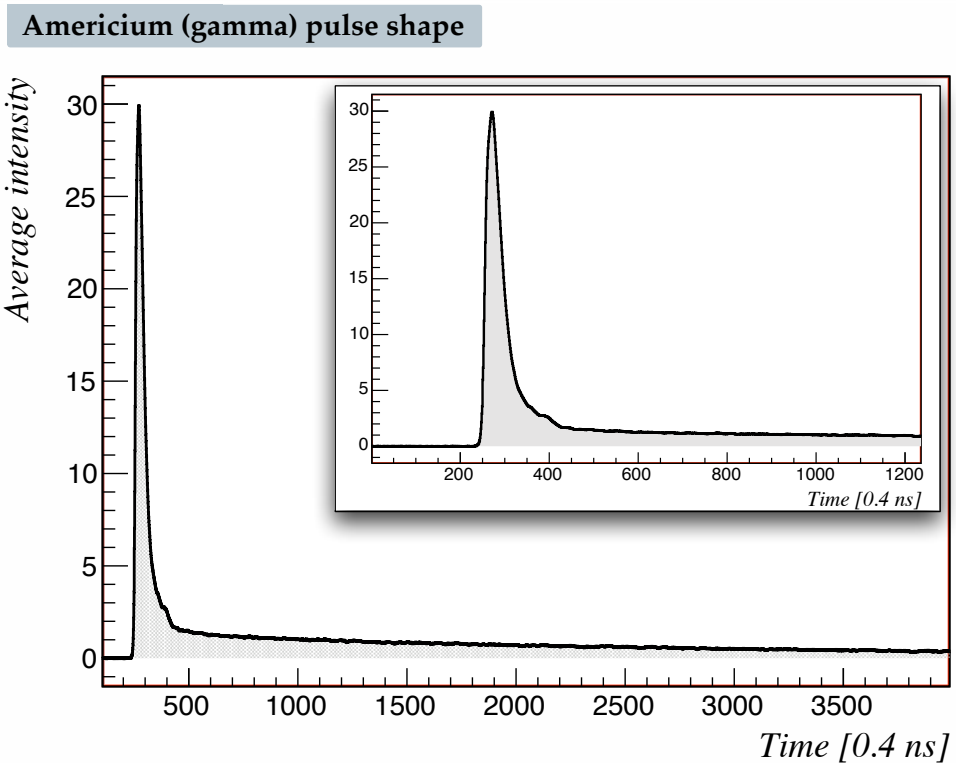

Figure 5.5: Gamma radiation pulse shape from an Americium-241 source, with the cuts from figure 5.4. The inlay shows only the first 480 ns of the same pulse.

There are some things to keep in mind when considering those average pulse shapes.

- The determination of the onset is in some ways problematic. The first data entry that is higher than some threshold is taken for the onset, if the mean of the following hundred entries is also above that height. This algorithm finds pulses reliably, but a high energy pulse will be given a sooner onset than a low energy pulse with the same PDF, even if they actually started at the same time offset within their signal. If the average pulse shape is calculated from a wide range of energies, this will smear out the peak, making it wider than it should be.

  A different approach is to try and find the peak positions of the pulse in each signal and to use those as reference instead of the onset. But finding the peak position is difficult in the jagged pulses dominated by statistical fluctuations, as we see them even at an energy of 60 keV (compare figure 5.2). Even if all of the peak positions could be identified with little uncertainty, a problem remains: actual differences in

the rise-times of the pulses would be hidden by this method.

Yet another approach is to take as onset the time when a certain percentage of the full intensity is reached. This, again, should work fine for high energy pulses (e.g. 5.5 MeV alpha pulses), but will yield just as much uncertainty for lower energy pulses (e.g. 238 keV gamma pulses) as the method employed now does.

- The slow component of the pulse is eventually lost in the background noise. This happens at different times for pulses from particle kinds with different R-values (equation 2.1 on page 9).
- The PMT is not perfectly linear with the signal intensity.

The theoretical pulse shape plots always showed the probability distribution function, so that they represented the emission probability at a given time. The same can be achieved for the average pulse shapes by normalizing the area under them to one. They then show a normalized intensity, which is nothing but the emission probability. With the normalization to one, all energy information is lost, so that pulses at different energies are now easily comparable. Figure 5.6 shows such normalized pulse shapes for alpha, gamma and neutron radiation. The cumulative distribution functions (compare equation3.13) are shown, too.

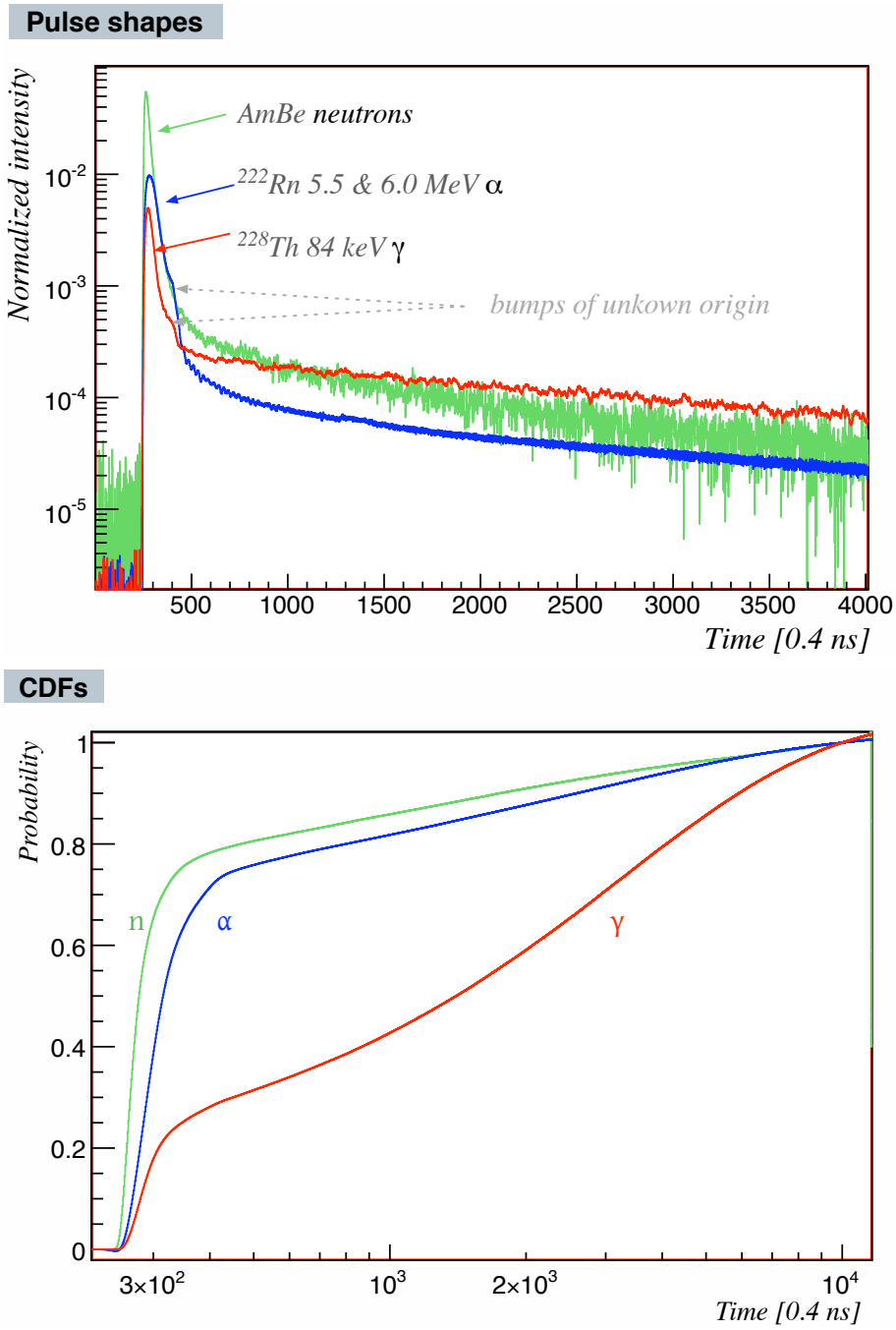

Figure 5.6: Average pulse shapes of α, γ and neutron radiation. Top: PDFs. Bottom: CDFs. The features, especially the elevation at the foot of the gamma and the alpha pulse shape peaks, will be discussed in the next chapter.

Chapter 6

Pulse shape analysis

6.1 The pulse shape: revisited

The average pulse shapes extracted from the data files only have a remote resemblance to the photon emission PDFs from 3.1 on page 14. They differ in the actual shape as well as in the parameters (lifetimes and ratios R).

The pulse shape parameters strongly depend on the purity of the argon; the presence of impurities even on the ppm level has considerable impact on the measured lifetimes through the photon quenching processes described in section 2.2 on page 11. It can therefore not be expected that the parameters as they were measured in a different experiment are valid for this setup. This is especially true for the slow component, which is affected more strongly by impurity quenching than the fast component is.

The change in the actual shape is due to detector effects, which were neglected before but play a big role now. A photon detection PDF that accounts for these effects will be developed by considering the different steps a photon goes through on its way from emission to detection, figure 6.1:

A photon that is produced at time t is absorbed and re-emitted by the WLS which has a life-time of τ_{wls}. With a certain probability it then induces an electron shower in the PMT that has a time spread δt by the time it reaches the anode. This means that there is no unique relation between the time we register a photon and the time it was emitted anymore - the signal is smeared out. The manifestation of this is most evident at the beginning of the pulse and throughout the fast component. It does not play an important role in the slow component of the pulse, since τ_s is much longer than τ_{wls} or δt are.

The first step, absorption by the wavelength shifter and subsequent re-emission, after which the photon distribution follows the intermediate PDF $p^{(2)}(t)$, can formally be treated by writing down rate equations:

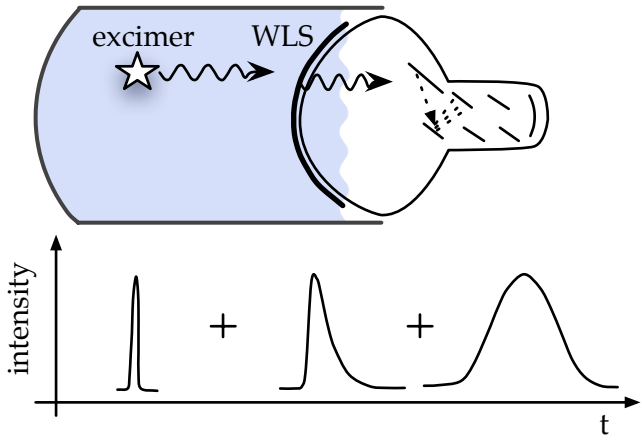

Figure 6.1: From photon emission to photon detection. The graphs show the PDFs pertaining to the detector components.

$$\frac{\partial}{\partial t}[(Ar_2^*)_s] = -\frac{1}{\tau_s}[(Ar_2^*)_s] \tag{6.1}$$

$$\frac{\partial}{\partial t}[(Ar_2^*)_t] = -\frac{1}{\tau_t}[(Ar_2^*)_t] \tag{6.2}$$

$$\frac{\partial}{\partial t}[WLS^*] = \frac{1}{\tau_s}[(Ar_2^*)_s] + \frac{1}{\tau_t}[(Ar_2^*)_s] - \frac{1}{\tau_{WLS}}[WLS^*] \tag{6.3}$$

and (6.4)

$$\frac{\partial}{\partial t}[\gamma] = p^{(2)}(t) = \frac{1}{\tau_{wls}} \cdot [WLS^*] \tag{6.5}$$

With initial conditions that

$$\frac{[(Ar_2^*)_s](t=0)}{[(Ar_2^*)_t](t=0)} = R \tag{6.6}$$

and

$$[(Ar_2^*)_s](t=0) + [(Ar_2^*)_t](t=0) = 1 \tag{6.7}$$

to ensure normalization.

Solving the equations one obtains:

$$p^{(2)}(t) = \frac{1}{\tau_{wls}}\Big[\frac{R}{R+1}\frac{\tau_{wls}}{\tau_s - \tau_{wls}}e^{-t/\tau_s} + \frac{1}{R+1}\frac{\tau_{wls}}{\tau_t - \tau_{wls}}e^{-t/\tau_t} + \tag{6.8}$$

$$+ \frac{1}{R+1}\big(R \cdot \frac{\tau_{wls}}{\tau_{wls} - \tau_s} + \frac{\tau_{wls}}{\tau_{wls} - \tau_t}\big)e^{-t/\tau_{wls}}\Big] \tag{6.9}$$

Photons with the distribution $p^{(2)}(t)$ reach the photo cathode of the PMT inducing the emission of photo electrons. A single photo electron emitted from the cathode leads to a gaussian signal at the anode. The PDF $p^{(2)}(t)$ thus has to be convoluted

with a gaussian to obtain the PDF $p^{pulse}(t)$ that describes the pulse shape seen on the oscilloscope. Following the calculations by Gale[19] one obtains:

$$\begin{aligned} p^{pulse}(t) &= \int_{-\infty}^{\infty} p^{(2)}(t') \cdot \frac{h}{\sqrt{\pi}} e^{-h^2(t'-t)} dt' \\ &= \frac{1}{2}\frac{1}{\tau_{wls}}\Big[\frac{R}{R+1}\frac{\tau_{wls}}{\tau_s - \tau_{wls}} e^{1/(4(\tau_s \cdot h)^2) - t/\tau_s} \cdot \{1 - erf(\frac{1}{2\tau_s h} - ht)\} + \\ &\qquad \frac{1}{R+1}\frac{\tau_{wls}}{\tau_t - \tau_{wls}} e^{1/(4(\tau_t \cdot h)^2) - t/\tau_t} \cdot \{1 - erf(\frac{1}{2\tau_t h} - ht)\} + \\ &\qquad \frac{1}{R+1}\Big(\frac{R\tau_{wls}}{\tau_{wls} - \tau_s} + \frac{\tau_{wls}}{\tau_{wls} - \tau_t}\Big) e^{1/(4(\tau_{wls} h)^2) - t/\tau_{wls}} * \\ &\qquad \{1 - erf(\frac{1}{2\tau_{wls} h} - ht)\}\Big] \end{aligned} \tag{6.10}$$

with the square of the standard deviation $\sigma^2 = 1/(2h^2)$.

Strictly speaking, $p^{pulse}(t)$ is no longer a photon PDF, but a photo electron PDF, since it describes the time distribution of the photo electrons that are detected.

Many effects that change the pulse shape have still been neglected. There is the additional spread caused by scintillation photons that are reflected several times before reaching the PMT. There is also the nonlinear behavior of the PMT with increasing light intensity and the fact that some photo electrons reach the anode early or late (pre- and after-pulses) because they do not take the regular path there. This latter effect is probably absorbed in the photo electron spread and the WLS decay time parameter.

In the following section, the results of fitting the experimental pulse shapes with the here developed PDF is presented.

6.2 Fitting the pulse shape

6.2.1 The fit routine

The PDF $p^{pulse}(t)$ depends on five variables and it should be possible to reproduce each of the three experimental pulse shapes in their normalized form of figure 5.6 with the right choice of those variables' values. Three of the variables however cannot be chosen freely, because they are independent of the exciting radiation and thus should have the same value for all three pulse shapes; those are the decay times of the singlet and triplet excimers, τ_s and τ_t, and the decay time of the wavelength shifter, τ_{WLS}.

The two remaining variables R and σ have unique values for each particle kind's pulse shape. The ratio of singlet to triplet excimer number R was the sole variable causing the theoretical pulse shapes to differ (compare chapter 3). The variable σ, the time spread of the photo electrons in the PMT, now also contributes to making the pulse shapes differ and this is a direct consequence of the different R values. The time spread of the photo electrons grows larger the more of them travel from cathode to dynode at the same time. At the same total energy, pulses with a large R value have more intensity in the fast singlet component than such with a small R, leading to more photo electrons liberated

in a short time interval[1]. A large value of R thus induces a large value of σ. In addition, the energies of the neutron, gamma and alpha radiation from which pulse shapes were recorded were very different, so that different numbers of photo electrons were present at the same time anyway. This breaks the dependency of σ on R, because the difference in energy between neutron and alpha induced events is much larger (about a factor of 10^4) than their difference in R (a factor of 2.3).

Another new variable, $shift$, accounts for the pulses not starting at 0 ns in the files. The pulses' onsets as determined by the software (see section 5.3) is at time bin 250 (100 ns), but this is not necessarily the start time as it is defined in the PDF, so t is replaced by $(t - shift)$ in equation 6.10.

No scaling variables were used in the fit. Since the PDF $p^{pulse}(t)$ is normalized and the pulse shapes are normalized, they should fit together without scaling one of them, as long as the normalization factors were calculated correctly and the theory is right. This approach is different from the one Hitachi et al.[58] and others took when fitting their pulse shapes to determine the R values and excimer lifetimes. They assumed a generic double exponential function, modified by Gale's equation to account for the apparatus function (photo electron time spread), with arbitrary amplitudes A and B of the exponentials.

There are now three data sets and 12 variables to fit to them. One of the variables, τ_t, is special because it alone governs the behaviour of the pulses at late times. The photon pulse shapes have the strongest triplet excimer contribution, so the triplet decay time was obtained by fitting a simple exponential function

$$f(t) = A \cdot e^{-t/\tau_t}$$

to the tail of the gamma pulse shape. The result of the fit was assumed as the start value of τ_t and the variable was only allowed to vary within 5% of this.

The fits were done with three instances of the PDF equation 6.10, so that each of the three particle kinds had its own set of R, σ and $shift$, but they all shared the same τ_s, τ_t and τ_{WLS}.

A custom χ^2 function that consisted of the sum over the three separate χ^2s for gamma, alpha and neutron pulse shape

$$\chi^2 = \chi^2_\gamma + \chi^2_\alpha + \chi^2_n \tag{6.11}$$

was then minimized. The separate χ^2 functions do not take into account statistical uncertainties in each bin, because the measured pulse shapes are analog ones[2], so it is not easily possible to find out how many photo electrons the intensity in each bin corresponds to, and thus not possible to determine a statistical uncertainty. A regular χ^2 function with equidistant sample points and all bin errors equal to one did not lead to variable values that fit the peak well, even though the value of χ^2 was fine. It behaved

[1]The decay time of the singlet excimer is comparable to the time spread of the photo electrons. The triplet excimer's decay time is so much longer that the photo electron time spread becomes negligible.

[2]They are analog in the sense that instead of counting each photo electron, an analog voltage is measured (which is then digitized by the oscilloscope).

that way because many more points were taken from the tail than from the peak, so that the tail had more weight in the value of χ^2. The situation was remedied by leaving out the normalization completely, so each separate χ^2 function looked like

$$\chi^2 = \sum_{i=0}^{N} (y_i - \overline{y}_i)^2 \tag{6.12}$$

with the value in each bin, y_i, and the value of the fit function at this bin, $\overline{y}_i$. This modification does not change the position of the minimum, but the value the χ^2 function has in the end is without statistical meaning, therefore it is not quoted. The outcome of the fit shown in figure 6.2 and table 6.1 lists the variables, their meaning and the fitted values.

Variable name	**meaning**	**fitted value**
Global variables		
τ_s	singlet state decay time	8.8 ±5.6 ns
τ_t	triplet state decay time	1.21 ±0.27 μs
τ_{wls}	WLS decay time	1.5 ±1.5 μs
V*variables specific to gamma pulse shape*		
R_γ	singlet/triplet ratio	0.28 ±0.12
σ_γ	photo electron spread	4.2 ±2.8 ns
shiftγ	onset of pulse in file	bin 265 ±10
Variables specific to alpha pulse shape		
R_α	singlet/triplet ratio	1.87 ±0.71
σ_α	photo electron spread	6.7 ±1.6 ns
shiftα	onset of pulse in file	bin 269 ±22
Variables specific to neutron pulse shape		
R_n	singlet/triplet ratio	3.0 ±0.8
σ_n	photo electron spread	1.5 ±1.2 ns
shift$n$	onset of pulse in file	bin 252 ±4

Table 6.1: The results of a global fit to the gamma, alpha and neutron pulse shapes. The three global variables are shared between the pulses, the others are specific to a certain particle's pulse shape. The χ^2 quoted is the mean over the three χ^2 values of the gamma, alpha and neutron pulse shape fit divided by the number of degrees of freedom. Compare to table 2.2 on page 9

.

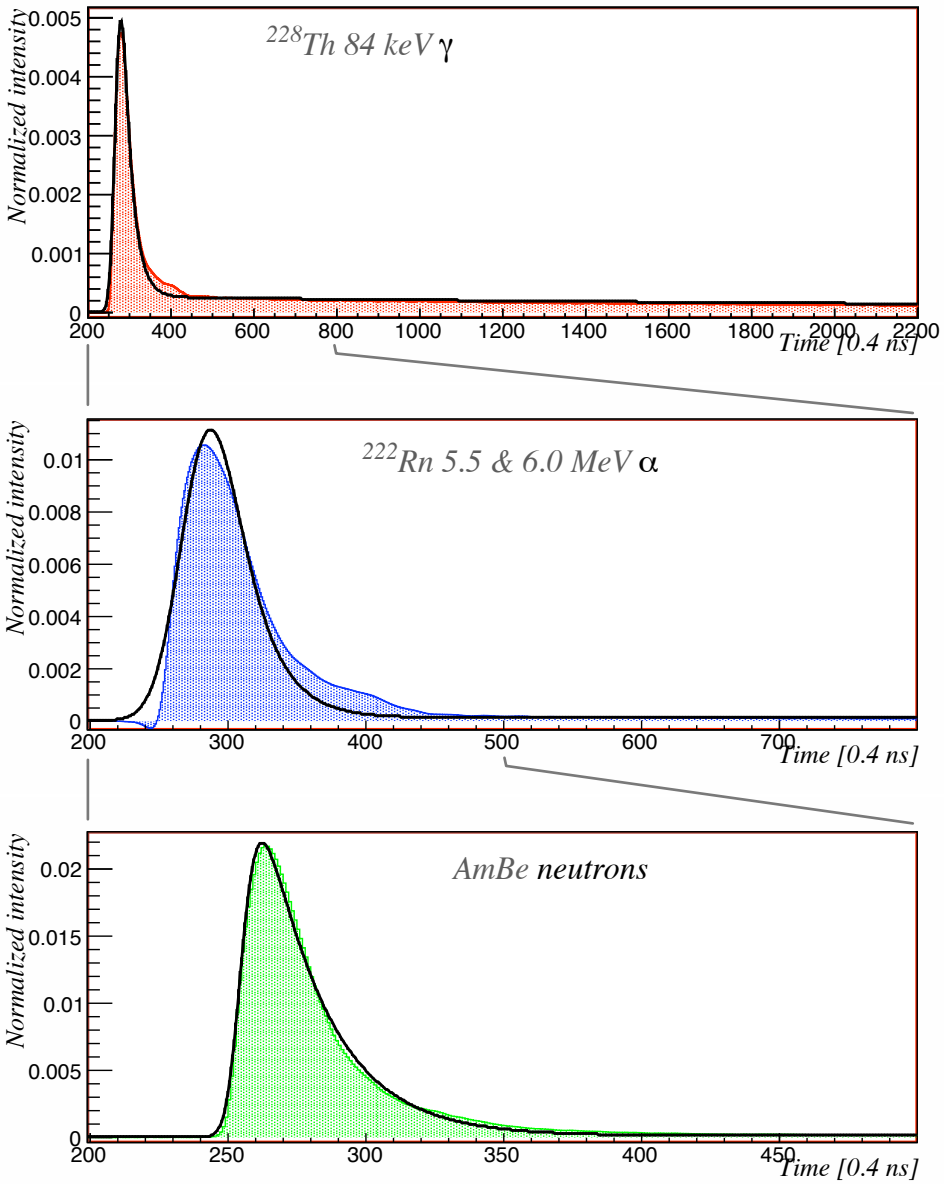

Figure 6.2: The gamma, alpha and neutron pulse shapes and the fitted functions $p^{pulse}(t)$ with the variables of table 6.1. The x-(time)-axes are different to account for the different strengths of the triplet excimer, allowing to see the most relevant parts of the pulses. Refer to figure 5.6 to see all three pulse shapes in the same scale.

.

6.2.2 Discussion

Visual inspection of the agreement between the theoretical curve and the pulse shapes indicates that the fit works rather well for the neutron pulses, and would work even better for the gamma pulse shapes if the small elevation at the foot of the peak was not there. This elevation can be seen in the alpha particle pulse shapes as well, but could not be explained. Similar findings were reported in literature for gamma[22][58] as well as for alpha[59] pulse shapes without an explanation given.

This second bump is seen in all the measured gamma pulse shapes, from 60 keV to 2.6 MeV without any appreciable energy dependence. There is only a hint for an elevation at the foot of the neutron pulse shape peak, but that pulse shape was made from only a few dozen events, while the other pulse shapes are averages over several thousand events, so that it remains uncertain whether a feature might arise with better statistics. Close inspection of the pulse shapes published in ref.[58] shows that there the elevation occurs for gamma and alpha as well as for fission fragment excitation, but their statistics are also rather poor. The hint of an elevation could be caused by a few gamma events that the discrimination missed.

The fit fails for the alpha pulse shape. This pulse shape was calculated from data taken at the dynode[3], but the shape of the actual pulse after the onset is the same at readout from the anode and from the dynode. The fit does not converge to different values when the lower limit is fixed after the dip. The shape can be fitted well, obtaining a smaller value of χ^2, if all parameters are decoupled, that is if the alpha pulse shape is fitted by itself and gets its own set of all 6 variables. That fit is however highly unstable under slight variations of the start values and the variables then show a strong correlation. It can also be fitted well if arbitrary scale factors are used for the amplitude of the different exponentials.

This either means that the decay times of the excimers and the wavelength shifter are different under alpha particle excitation than they are under gamma or neutron excitation (which is very unlikely), or that some physical process is different, ie. $p^{pulse}(t)$ is not the right PDF. Despite this, the values of R_α and σ_α converge to reasonable values.

As expected the σs go with the energy of the events, with σ_n having the smallest and σ_α the largest value.

Some of the errors on the fitted values are rather large. This is because several variables, most notably those that govern the shape of the peak - σ, tau_s and τ_{WLS} - are correlated, but this correlation cannot be broken with the available data. An independent measurement of τ_{WLS} and σ would prove useful here. A limited measurement of σ could be done using the calibration LED (see figure 4.1) but the energy reached was nowhere near even that of the neutron events.

[3]This is the reason for the dip below zero before the onset of the pulse. All pulses taken from the dynode have that feature. It can be traced back to the capacity over which the signal is read out, which forms a resonant circuit with other electronic components. Compare section 4.3

6.3 Pulse shape discrimination study on experimental data

6.3.1 Preamble: Photo electron yield and quenching

One is usually concerned with the question of what discrimination power is possible with a given energy deposit in the detector, or what energy deposit is necessary to guarantee a certain discrimination power. The answer depends on how many photons are emitted due to this energy deposit, because the discrimination power depends on the number of photons in a pulse (compare chapter 3 on page 13). But what we actually measure are photo electrons, so the quantity of interest is the photo electron yield.

The photo electron yield is an important property of every scintillation detector. It is defined as the number of photo electrons produced per unit deposited energy. This is proportional to the number of photons emitted by the scintillator, since photons liberate photo electrons from the photo multiplier cathode with a fixed probability. In equations:

$$Y = \frac{N_{pe}}{E_{dep.}} \tag{6.13}$$

$$N_{pe} = \eta N_{ph} \tag{6.14}$$

With

Y photo electron yield

N_{pe} number of photo electrons

$E_{dep.}$ deposited energy

N_{ph} number of photons

η fraction of photons that liberate a photo electron (quantum efficiency).

Making this more complicated is the fact that at the same energy deposition in the scintillator, the number of scintillation photons available to liberate a photo electron is not the same under excitations with particles of different LETs (see section 2.2 on page 7). The photo electron yield therefore also depends on the LET. For different kinds of exciting radiation this is plotted in figure 6.3 (adapted from ref.[54] and [56]). The plot is normalized to the photo electron yield of relativistic Lanthanum ions.

6.3.2 Measured photo electron yield and alpha quenching factor

The photo electron yield Y_γ of the LArGe setup under excitation with photons is

$$Y_\gamma = 1243 \pm 27 pe/MeV.[63] \tag{6.15}$$

This value was calculated by fitting a single photo electron (SPE) spectrum and the 123 keV ^{57}Co peak. This yields two channel numbers, Ch^{SPE} and Ch^{Co} and the photo electron yield is then:

$$Y = \frac{Ch^{Co}}{Ch^{SPE} \cdot E^{Co}} \tag{6.16}$$

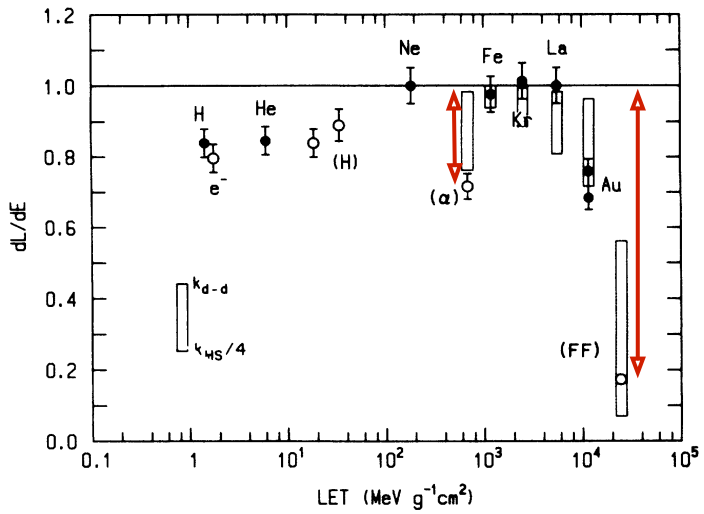

Figure 6.3: Quenching factors from ref.[54],[56]; filled circles are for relativistic, open circles for non-relativistic velocities. The largest number of scintillation photons are emitted under excitation of relativistic Lanthanum, the plot is therefore normalized to that number. Under excitation of non-relativistic fission fragments less than 20 % of that number is reached.

With E^{Co} equal to the 123 keV peak energy of the ^{57}Co peak.

Figure 6.4 serves a dual purpose, first for a rough calculation of the alpha quenching factor, and then to demonstrate the discrimination power of the "fast to total" and the Gatti filter. The top of figure 6.4 shows a scatterplot with the discrimination parameter D_{ft} on one axis and the energy of the pulse on the other (in channel numbers, see section 5.2 on page 39 for an explanation of their meaning). The bottom plot is just the spectrum, it can be seen as a projection of the scatterplot onto its x-axis.

In the linear range of the setup, there is a linear correlation between channel number and energy.

$$E = m \cdot Ch \tag{6.17}$$

The conversion factor m can then be found by inserting a source with a line at a known energy E^{source} into the system and finding the channel number Ch^{source} of the peak. Then

$$m = \frac{E^{source}}{Ch^{source}}. \tag{6.18}$$

Generally, the channel number zero does not coincide with zero energy deposit, so that the relation between energy E and channel number Ch becomes

$$E = m \cdot Ch + \text{offset}. \tag{6.19}$$

In that case, the source must have at least two lines at known energies so that m as well as the offset can be calculated.

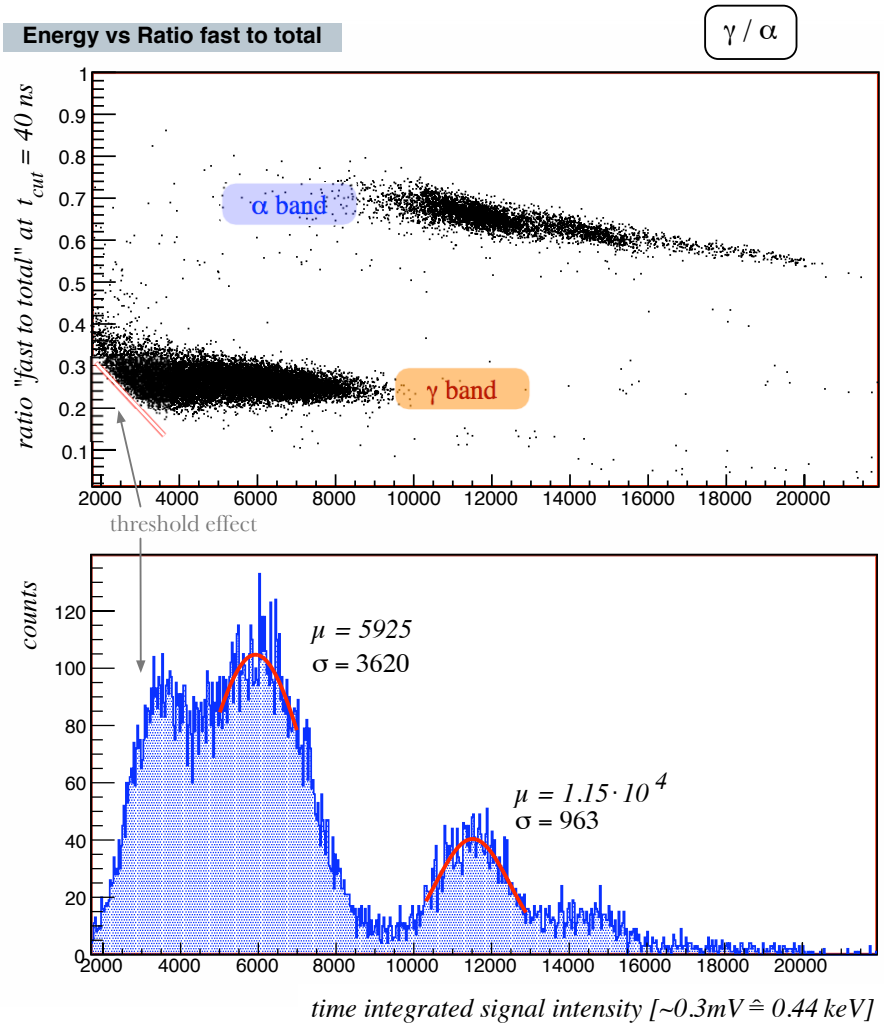

Figure 6.4: Top: Scatterplot showing the γ and the α bands, compare figure 3.4 on page 21. Bottom: The spectrum showing 4 peaks: the first peak is not actually a peak, but an artefact of the trigger threshold, the second peak is from the 2.6 MeV gamma of the ^{228}Th chain, the third peak is from the 5.5 and 6.0 MeV alphas of the ^{222}Rn chain (not resolved), and the last peak is the remaining 7.68 MeV alpha. The spectrum can be seen as a projection of the top scatterplot onto the x-axis.

The offset can be influenced by the parameters used in the data evaluation, namely the time window used for the integration and the baseline determination. The program was optimized for gamma pulses and a 10 mV scale on the oscilloscope in such a way that the offset is nearly zero. This is demonstrated in figure 6.5.

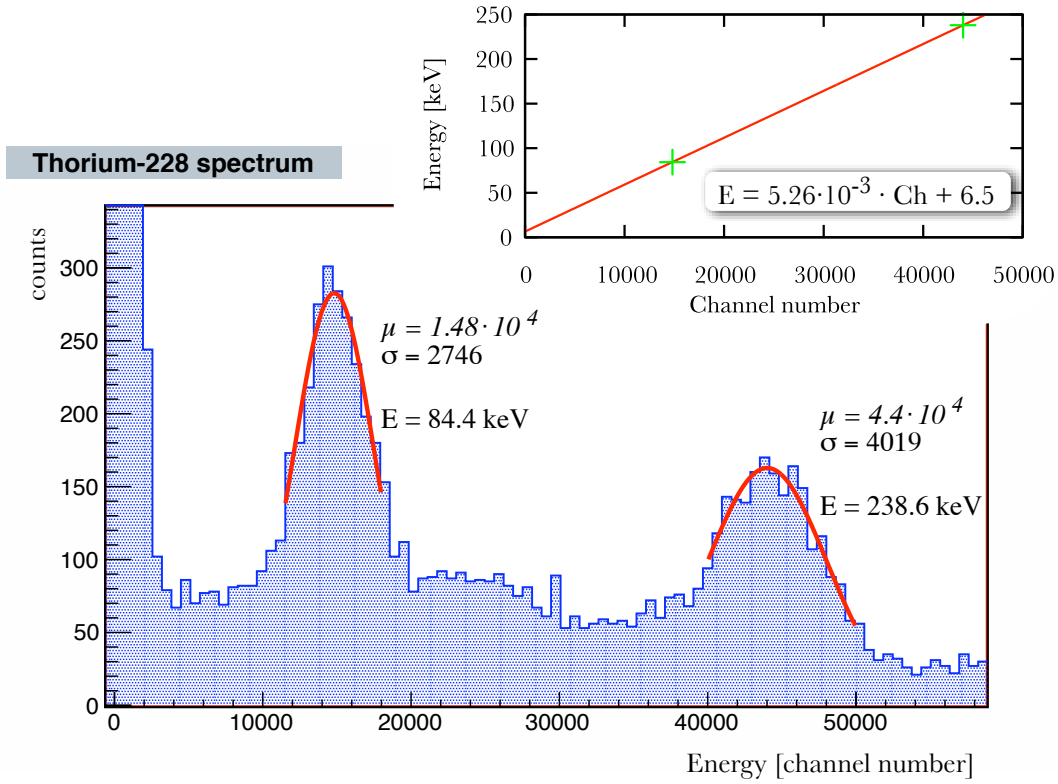

Figure 6.5: ^{228}Th spectrum with fits of the peaks and an illustration of the linearity between channel number and peak energy.

Back to the spectrum of figure 6.4:

The first peak is not due to any radiation with that energy. It is a "pseudo peak" that arises because of the position of the trigger threshold on the oscilloscope. This is clear from the scatterplot representation where the lower part of the band in that energy region is cut off, because at the same total intensity, those pulses with a more intense fast component will set off the oscilloscope trigger when those with a weaker fast component are already ignored. The oscilloscope trigger thus shows in the scatterplot as a sloped line below which there are no events.

The second peak is actually a compton edge from the 2.6 MeV gammas of the ^{228}Th chain (compare figure 4.2 on page 36), and the energy deposit in the detector is most likely less than 2.6 MeV, because many of the gammas do not get stopped completely

in the active volume.

The third peak is a superposition of the peaks from the 5.5 and 6.0 MeV alphas of the ^{222}Rn chain (compare figure 4.3 on page 37). Due to bad statistics, those peaks are not resolved[4].

The last peak is from the 7.68 MeV alpha of the ^{222}Rn chain.

With this information, it is possible to estimate the quenching factor the following way:

Using equation 6.17 and the 2.6 MeV gamma peak's compton edge one obtains

$$m = 0.44\ [\frac{keV}{Ch}]. \tag{6.20}$$

This is only an upper limit, because the actual energy deposit is unknown, but certainly less than 2.6 MeV

The channel number $Ch = 1.15 \cdot 10^4$ corresponds to an energy of $E = 5073keV$ in this scale. The actual alpha particles that caused the peak have a mean energy of 5740 keV, so that the quenching factor for alpha particles in the gamma energy scale is

$$Q_{alpha} = \frac{E_{detected}}{E_{deposited}} \leqslant 0.88 \tag{6.21}$$

A more exact calculation with higher statistics, taking into account offsets, yields

$$Q_{alpha} = 0.72 \pm 0.03 \quad [63] \tag{6.22}$$

6.3.3 "Fast to total" filter

The scatterplot of figure 6.4 was done using the "fast to total" filter. To see how well this filter performs it is again useful to project a certain energy range of the scatterplot onto the y-axis. This is shown in figure 6.6 for the range of channels $[3000, 20000]$ corresponding to a range of photo electrons of $[2500, 8000]$. The two bands do not overlap, so the discrimination power is very good; this will be quantified in the next section.

The situation is different when considering γ against neutron events. At the low energies of the neutron events, the bands overlap considerably. In order to get an idea of how many γ-like events lie in the neutron band, one can take data without the neutron source but otherwise under the exact same conditions. This data was taken with an additional shielding of borated polyethylene around the detector to absorb neutrons and is drawn in red in figures 6.8 and 6.9, where the data from the mixed file is drawn in blue.

[4]The two peaks are resolved in the spectrum of figure 7.12 on page 92, where the statistics as well as the resolution is better.

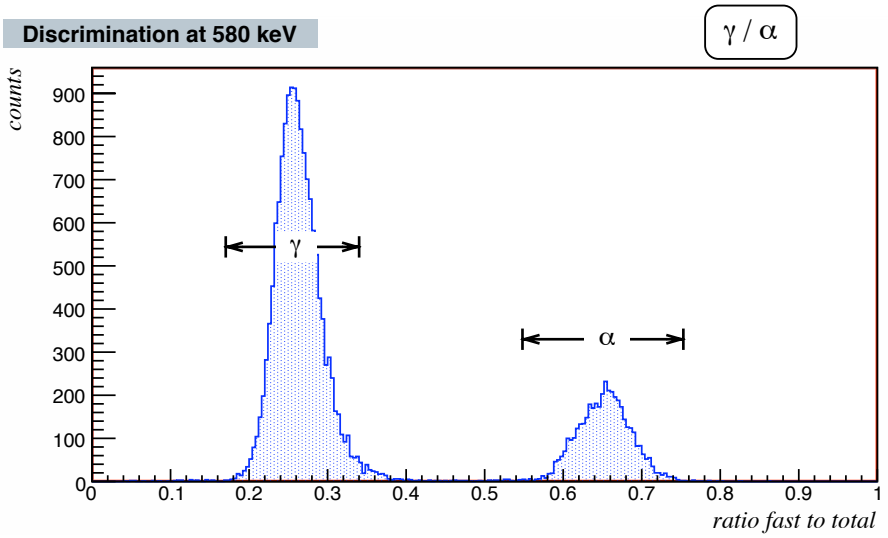

Figure 6.6: This is a projection of the scatterplot in figure 6.4 onto the y-axis, similar to the top plots of figures 3.6 and 3.7 on page 25. Unlike in those plots, where slices of an equal number of photons (or in the new terminology, photo electrons) were taken, this projection is done starting from just below the 2.6 MeV gamma's channel number and going up to the end of the alpha peaks (channels 3000 to 20000). This corresponds to a slice starting at 2500 and going up to 8000 photo electrons.

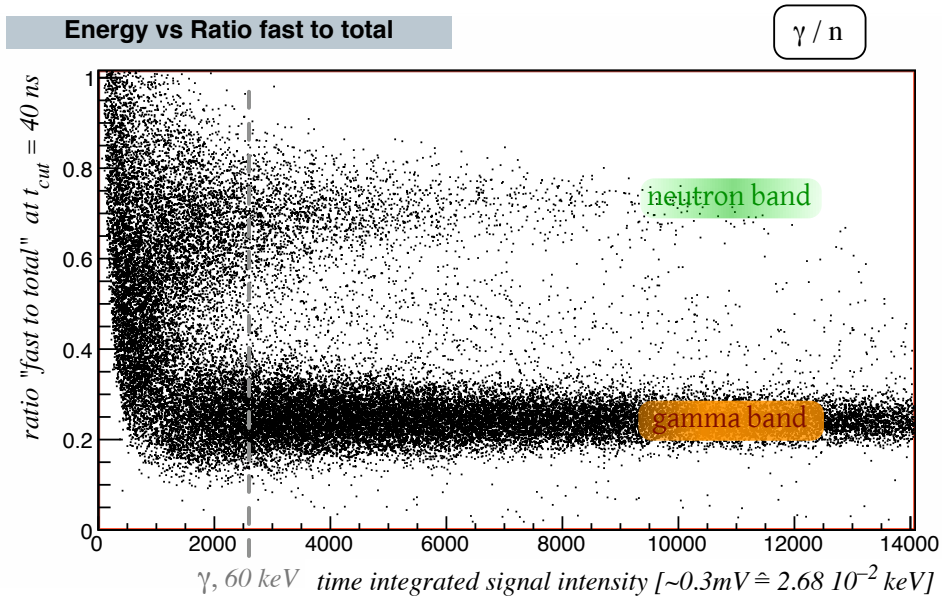

Figure 6.7: Scatterplot of the "fast to total" ratio against the energy of the pulse for a file under neutron and gamma radiation.

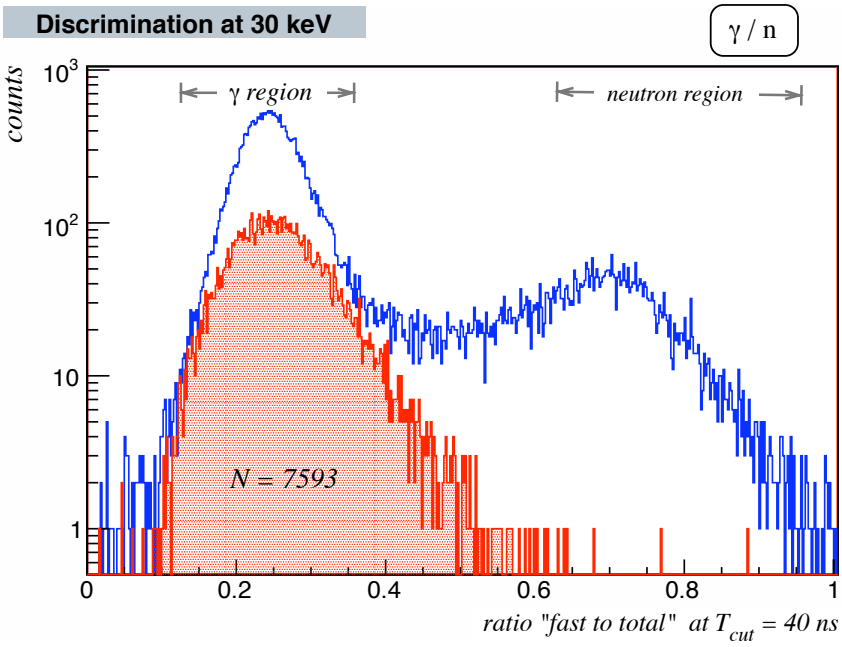

Figure 6.8: The discrimination power of gamma against neutron signals at an energy threshold of 30 keV. The blue histogram is data from a file taken under gamma and neutron radiation excitation. The red histogram shows data from a file with only gamma radiation excitation.

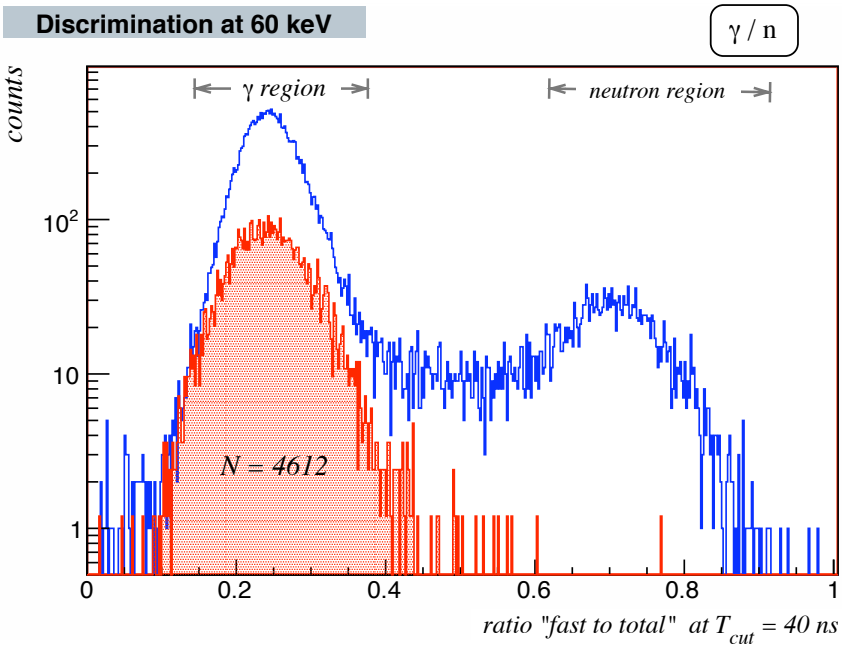

Figure 6.9: The same as figure 6.8 but with an energy threshold of 60 keV.

The following discrimination against γ events follows from this (the table quotes the fraction of events from the gamma file in the neutron band at two choices of D^{border}) :

	threshold energy	
D^{border}	30 keV	60 keV
0.6	$1.3{\cdot}10^{-3}$	$4.3{\cdot}10^{-4}$
0.7	$2.6{\cdot}10^{-4}$	$2.2{\cdot}10^{-4}$

These values are only upper limits, because the γ-like events above D^{border} are not necessarily caused by photons; they could actually be from background neutrons.

The acceptance for neutron events under the assumption of a Gaussian peak is 90$\pm$ 5% at $D^{border} = 0.6$ and 66 $\pm$5% at $D^{border} = 0.7$. These numbers were determined from a fit of the neutron peak in figure 6.9.

30 keV and 60 keV correspond to 37 and 74 photo electrons, respectively. With 35 photo electrons at $D^{border} = 0.6$ the discrimination, according to the simulation, is already better than 10^{-6}, but the number of events in the simulation was also larger by a factor of 10^3, so that just from a statistical point of view a better discrimination power was to be expected.

6.3.4 Gatti's filter

The ideal pulse shapes needed to generate the weights for Gatti's filter[5] were made from events cut out of the bands of the "fast to total" filter. These are nothing but the average pulse shapes shown in section v5.3. Since it is imperative that the right time slots of the signal and the weight are compared, the Gatti filter used the pulse's peak position as a reference. The peak is the only characteristic of the pulses whose position in time does not depend on the total energy.

A very simple algorithm was used to find the peak position. The program goes through each data point until one is higher than a given threshold, then it keeps going until the value in time bin $i + 10$ is smaller than the value in bin i. The bin $i + 5$ is then taken as the peak position.

The performance of Gatti's filter on the same data used in the previous subsection is shown in figure 6.10 for gamma-alpha discrimination.

The filter does not work well for the low energy gamma events in the neutron-gamma discrimination procedure, because it cannot find their peak positions reliably. It can still deal with the neutron events due to their much stronger fast component. The Gatti filter program was therefore rewritten to use the onset found by the previously used procedure described in section 5.2. The weights were re-calculated accordingly and the results are shown in figure 6.11 for an energy threshold of 30 and 60 keV. There were some data files with gamma events on which the Gatti filter did not work at all even after exhaustive attempts with varying thresholds and onset finding procedures.

[5]Refer to section 3.2.2 on page 23 for an explanation of the Gatti filter.

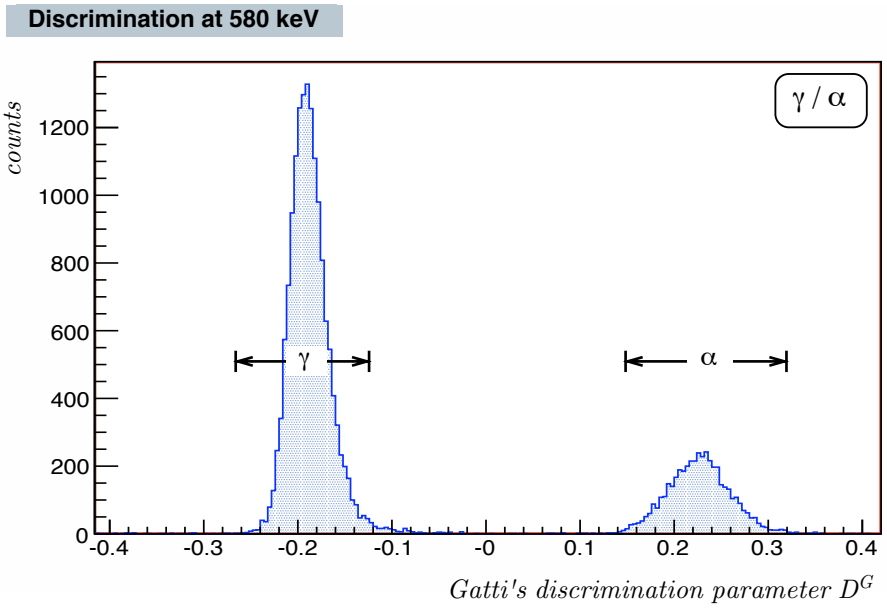

Figure 6.10: Gatti's filter applied to a file taken with Rn-222 in the system. Comparable to figure 6.6 on page 61.

The following discrimination against γ events is reached:

	threshold energy	
D^{border}	30 keV	60 keV
-0.12	$7.2{\cdot}10^{-3}$	$2.4{\cdot}10^{-4}$
-0.2	$4.1{\cdot}10^{-3}$	$1.7\cdot10^{-3}$
-0.25	$2.7{\cdot}10^{-3}$	$7.35{\cdot}10^{-4}$

A Gaussian fit fails on the neutron peak here, so that not even approximate acceptance levels can be quoted.

6.3.5 Discussion

In the simulations of chapter 3 it was assumed that all particle kinds occur at all energies with the same frequency. In reality, discrete transitions in unstable nuclei lead to discrete particle energies, so that the most abundant alpha particles for example have energies above 5.5 MeV. Neutrons on the other hand tend to have visible energies below 100 keV[6], so that discrimination between those two need not rely on pulse shape discrimination, but can be done by looking at the energy.

The case is different for photons/electrons/muons [7], which come from various decays

[6]The neutrons deposit only part of their energy in the detector, and part of that is quenched, so the energy seen by scintillation is much smaller than the original neutron energy.

[7]Photons, electrons and muons produce the similar pulse shapes.

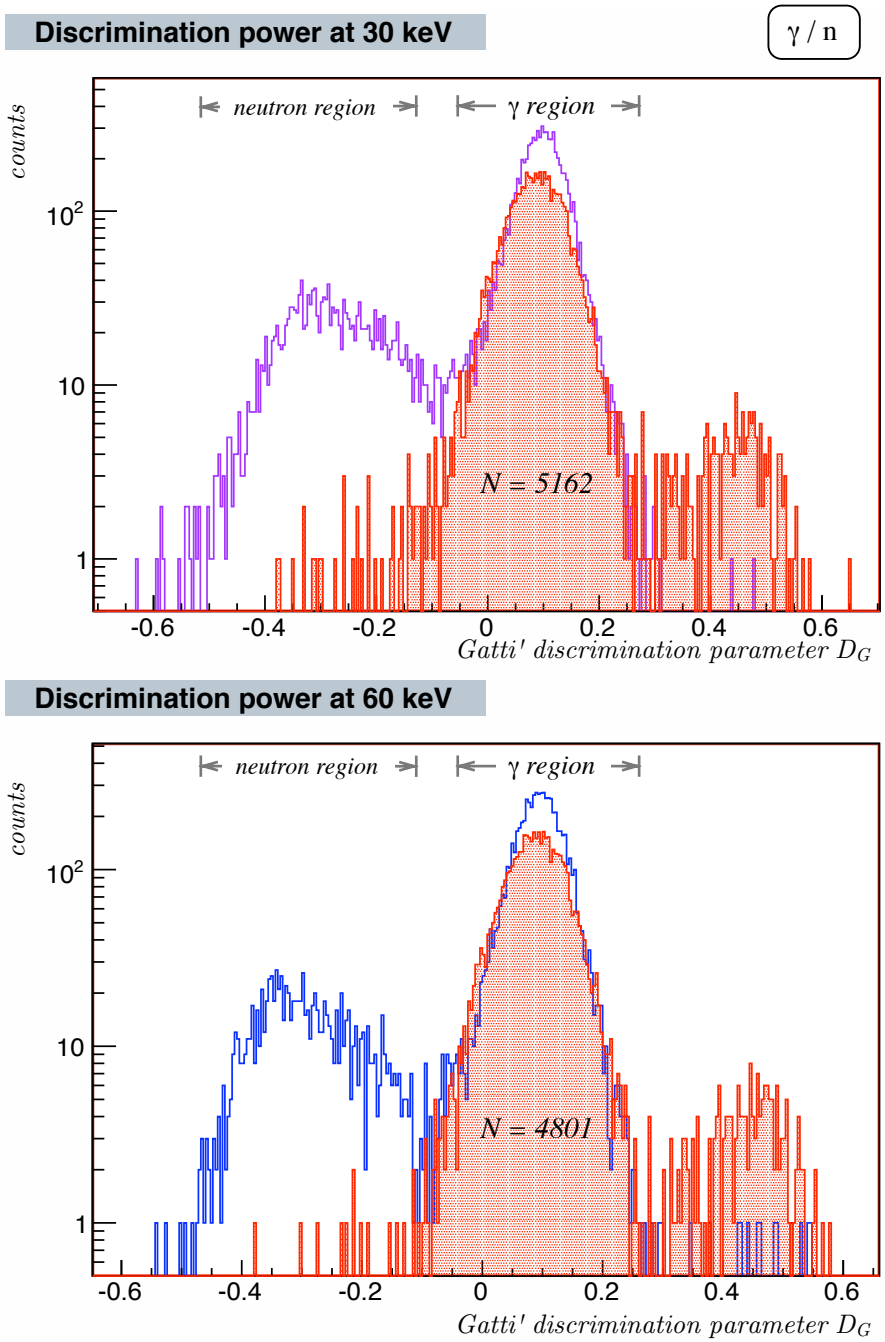

Figure 6.11: Discrimination between gamma and neutron events using Gatti's filter. The energy threshold is noted in the panels. Compare figures 6.8 and 6.9 on page 62.

and from cosmic radiation, and in addition tend to lose only part of their energy in the active volume. One can therefore expect photon-like events over the whole energy range, that is 0 to 8000 keV considered here.

The performance of the two filters will be discussed separately for gamma-alpha and gamma-neutron discrimination power, because the conditions for the discrimination procedure are quite different for those two cases.

gamma-alpha The peaks in the discrimination plots are rather far apart, so that it is not possible to quote how many events are in a wrong band. A statement about the quality of the discrimination can be made by introducing a distance parameter that quantifies how far the peaks are apart, taking into account the spread. For two gaussians with mean μ and spread σ this parameter is:

$$d = \frac{\mu_2 - \mu_1}{\sigma_1 + \sigma_2} \tag{6.23}$$

The bigger d is, the better is the discrimination power.

A gaussian fit to the peaks of figures 6.10 and 6.6 yields the following values:

	f/t		Gatti	
	α	γ	α	γ
μ	0.65	0.26	0.226	-0.189
σ	0.036	0.0027	0.032	0.019
d	6.2 $\pm$0.1		8.1$\pm$0.1	

The Gatti filter clearly places the bands further apart, thus allowing a better particle discrimination.

gamma-neutron The gamma and the neutron peaks in the discrimination plots overlap. Since data containing (nearly) exclusively gamma events is available, the discrimination parameter plots of the data with and without neutrons can be overlaid to see how far the gamma band stretches into the neutron region. This works well using the "fast to total" filter, but the plots produced using Gatti's filter deserve some discussion.

The Gatti discrimination parameter plots show some unexpected behaviour. The most obvious unexpected feature is that the bands are shifted to the left; the median of the peak centers should be at zero, instead it is located approximately at $D_G = -0.1$. This behaviour is an indication either for the assumed "ideal" pulse shapes not being the right ones, or for the discrimination algorithm not working right. Both factors probably play a role:

- The "ideal" pulse shapes are just the average pulse shapes gained by applying several cuts, among them a "fast to total" ratio cut, to the data and averaging over the pulse shapes of the remaining events. This means the crucial component of the Gatti filter, the ideal pulse shape, is gained by taking data chosen by a

different filter. This has to introduce a bias into the Gatti filter. If the events are taken from the central part of the neutron band, as it presents itself in the "fast to total" scatterplots, some of the events are from gammas, so the pulse shape is not a pure neutron shape. If events only from the upper part of the neutron band are taken, where the chances of finding a gamma event are slim, the ideal pulse shape is biased towards events with a stronger fast component than that of the typical neutron pulse.

- That the discrimination algorithm in principle works fine is clear from the gamma-alpha discrimination. It does however not work fine for gamma pulses of low energy, as seen by the need to modify the onset finding algorithm. The second crucial part of Gatti's algorithm is the comparison of intensity at a certain time. If intensities in the wrong time bins are compared, the discrimination suffers considerably. Finding the onset of low energy gamma pulses with an uncertainty perfectly acceptable to the "fast to total" filter can easily be done, finding it so that the Gatti filter performs well is very hard.

The second unexpected feature is the band that seems to rise to the right of the gamma band in the gamma data. There is no indication for another band in the "fast to total" scatterplot of the same data. The neutron/gamma data shows some events in that area, but not nearly as many. No conclusive explanation for that band could be found, though it probably has to do with the problems of finding the right onset. The tables that state the fraction of gamma events in the neutron area do not take into account the events in that unexplained band.

The number of events in the wrong band depends on the choice of band border, D^{border}. There is however no direct correspondence between the discrimination parameter values of the two filters, so that one cannot compare the performance of them directly. Looking at the results for values of D^{border} chosen to approximately correspond to each other and taking into account all uncertainties one has to conclude that both filters work equally well.

The Gatti filter might yet work better on the neutron data if the onset finding algorithm is improved and the ideal pulse shape for neutron events is gained with a lot better statistics and more shielding against background.

Chapter 7

Xenon doped liquid argon

7.1 Motivation

We know from literature that doping liquid argon with small amounts of xenon improves the light yield[45][37][59][24] and shortens the overall duration of the pulses [35]. The discussion of chapter 3 showed that the discrimination power crucially depends on the light yield and it might therefore be improved by the addition of xenon. A shorter pulse duration is also desirable since the dead time of the detector decreases together with it. For the GERDA experiment in particular, a higher light yield and more intensity in a short time interval means the background detection energy threshold for the veto system is lowered, a shorter time window can be used, or alternatively less PMTs are necessary to maintain the same background detection ability as in pure argon. The reduction of the number of PMTs is an advantage because the PMTs themselves contain many radioactive impurities.

The purpose of the following investigations was to study the effects of xenon doping on the achievable light yield, pulse shape and ultimately the achievable discrimination power. To the best of the author's knowledge, this was the first time such studies were done in a xenon doped liquid argon detector with the dimensions of LArGe@MPI-K (about 21 l active volume). All the measurements with argon-xenon mixtures reported about in literature were done with less than On measurement was reported using 1 l of liquid argon[33]. The others only used in the order of a few hundred ml. In all cases, argon and xenon were mixed in their gaseous states and then liquefied together, with the assumption that the concentration does not change during the process [45, 34, 37, 33, 61].

7.2 Theory and literature review

Xenon is a noble gas with atomic number 54. The configuration of its outer shell electrons is the same as that of argon, therefore it has the same kinds of excited atomic states and inter-atomic potentials and will also form excimers in a singlet and in a triplet state. The energy levels associated with those states in xenon are shown in table 7.1. For

Table 7.1: argon and xenon atom lowest excited states. [41][31]

state	energy [eV] argon	xenon
$^1S_0$	0.0	0.0
$^1P_1$	11.82	9.57
$^3P_0$	11.72	9.45
$^3P_1$	11.62	8.44
$^3P_2$	11.54	8.31

comparison, the argon energy levels from table 2.2 on page 7 are stated, too.

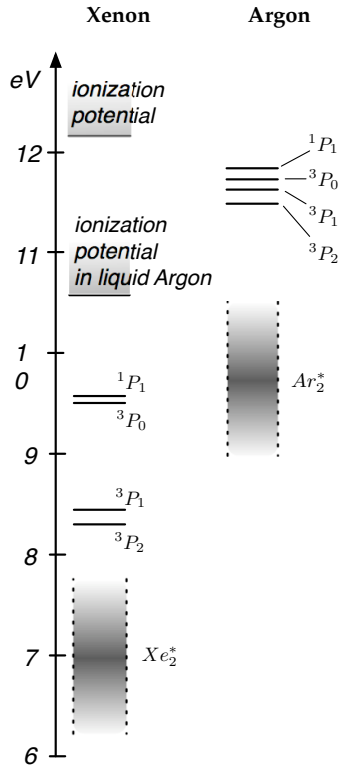

Figure 7.1: Lower atomic and molecular energy states of the argon/xenon system. (Reproduced from ref.[41] and adapted for the liquid using ref.[45] and [51])

In figure 7.1 the atomic and molecular energy levels of argon and xenon are shown. The ionization potential of xenon in liquid argon is smaller than it is normally[51], lying lower than the four lowest excited argon levels.

xenon also scintillates with the following properties:

Wavelength	175 nm
Singlet decay time	∼2 ns [47]
Triplet decay time	∼20 ns [47]

Figure 7.2 shows the spectra of argon gas with two concentrations of xenon. The peaks are labeled in accordance with figure 7.1. It shows that both dipole-allowed atomic xenon emissions appear at a low xenon concentration already, and that at higher xenon concentrations the Ar_2^* emission disappears in favour of the Xe_2^* molecular emission. The measurement was done in the gas phase, but the results qualitatively also apply to the liquid, where the Xe_2^* peak appears sooner[34].

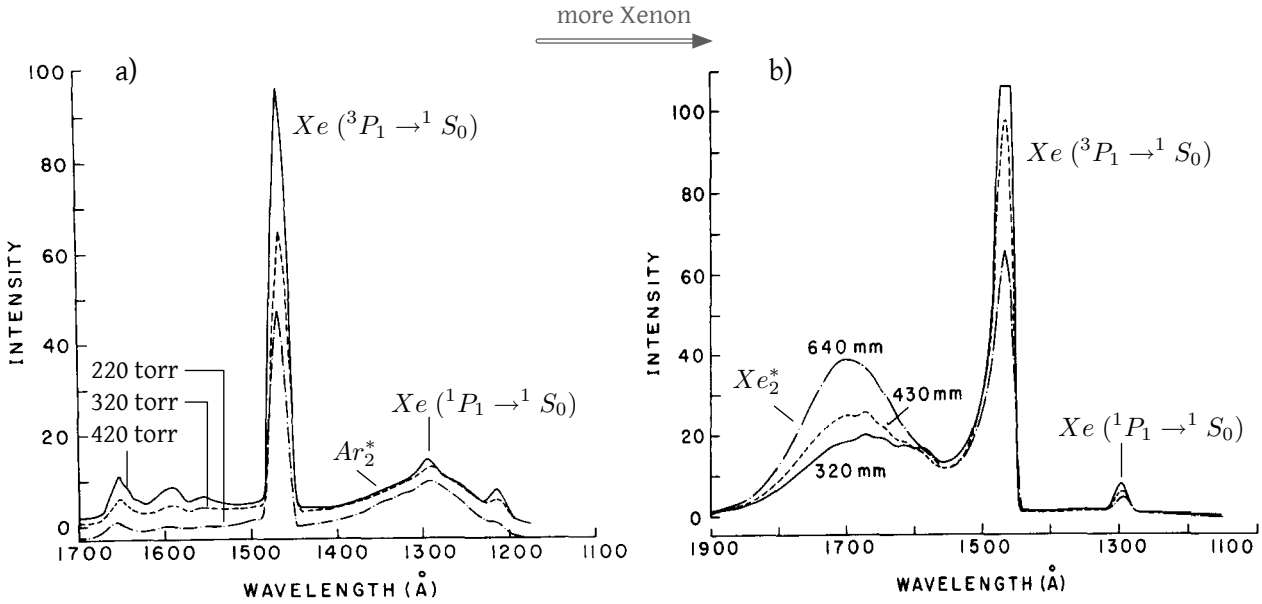

Figure 7.2: Spectra of xenon doped argon gas. Argon pressures are noted in the graphs. Xenon concentrations: a) $7.5 \cdot 10^{13} atoms/cm^3$ b) $7.5 \cdot 10^{15} atoms/cm^3$. Taken from ref. [41].

The presence of atomic and molecular xenon emission is a consequence of energy transfer from argon to xenon atoms. Looking again at figure 7.1, the excited atomic argon states transferring their energy will lead to ionization of xenon atoms, while the argon excimers will transfer their energy to the xenon atoms, exciting them into either the $^1P_1$ or the $^3P_0$ states. The remaining two lowest excited xenon states can be populated through collisions from the upper excited states, or from the recombination of the ionized xenon with its electron. Kubota et al.[45]([37]) showed that at xenon concentrations $> 2\%$ all of the argon excimers transfer their energy to xenon atoms many of which then become ionized. The shortening of the pulse duration is then due to energy transfer from the long-lived argon triplet excimers to xenon, which has a much shorter decay time.

A definite reaction scheme for the energy transfer from argon to xenon has not been agreed upon. There is some controversy as to whether mixed molecules, i.e. $ArXe^*$, exist and play a role in the energy transfer[36][61][34], and in how far the energy transfer is mediated through collisions or through dipole-dipole interaction between argon molecule and impurity atom. Possible energy transfer pathways will be discussed in section 7.4.2 in the context of developing a mathematical description for the new pulse shapes.

A conclusive explanation for the light yield gain has not been given yet either. While the addition of xenon does seem to lower the W-value (see equation 2.10 on page 12) to for example 21.3 ±0.5 eV at 0.7 % xenon[24], this decrease is not enough to explain an increase of up to twice the scintillation yield as reported for example by Kubota et al[59]. They suggested that the increased light yield is due to a higher quantum efficiency of the wavelength shifter at the emission wavelength of xenon excimers. Since some groups did not notice any considerable increase in the light yield[33], Kubota's explanation seems likely.

7.3 Implementation and Operation

7.3.1 Xenon doping

xenon was inserted into the system in its gaseous state through pipe E especially added for that purpose (compare figure 7.3). Since xenon freezes at the temperature of liquid argon, it had to be diluted with enough argon gas to prevent freezing inside the pipe. This was achieved by connecting an argon gas bottle to the xenon pipe and opening valve 7 first, then slowly opening valve 8 so that the flow from the xenon bottle was much smaller than that from the argon bottle.

The concentration of xenon actually dissolved in the argon could not be calculated exactly from the amount of xenon lost from the bottle and the amount of argon in the system, because some xenon would freeze to the walls of the tube, and some of it would bubble out with the argon gas and escaped through tube A. The exact amount of argon in the active volume is also not known[1], and neither is the extent to which xenon will diffuse into the outer volume. Samples of the argon-xenon mixture were therefore taken for analysis in a mass spectrometer by the following procedure:

One side of a T-piece pipe was connected to the pipe after valve 5, one side of it was open to the atmosphere and one was connected to an air tight, evacuated glass sample container[2] that could be opened or sealed with valve 7. The whole tank was pressurised with argon gas through pipe D with only valve 4 open. Valves 3 and 5 were then opened and liquid argon escaped through pipe C, evaporating before reaching the exit. As soon as argon escaped in the liquid phase, valve 7 was opened and a small amount of liquid argon entered the evacuated sample container. The argon evaporated on contact with the glass and valve 7 was closed again.

[1] The fill level can not be determined exactly, and argon evaporates constantly.

[2] All but one sample were kept in glass containers. The remaining sample was filled into a metal sealed piece of pipe.

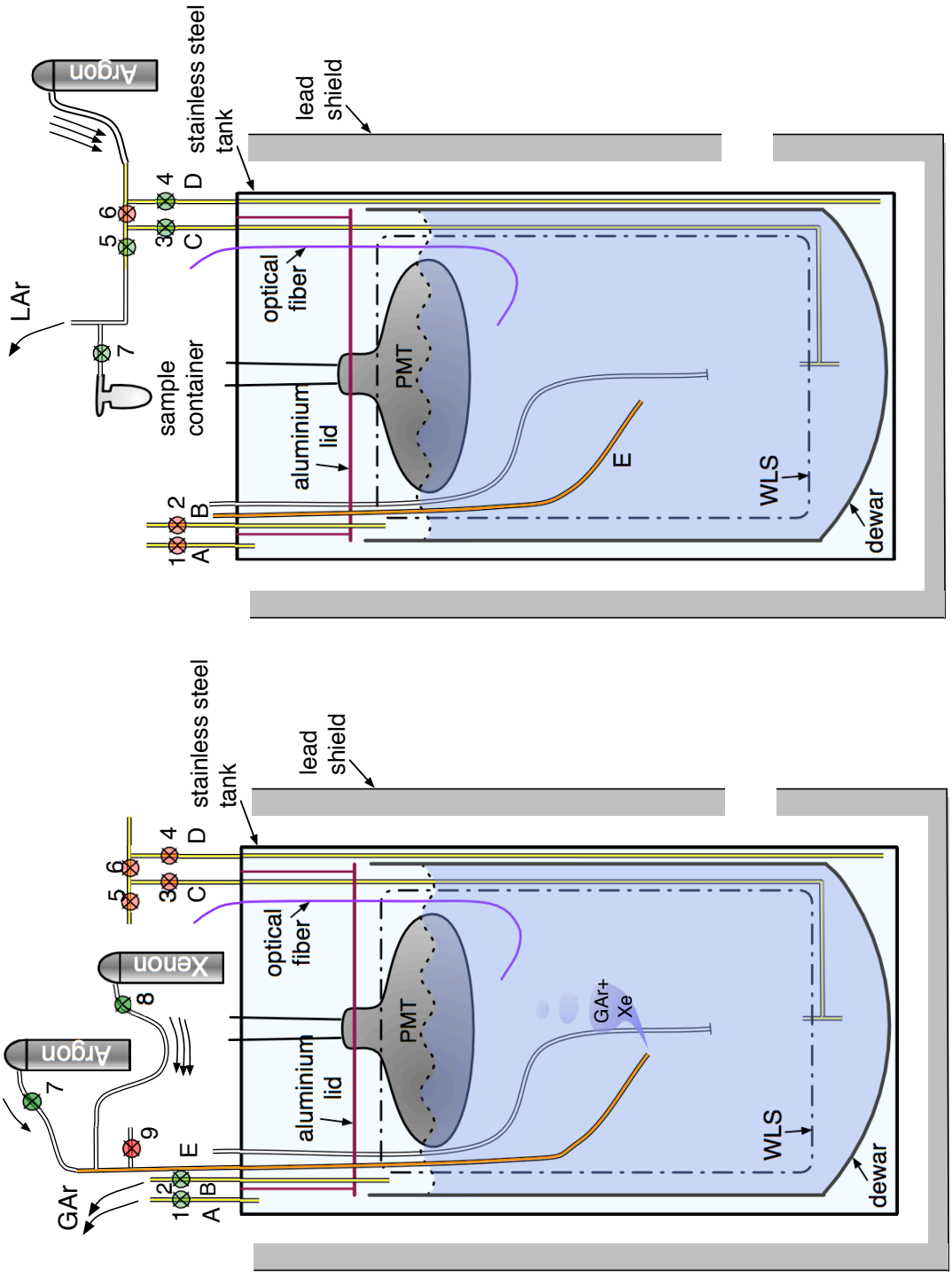

Figure 7.3: System configurations for filling xenon and for taking a sample of the argon-xenon mixture. Valves drawn in red are closed, valves drawn in green are open.

A possible intake of ambient air after opening valve 7 was not a serious concern, since neither argon nor xenon are present there in such amounts[3] as to seriously alter the concentration. Possible problems with this method of sample taking will be discussed at the end of the next section.

In the first run, 1 l, as measured by the pressure loss in the gas bottle, of gaseous xenon grade 4.0 was flushed into the system. After that, 3 l and then 6 l xenon gas were added. If all the gas was dissolved in the liquid argon of the active volume (about 13.5 l), the following concentrations would be expected:

Pressure loss in xenon bottle [bar]	Expected xenon concentration [ppm]	Concentration label
1	88	c1
4	352	c2
10	500-700	c3

While filling 6 l of xenon into the system, pipe E froze shut with xenon, so that it is unclear how much xenon actually entered the active volume. Pipe E could not be used anymore to fill xenon or to extract samples. Therefore, it was decided to remove half of the argon-xenon through pipe C, then refill pure argon in the usual way, that way reducing the xenon concentration.

The procedure of removing liquid from the detector was similar to that for taking a sample from the liquid, except that the end of the replacement pipe for pipe C was connected to a waste Dewar and pressure was applied to the system until half of the argon-xenon had been pressed out. Every time this procedure was performed, the xenon concentration should have been halved if the xenon was distributed homogeneously. The uncertainties however are just as big as in the previous case of filling xenon in, because the temperature sensors allow only a very crude estimate of the argon filling level. All samples from c3 on were also taken through that replacement pipe. The expected xenon concentrations (assuming homogeneous distribution) then were the following:

Emptying cycle	Expected xenon concentration [ppm]	Concentration label
1	250-350	c4
2	125 - 175	c5
3	60 - 90	c6

There is no reason to believe that the xenon was distributed homogeneously in a detector of this size. Since all former experiments seem to have been done in very small detectors, there is no experience with such large volumes. Nevertheless, the assumption of homogeneous distribution was made as no indication to this not being the case could be found in literature.

[3]There is less than 1% argon and less than 9 ppb xenon in the atmosphere

7.3.2 Xenon concentration measurement

Mass spectrometry

Gases that flow through the mass spectrometer are ionized by an electron beam and then pass a quadrupole filter that filters out all ions except such with a given ratio of charge to mass whose current is then measured. The value of charge to mass that gets through to the detector can be chosen by adjusting the parameters of the quadrupole filter.

To correlate the measured currents at a given mass with the concentration of the gas with that mass, the system has to be calibrated. This is done the following way: One prepares a gas mixture that contains known amounts of all the gasses for which one seeks calibration factors and measures the currents at their masses. Say there are N gasses in the calibration mixture with known masses $\{m_1, ..., m_N\}$[4], and partial pressures $\{p_1, ..., p_N\}$, and the measured currents of the sample are $\{I_1, ..., I_N\}$, while those of the background at the same masses are $\{I_1^{bg}, ...I_N^{bg}\}$. The partial pressure of the gas with mass m_i is related to the total pressure P of the mixture by

$$c_i \cdot P = p_i \tag{7.1}$$

where c_i is the concentration of component i expressed as fraction of the total gas volume. The sensitivity of the system to the i-th gas in the mixture expressed in A/mbar is

$$f_i = \frac{I_i - I_i^{bg}}{p_i} = \frac{I_i - I_i^{bg}}{c_i \cdot P}. \tag{7.2}$$

The factor f_i stands for how big a current is measured per unit partial pressure of the i-th component.

The sample measurement, done at absolute pressure P^{sample}, will yield another set of currents $I_1^{sample}, ..., I_N^{sample}$, and the concentration of component i is then:

$$c_i^{sample} = \frac{I_i^{sample} - I_i^{bg}}{f_i \cdot P^{sample}} \tag{7.3}$$

Mass spectrometer setup and operation

The concentration of xenon in argon was measured with a Prisma QMS 200 M2 mass spectrometer. A schematic view of the setup is shown in figure 7.4. The spectrometer is operated under dynamic conditions, with the sample gas flowing through the variable leak valve (VLV) into the mass spectrometer vacuum chamber (MSVC) which is pumped constantly by a turbo pump.

[4]If any of the gases one is measuring has several isotopes, they all have to be taken into account by either measuring the current at each corresponding mass and adding them up, or by measuring only one isotope and then calculating how much of that gas is actually present using known ratios between the isotopes.

Before commencing the measurements the whole system was baked at $\sim 150°C$ and pumped for three days in order to reduce the background. The final pressure in the MSVC was at the level of $2 \cdot 10^{-9}$ mbar as seen from pressure gauge P2[5], and the volume enclosed by valves V1, V2, V4 and the VLV was below 10^{-8} mbar seen from gauge P3.

The setup allowed for measuring the remaining background in two different ways: with the VLV closed at the pressure of $2 \cdot 10^{-9}$ mbar in the MSVC, and with the VLV open under flow of a pure test gas. The connection line from the test gas bottle to the setup was flushed through the bubbler for at least an hour after switching gas bottles and before the start of a measurement.

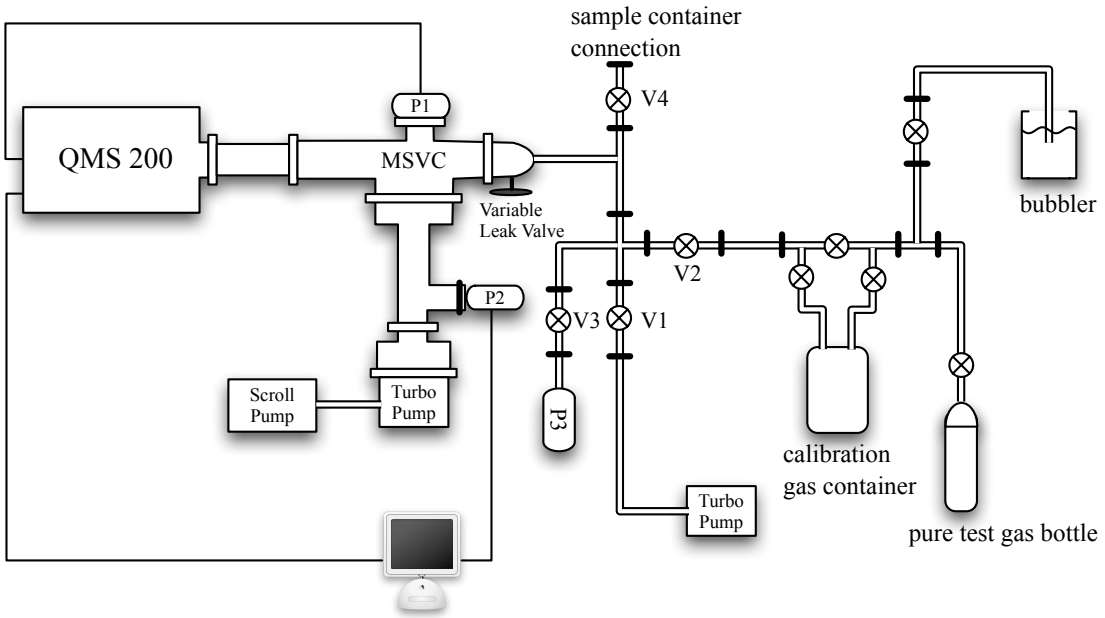

Figure 7.4: The setup surrounding the mass spectrometer. The sample container with the argon-xenon mixture is connected above valve V4. P1 to P3 are pressure gauges.

The spectrometer was calibrated at a pressure of $1.0 \cdot 10^{-6}$mbar in the MSVC using a calibration gas of the following composition:

[5]There are two pressure gauges, P1 and P2, connected the the same volume. This is not strictly necessary, but convenient for observing the pressure at all times using P2, because P1 is linked to the mass spectrometer and cannot be read out directly.

Component	Concentration [%]
Ar	94.43 ± 0.03
Xe	0.94 ± 0.03
Kr	1.02 ± 0.03
O_2	0.91 ± 0.03
N_2	1.45 ± 0.03
CO_2	1.24 ± 0.03

The gas was kept in a metal sealed 2 l container which had been baked out at 150°C and pumped for several days before the calibration gas was filled into it. The uncertainties in the calibration gas composition came from the uncertainty in the pressure reading.

Before each sample measurement, the background under argon 6.0 flow was measured and the spectrometer calibration with the calibration gas repeated. The sample containers were connected above valve V4 and the concentration measurement was done at a pressure of $1.0 \cdot 10^{-6}$ mbar in the MSVC

Concentration measurement results

The following masses (in atomic units) were scanned for each measurement, following the composition of the calibration gas and taking into account water as the most abundant impurity: 18 (H_2O), 28 (N_2), 32 (O_2), 36 (Ar)[6], 44 (CO_2), 84 (Kr), 129 (Xe). Other isotopes for each element need not be considered, because we were not interested in absolute amounts, but in the relative amount of xenon in the argon. For this purpose it is only necessary to assume that the fraction each isotope constitutes of the total amount of one element is constant in time.

The background was measured under argon 6.0 flow, because during initial sample measurements high concentrations of impurities were found, which could not have been present in the scintillation detector without completely quenching the scintillation light. This raised the question whether so many impurities could still be present in the spectrometer setup. Table 7.2 lists the currents measured under vacuum (VLV closed) and under argon 6.0 flow. The considerably higher signals of all impurities under argon flow – nearly one order of magnitude for xenon – can be seen (also compare figure 7.5). They could not be reduced by further baking, filament degassing or spectrometer parameter optimization. Changing the operating pressure from 10^{-6} mbar to 10^{-7} mbar resulted in less background, but an equally smaller signal, so that the sensitivity in the end was unchanged.

The test was repeated with pure Helium 6.0 gas and yielded similarly high background currents. Since the sample measurements would be done at the same total pressure and under dynamic conditions, the background values under pure argon flow were assumed as the actual background for all calculations.

[6]This isotope with a very small fraction of the total amount of argon was chosen so that the argon and the xenon current could be measured with the same instrument.

Table 7.2: Background values (currents) for different masses (elements) measured under vacuum and clean Ar (6.0) atmosphere at 1×10^{-6} mbar.

Mass [element]	Vacuum [A]	Ar [A]
18 [H_2O]	6.51×10^{-10}	1.03×10^{-9}
28 [N_2]	8.84×10^{-11}	4.64×10^{-9}
32 [O_2]	8.41×10^{-13}	9.00×10^{-13}
36 [Ar]	8.34×10^{-13}	-
44 [CO_2]	1.91×10^{-11}	2.28×10^{-10}
84 [Kr]	2.03×10^{-13}	5.34×10^{-12}
129 [Xe]	1.80×10^{-13}	9.61×10^{-13}

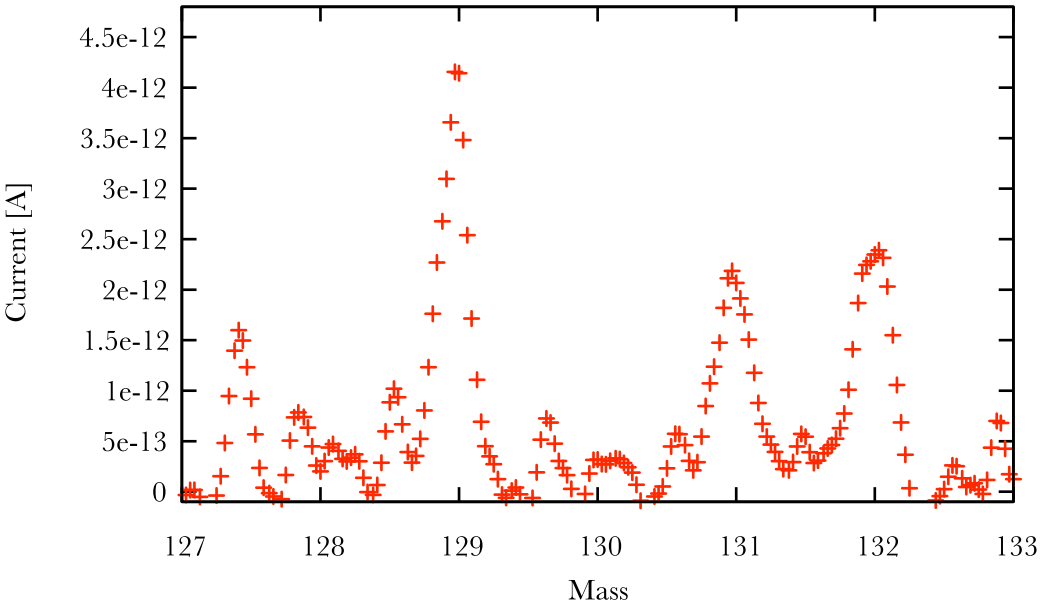

Figure 7.5: xenon peaks in the mass spectrum under flow of argon 6.0.

Typical currents of the calibration gas mixture and the sensitivities following from them are shown in table 7.3

Mass [element]	I [A]	f [A/mbar]
28 [N_2]	2.03×10^{-8}	1.07
32 [O_2]	3.19×10^{-9}	0.35
36 [Ar]	2.21×10^{-9}	2.32×10^{-3}
44 [CO_2]	6.85×10^{-9}	0.53
84 [Kr]	1.33×10^{-9}	0.13
129 [Xe]	1.45×10^{-10}	1.52×10^{-2}

Table 7.3: Typical currents measured for the calibration gas mixture and the sensitivities that follow from them.

The final results for the concentrations are summarized in table 7.4. The errors are only those pertaining to the measurement in the mass spectrometer, including uncertainties in the calibration gas partial pressures, the statistical fluctuations of the measured currents on the signal and on the background and the uncertainties in the pressure reading at P1 and P2.

The pressure gauges P1 and P2 eventually turned out to have been responsible for the high background. They are hot cathode ionization gauges and were recommended by the company for use with the mass spectrometer, P1 was delivered with the system, yet turning them off resulted in an immediate reduction of the background nearly to vacuum level. This however was not found until all samples had been measured.

sample	concentration [ppm]
c1	< 90
c2	297 ± 160
c3	3341 ± 350
c4	1411 ± 130
c5	871 ± 110
c6	357 ± 160

Table 7.4: The concentrations measured for samples c1 through c6.

The uncertainties are so high because the signal was only a few times higher than the background, so that fluctuations in the background lead to a large uncertainty in the signal. The high background and resulting high uncertainty in the measured concentrations are immaterial in so far as the overall uncertainties on the concentration are actually much larger. They can be divided by error source:

argon evaporating from the dewar The xenon concentration during the time when signals were recorded might have been lower than at the time when the sample was taken, because some argon had evaporated.

Sample taking The samples c1 and c2 were taken from the same tube that was used to insert xenon. Xenon that might have been frozen on the tube and thus never entered the liquid could have been flushed out and into the sample container, making for a higher xenon concentration than that actually present during the measurement.

The samples c3, c4, c5 and c6 were taken from a different tube with an opening split between the active volume and the area beyond the reflector foil. A possible concentration gradient between those two areas of the detector would mean that the samples taken from different tubes are not comparable.

The xenon concentration could also have been altered during the evaporation process in the sample container, since evaporation started already in the tube leading to the container and argon evaporates sooner than xenon.

Storage The glass sample containers had to be stored for several weeks before the mass spectrometer was ready to be used. Any leaks in the vacuum seal would have allowed more argon than xenon to escape, changing the concentration in favour of the xenon.

Concentration measurement The unsuitable pressure gauge caused a very high xenon background and made it impossible to measure with a good accuracy.

7.4 Pulse shapes in xenon doped liquid argon

7.4.1 Measured pulse shapes

The deformation of the pulse shape at increasing concentrations of xenon can be seen well in figure 7.6 for alpha and for gamma pulse shapes. In both cases a second peak emerges whose position depends on the xenon concentration. The duration of the pulses is considerably shortened as shown in figure 7.7 where the pulse shape PDFs as well as the corresponding CDFs are shown for pulses in pure argon and in argon with two different concentrations of xenon. The transition to xenon doped argon seems to affect the different particle's pulse shapes in different ways. Especially the neutron pulse shape behaves in a peculiar way, turning up much closer to that of gammas once there is xenon in the system and displaying two instead of one intersections with the gamma pulse shape. At xenon concentration c2 the alpha and gamma pulse shapes are nearly identical[7].

The gamma pulse shapes for all xenon concentrations are shown in figure 7.8. The two frames show the same pulses once with double and once with single-logarithmic axes to emphasize the crossing times between the pure argon and the xenon doped pulse shapes and the positions of the new peaks respectively.

[7]No data for neutrons could be taken at that concentration, because the source was not available.

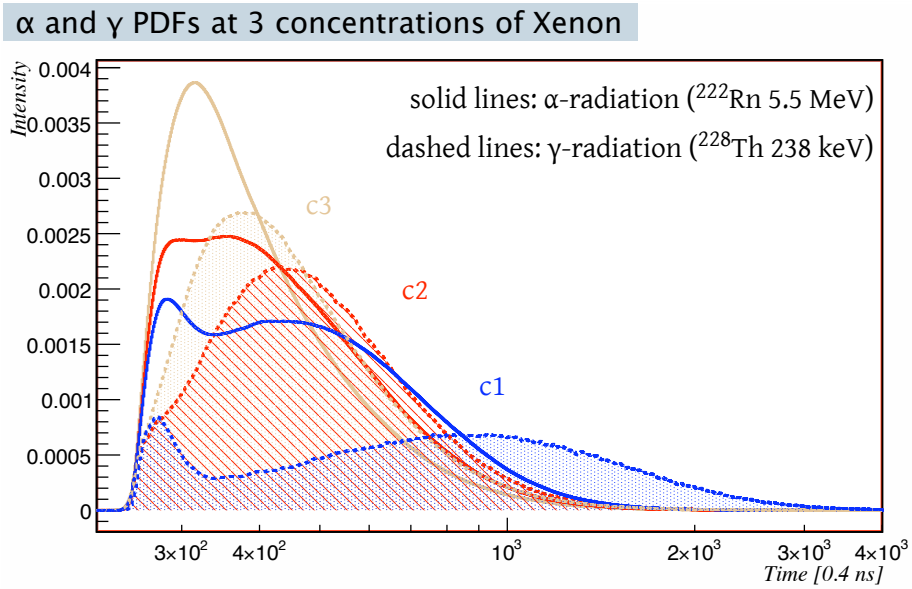

Figure 7.6: Alpha and gamma pulse shapes at 3 concentrations of xenon.

7.4.2 A new PDF

The pulse shape PDF in the argon-xenon system before any detector effects is a lot more complicated than it is in the case of pure argon. In order to get an idea how to go about constructing this PDF, the possible reactions that take place in the scintillator medium will now be considered. For starting points there are the measured pulse shapes, as well as the following facts which were presented in section 7.2 on page 68 already:

1. Atomic xenon emissions are seen in the spectrum.[41]
2. Molecular xenon emission gets stronger the higher the xenon concentration becomes.[41]
3. Molecular argon emission disappears with rising xenon concentration in favour of the molecular xenon emission.[41]
4. Increased ionization yield, consistent with the idea that excited argon atoms transfer energy directly to xenon atoms, thus ionizing them.[45]
5. The xenon's triplet state decay time is with about 20 ns[47] much shorter than that of argon. Its singlet state decay time is about 2 ns.

argon atoms must be the main excited species, because they are present in much bigger number than xenon atoms. The excited argon atoms then transfer energy to xenon atoms, leading to the respective peaks in the spectrum. The energy transfer can be mediated through collisions or through direct dipole-dipole interaction between the atoms[33]. The pathways by which this can happen are sketched in figure 7.9.

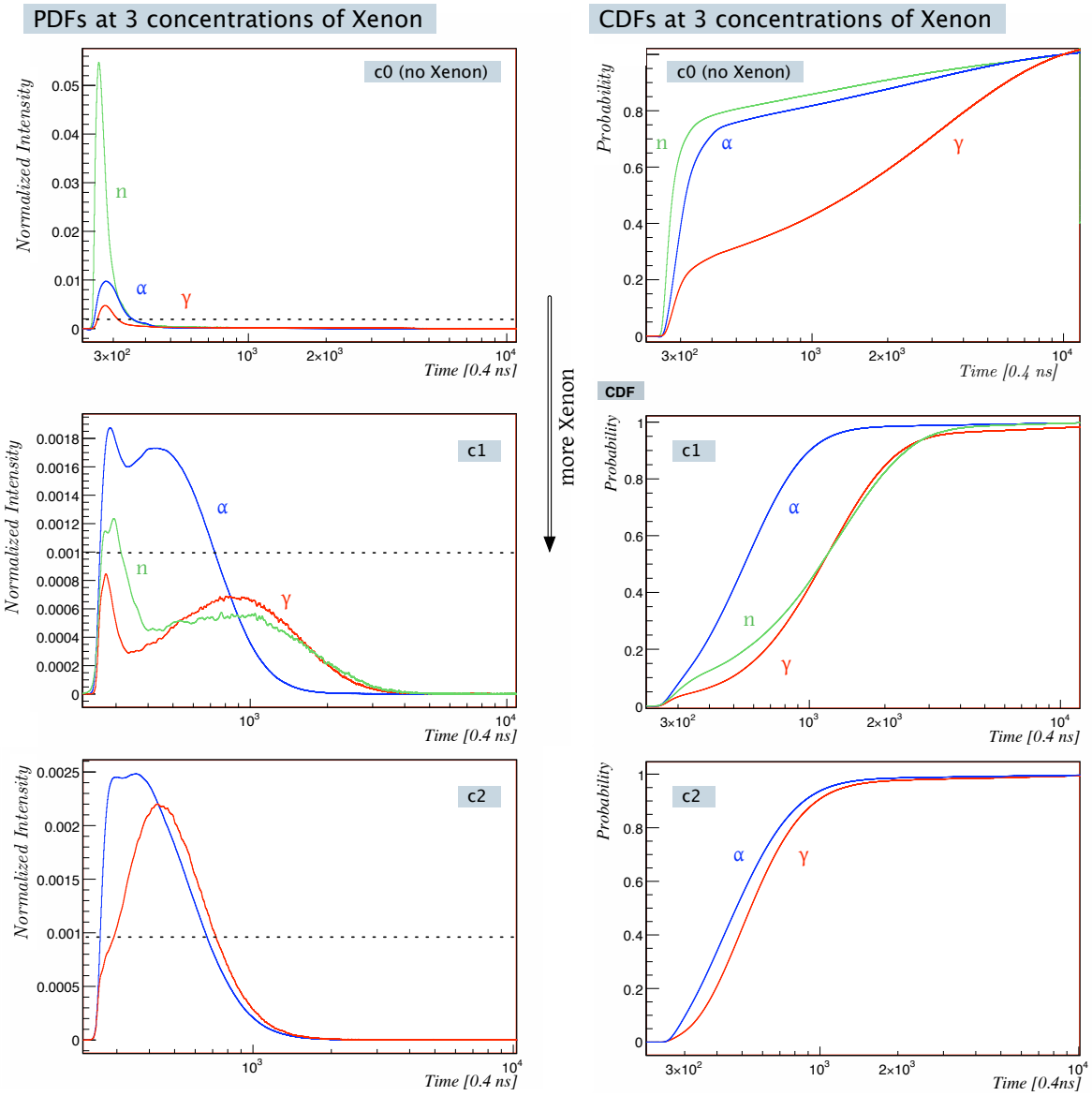

Figure 7.7: The evolution of the pulse shape from no xenon to the xenon concentration c2. Left column: PDF (mind that the x-axis scale is not the same on each plot). Right column: CDF. Notice how the neutron pulse shape changes relative to the alpha and gamma pulse shapes.

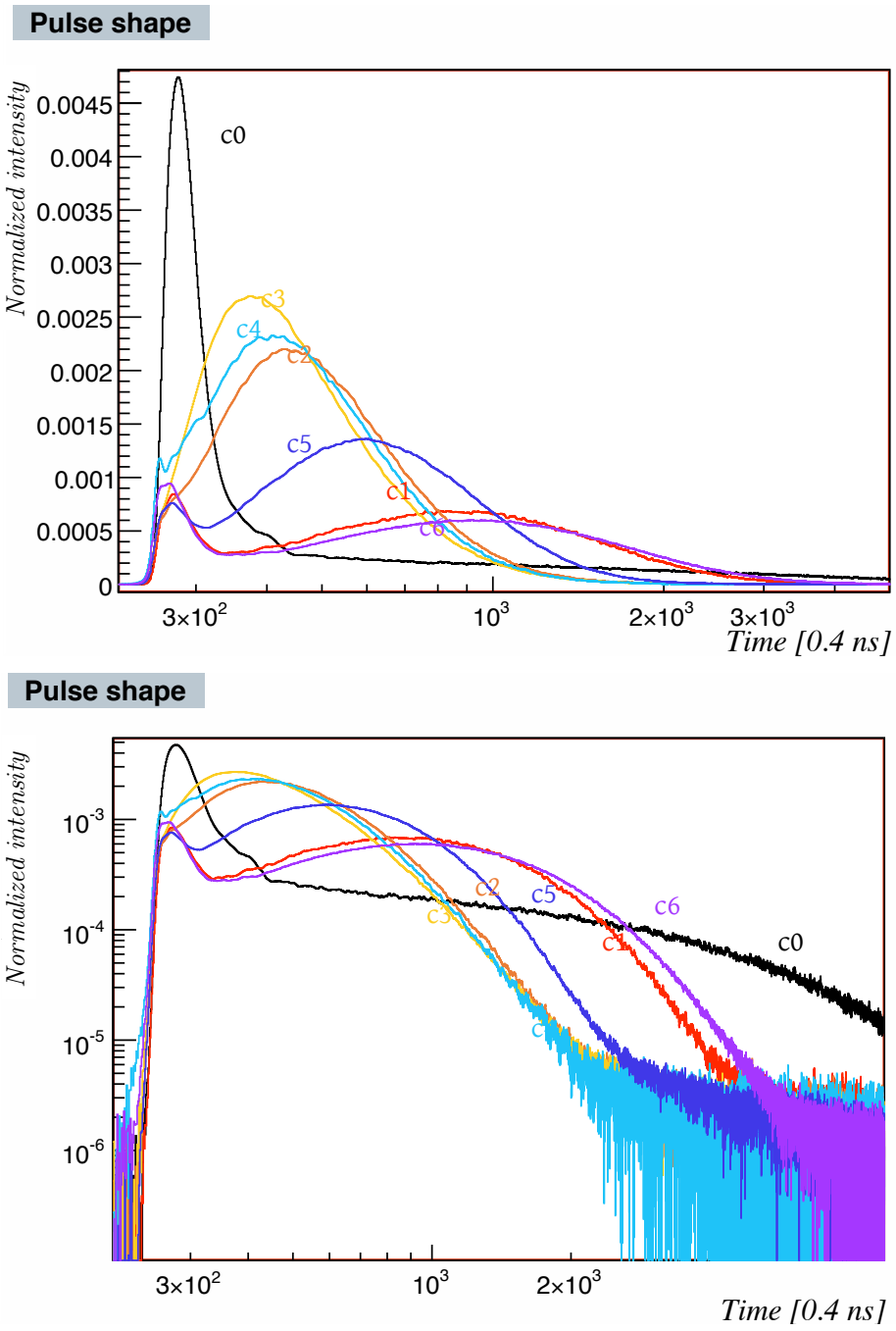

Figure 7.8: Gamma PDFs for all concentrations of xenon. Top: single-logarithmic scale, showing the change in position of the second large peak. Bottom: double-logarithmic scale, showing the order in which the xenon and argon pulse shapes cross the pure argon pulse shape.

From the excited argon atoms[8], a line goes directly to ionized xenon through dipole-dipole interaction, consistent with point 4 of the above list. Collisions are an unlikely energy transfer channel here, because they happen on a much longer time scale than the formation of argon excimers does. All four lower excited atomic xenon states can be populated after recombination of the xenon ion and its electron.

[8]For simplicity, the path over ionization, recombination and cooling to excitation is summarized into just one step. Refer to section 2.2 on page 7 for the pure argon scintillation mechanism.

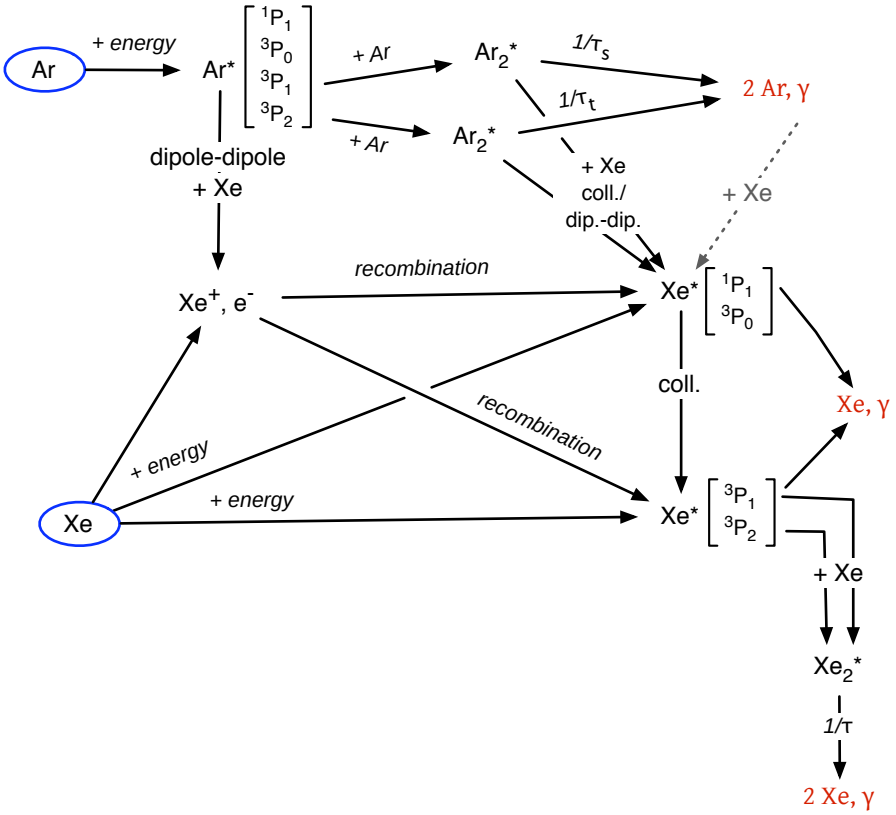

Figure 7.9: Simplified scheme of the possible energy transfer paths in the argon-xenon system. argon is excited into either of the four lower exciton states. Two of these can form excimers, all of them can transfer their energy to a xenon atom which is ionized as a result. The argon excimers can decay under photon emission, or they can transfer their energy to a xenon atom, forming one of the two resonant exciton states. The other two lower xenon exciton states have a much smaller energy and are no longer in resonance with the argon excimers, so that their direct formation is unlikely. They can however be formed from the other xenon exciton states by collision. Two of the xenon excimers can decay radiatively. As long as the xenon concentration is low, there is only a negligible chance for that light to be resonance absorbed by another xenon atom. Two of them can also form excimers which subsequently decay radiatively. The xenon that was ionized can recombine into either of the four lower excimer states, and xenon that is excited directly, i.e. by the primary radiation, can also form all four lower excimer states. The possible formation of mixed excimers $ArXe^*$ is not taken into account.

Not all energy goes that way, as indicated by point 3 in the above list. Some argon excimer emission can still be seen up to a certain xenon concentration, so excimers are still produced and part of them decay normally, while others transfer their energy to xenon atoms which become excited into one of the states whose energy overlaps with that of the excimers (compare figure 7.1). Both collisional and dipole-dipole energy transfer is possible here, but the dipole-dipole interaction channel is more likely for the singlet argon excimer, which decays too quickly to make collisions an effective energy

transfer method; the long-lived triplet excimer has both channels at its disposal. The energy transfer can as well occur after the argon excimer decay, if a xenon atom absorbs the released scintillation photon. In all of these cases, only the two upper excited xenon states can be excited. One of them can just decay under photon emission, both can loose some energy in collisions and end up in one of the remaining two states. One of those states can again just decay, and both of them can form a xenon excimer with another xenon atom. This excimer then decays under emission of a photon.

Despite the small number density of xenon atoms compared to that of argon atoms at the concentrations considered here (100 to 1000 ppm), the direct excitation of xenon might not be negligible in the case of excitation with photons, because xenon has an up to 10 times higher interaction cross section with them than argon does (in the energy range of 20 to 200 keV)[31]. Assuming cross sections σ_{Ar} and σ_{Xe} in barn/atom and a xenon concentration of c_{Xe} one finds that

$$\frac{N_{Ar^*}}{N_{Xe^*}} = \frac{N_{Ar} \cdot \sigma_{Ar}}{N_{Xe} \cdot \sigma_{Xe}} = \frac{1}{c_{xe}} \cdot \frac{\sigma_{Ar}}{\sigma_{Xe}}. \tag{7.4}$$

A rough estimation yields that at a xenon concentration of 100 ppm xenon is excited directly in about 0.5% of the cases. In addition, the energy flow from excited argon atom over ionized xenon to excited xenon atom happens so quickly that the excited xenon atoms can be treated as if they were produced directly.

The unification of the pulse shapes can already be understood from the above scheme: Both the singlet and the triplet argon excimer excite the same xenon states, so that information about the ratio R, which has been the lever for discrimination, is lost the more of the energy is turned into scintillation through the xenon and the faster the energy transfer takes place. When the concentration of xenon is so high that the energy transfer to the xenon is faster than the lifetime of the argon singlet state, the pulse shapes are probably indistinguishable.

With the introduction of xenon another detector effect arises: the wavelength shifter very likely has a different quantum efficiency at the wavelength of the xenon scintillation. There is no information about the wavelength shifter's quantum efficiency at the wavelengths involved here, so the contributions of scintillation photons from the different steps of figure 7.9 should be weighted with arbitrary factors.

7.4.3 Fitting the new PDF

The challenge of developing a photon emission PDF in the argon-xenon system lies in finding all the energy transfer paths that may be neglected. Taking into account all possible paths would lead to an unwieldy equation and to a large number of free parameters. The negligible paths, however, depend on the xenon concentration.

A very crude ansatz that might be approximately right for most of the concentrations

used here is the following:

$$\begin{aligned}
(Ar_2^*)_s &\xrightarrow{1/\tau_s} 2Ar + \gamma \\
&\xrightarrow{a} Xe^*(^1P_1) \\
(Ar_2^*)_t &\xrightarrow{1/\tau_t} 2Ar + \gamma \\
&\xrightarrow{a} Xe^*(^1P_1) \\
Xe^*(^1P_1) &\xrightarrow{b} Xe + \gamma \\
&\xrightarrow{c} Xe^*(^3P_1) \\
Xe^*(^3P_1) &\xrightarrow{d} Xe + \gamma \\
&\xrightarrow{e} Xe_2^* \xrightarrow{1/\tau_{Xe}} 2Xe + \gamma
\end{aligned}$$

With initial concentrations

$$\begin{aligned}
[(Ar_2^*)_s](t=0) &= A \\
[(Ar_2^*)_t](t=0) &= B \\
[Xe^*(^1P_1)](t=0) &= C \\
[Xe^*(^3P_1)](t=0) &= D \\
[Xe_2^*](t=0) &= 0
\end{aligned}$$

and restrictions

$$\begin{aligned}
\frac{A}{B} &= R \\
A + B + C + D &= 1.
\end{aligned}$$

The different kinds of possible energy transfer mechanisms are not distinguished, the four excited xenon states are grouped in pairs of two just like in figure 7.9 and the singlet state decay time of the xenon excimer is neglected. The corresponding rate equations

are

$$\begin{aligned}
\frac{\partial}{\partial t}[(Ar_2^*)_s] &= -(\frac{1}{\tau_s} + a)[(Ar_2^*)_s] \\
\frac{\partial}{\partial t}[(Ar_2^*)_t] &= -(\frac{1}{\tau_t} + a)[(Ar_2^*)_s] \\
\frac{\partial}{\partial t}[Xe^*(^1P_1)] &= a \cdot ([(Ar_2^*)_s] + [(Ar_2^*)_s]) - (b+c) \cdot [Xe^*(^1P_1)] \\
\frac{\partial}{\partial t}[Xe^*(^3P_1)] &= c \cdot [Xe^*(^1P_1)] - (d+e) \cdot [Xe^*(^3P_1)] \\
\frac{\partial}{\partial t}[Xe_2^*] &= e \cdot [Xe^*(^3P_1)] - \frac{1}{\tau_{Xe}} \cdot [Xe_2^*].
\end{aligned}$$

The mathematical expression for the pulse shape has to take into account the contributions from all photon-emitting processes, so it can be written as a sum over 5 contributions. Each of these should be weighted with a number representing the relative efficiencies of the wavelength shifter at the wavelengths of the emitted photons, but this effect is neglected as well. The solution of the above system of linear equations is a lengthy expression and derived in appendix A on page 106. The effect of the wavelength shifter's decay time is also neglected there.

The pulse shapes with xenon concentration c1 were each fitted with the solution to the above system of equations. The variables τ_s, τ_t and R were only allowed to vary within 10% of the values obtained in the fit to the pulse shapes in pure argon (see table 6.1 on page 53). The value of τ_{Xe} was allowed to vary within 20% of the literature value of 20 ns [47]. All remaining parameters were merely restricted to physically meaningful values (i.e. they had to be larger than zero).

When trying to interpret the fit results, one has to keep in mind that there is no way to know for sure that the various steps in the reaction scheme actually involve the states and atoms quoted there. Several schemes can be thought up that lead to identical rate equations, but a different interpretation of the states and processes involved. Furthermore, the variables' values are all strongly coupled, so that fits do not converge to a stable global minimum. Therefore, the obtained values for variables a to e and A to D are not quoted. In order to show that the measured pulse shapes can in principle be fitted with the solution to the system of equations above, figure 7.10 shows the pulse shapes in xenon concentration c1 and their respective fit functions.

Figure 7.11 shows the fits to the gamma pulse shapes in 3 concentrations of xenon. The fit function behaves correctly by just varying the variables connected to energy transfer from argon to xenon.

It should be noted that, again, no scaling variables were used in the fit; the factors weighing the exponential functions that make the pulse shape were determined solely

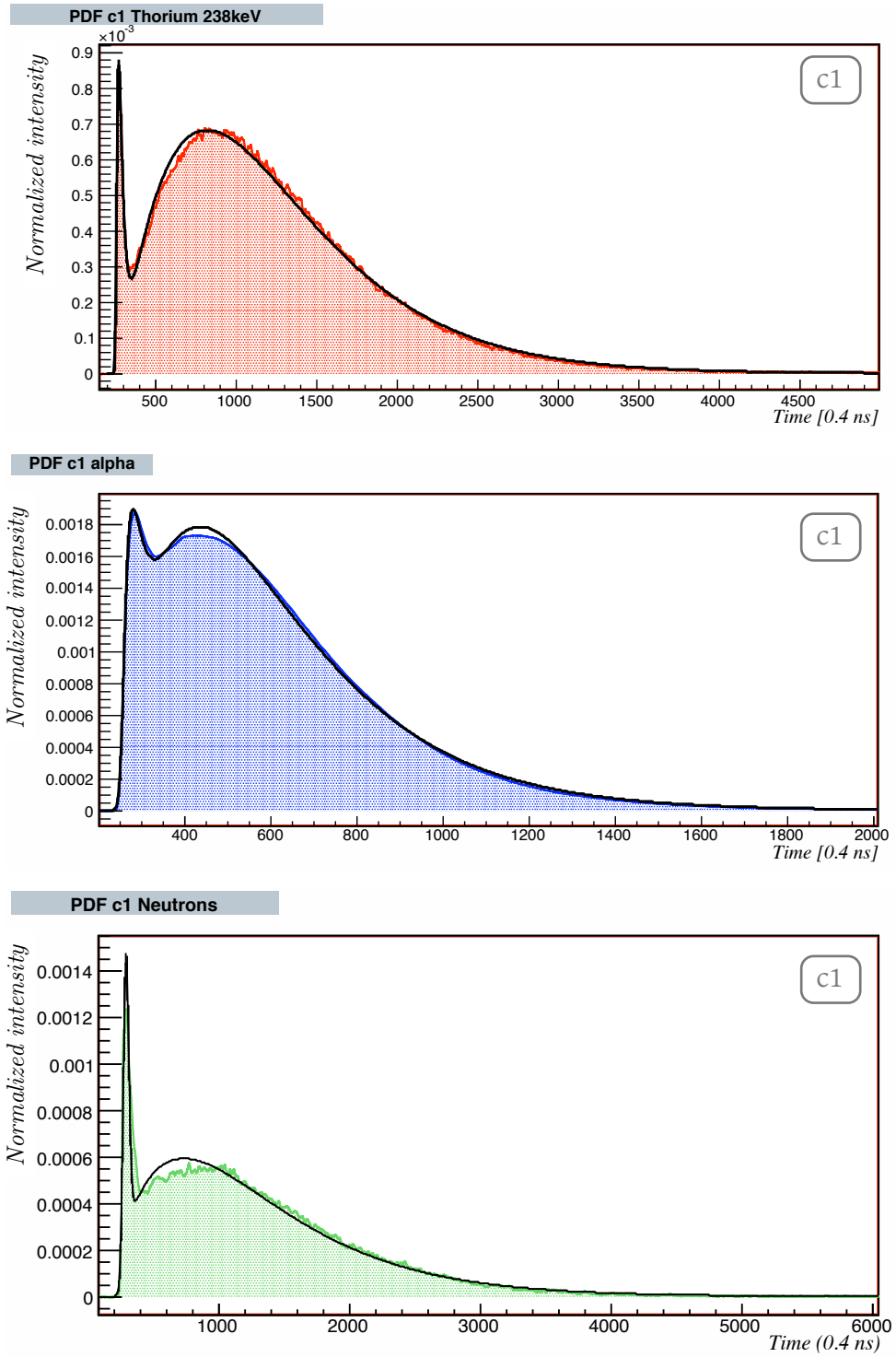

Figure 7.10: The fits to the gamma, alpha and neutron pulse shapes with xenon concentration c1. Mind that the axis ranges vary from plot to plot, they were chosen to best accommodate the pulse shapes, not for comparing the pulse shapes. For that refer to figure 7.7 on page 81.

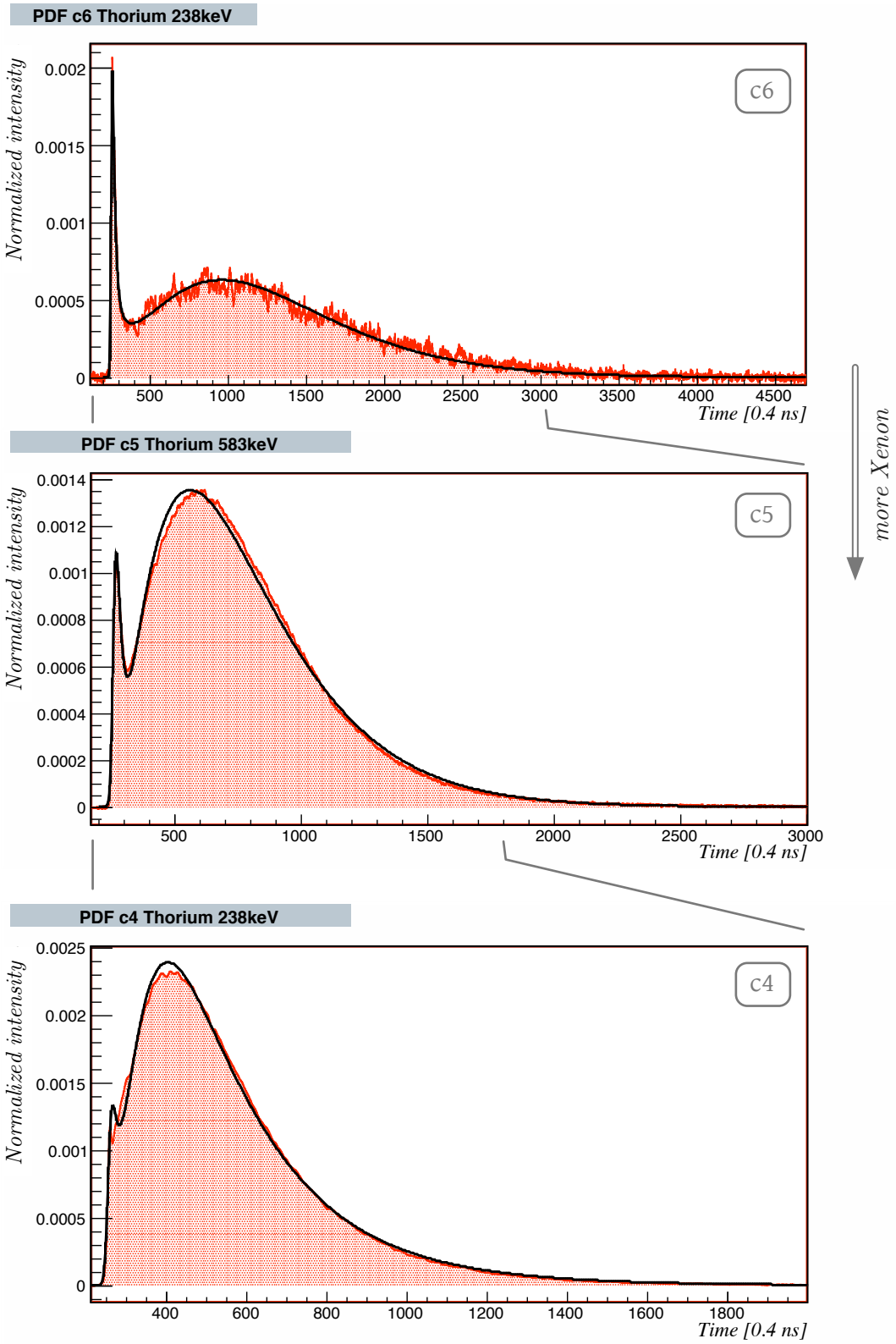

Figure 7.11: The fits of the gamma pulse shape at three concentrations of xenon.

from the solution of the rate equations. Therefore the correct behaviour of the model function with changing concentration and particle kinds shows that the assumptions which led to the model are adequate. The model function is not expected to fit the data so closely under more reasonable restrictions though. A global fit, for example, that would require certain sets of variables to stay constant over different concentrations and another set of variables to stay constant over the different particle kinds, would yield more realistic results at the prize of a worse congruency between model function and data.

With a global fit it would also be possible to make a stronger statement about the validity of the atomic states involved in the reaction scheme and their roles in the rate equations, especially if it was done with additional data sets in the very low (in the order of 10 ppm) and very high (in the order of 2%) xenon concentration range. With the simple separate fits used here, where only the basic variables known from the pure liquid argon pulse shape fit are fixed to a certain range, a process not actually important in a low concentration can make up for a neglected one that is actually present.

The degeneracy could be broken even more if it was possible to measure only the photons of a certain wavelength. The PDFs of the five decays involved could be measured and fitted separately, yielding information about which state of which atom contributes to what part of the pulse shape. A measurement of the emission spectrum would also prove useful, showing which states of which atoms are actually emitting scintillation light at a given xenon concentration. Such spectra have been measured, one was presented in figure 7.2 on page 70, but reproduction of the exact xenon concentrations at which the emission spectra were measured was not possible in the LArGe setup.

7.5 Spectra, scatterplots and discrimination power

The spectra of ^{222}Rn for the concentrations c1 and c2 are shown in figure 7.12. A clear increase in photo electron yield can be seen from c1 to c2, however that trend does not continue for concentrations c3 to c6. The following table summarizes the measured photo electron yields (as inferred from the position of the ^{241}Americium peak):

Concentration label	PE yield [PE/MeV]
c0	1243 ±20
c2	1771 ±27
c1	1678 ±27
c5	1391 ±22
c3	1340 ±22
c4	1338 ±22
c6	1307 ±21

They will be discussed in the next section.

The energy resolution, especially for c1 and c2, is improved due to the increased light yield. The 5.5 and 6.0 MeV alpha peaks are now resolved, unlike in the pure argon spectrum of figure 6.4 on page 58. The "fast to total" scatterplots that go with these spectra are shown in the same figure (bottom), together with the projections of the events in the shown energy range onto the discrimination parameter axis.

The scatterplots show a "shadow band" above the regular alpha band. The number of events in the shadow band increases with time as shown in figure 7.13 and at the same time the band becomes more and more detached from the alpha band, as can be seen in figure 7.14.

The distance parameters d (see eq. 6.23 on page 66) between the alpha and the gamma peak in the discrimination parameter plot for concentrations c2 and c5 depending on the time chosen for T_{cut} are summarized in table 7.5.

	T_{cut} [ns]					
d	32	40	48	60	80	88
c2	6.2	6.48	6.5	6.3	4.9	
c5	–	4.9	4.7	5.0	5.5	5.7

Table 7.5: The distance parameter between the alpha and the gamma peak in the "fast to total" discrimination plot for two concentrations of xenon and different choices of T_{cut}. There is a 5% error on each value. At 32 ns and concentration c5 there is no clear separation of the bands.

In figure 7.14 T_{cut} was chosen to be 40 ns so that it may be compared to figure 7.12. An equally good discrimination power can be reached with $T_{cut} = 48ns$, but this is only the case when considering gamma-alpha events. At higher choices of T_{cut} the gamma band becomes split into two parts as is shown in figure 7.15. Such a split was not observed in any data taken in pure argon and it cannot be seen in the actual gamma peak, but in the higher energy part of the band that is caused partially by cosmic muons. The wider gamma band is the reason for the loss in discrimination power.

The neutron-gamma discrimination was studied the same way as in the case of pure argon, overlaying data taken with the neutron source and data taken with the Americium gamma source. This is shown in figure 7.16. The split gamma band manifests itself again, this time it is clear where it comes from: The events from the Americium file, the vast majority of which are caused by the Americium's 60 keV gamma, form one peak, while the gamma-like background events from the AmBe neutron data form the other peak of the gamma band.

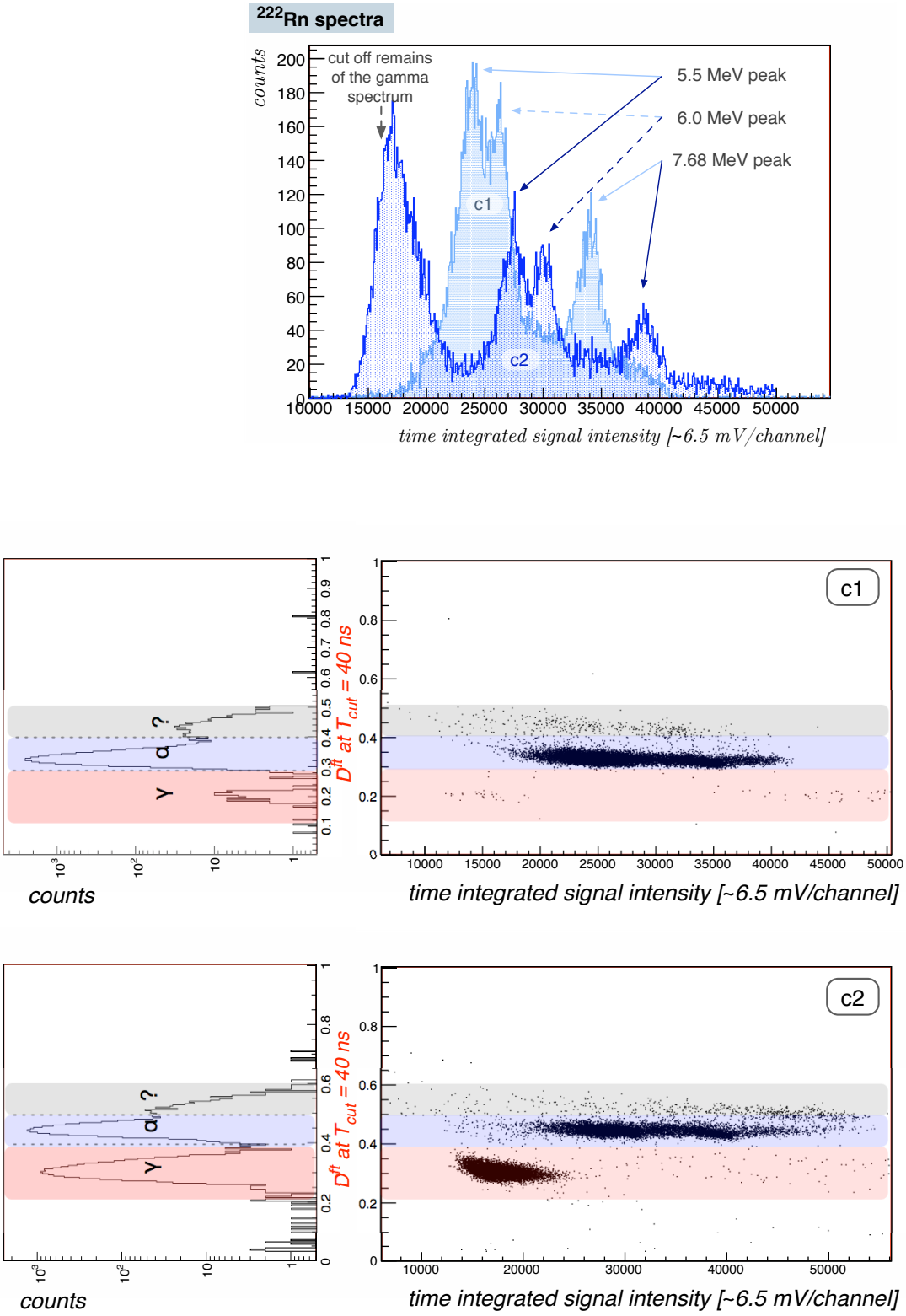

Figure 7.12: Top: ^{222}Rn spectra with xenon concentrations c1 and c2. Bottom: Scatterplots of the "fast to total" discrimination parameter against the energy of the event, and projection of all the events in the shown energy window onto the y-axis.

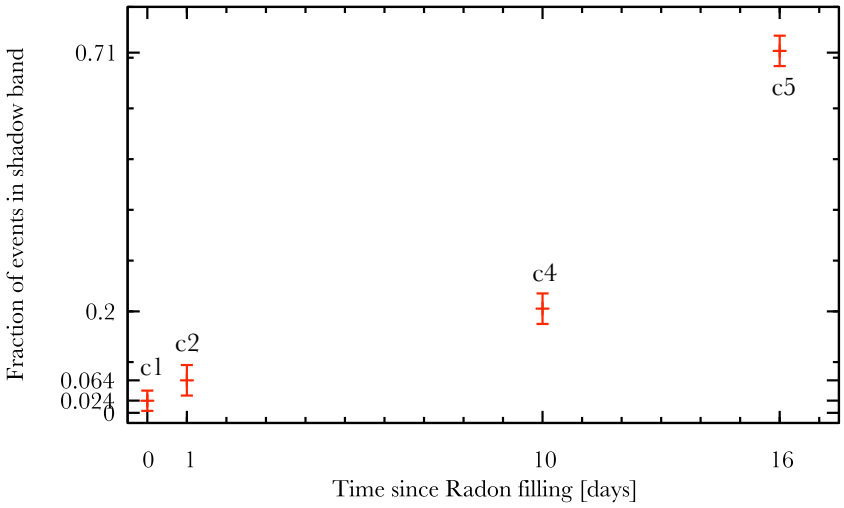

Figure 7.13: Fraction of events in the "shadow band" as it depends on the time passed after filling Radon into the system. The error bars reflect the uncertainty of the border position between the alpha and the shadow band.

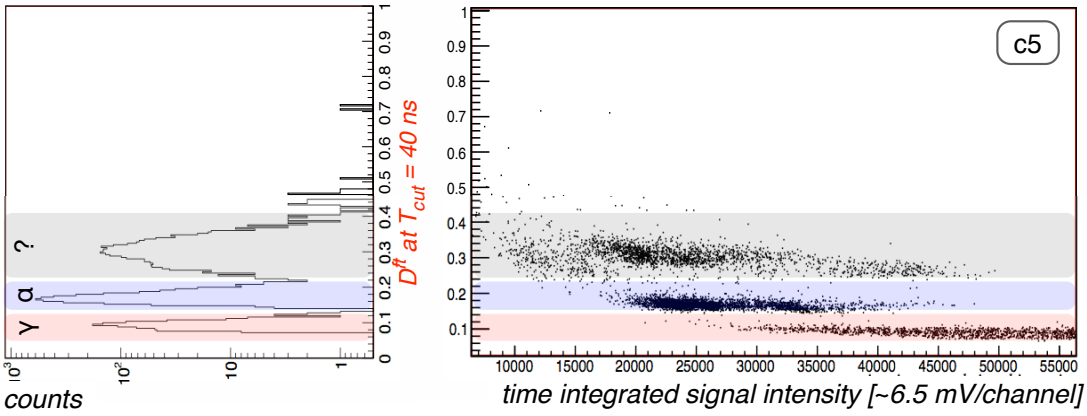

Figure 7.14: Scatterplot showing the gamma, alpha and "shadow" band at xenon concentration c5, where it is clearly more detached from the regular alpha band than at concentrations c1 or c2. Compare figure 7.12.

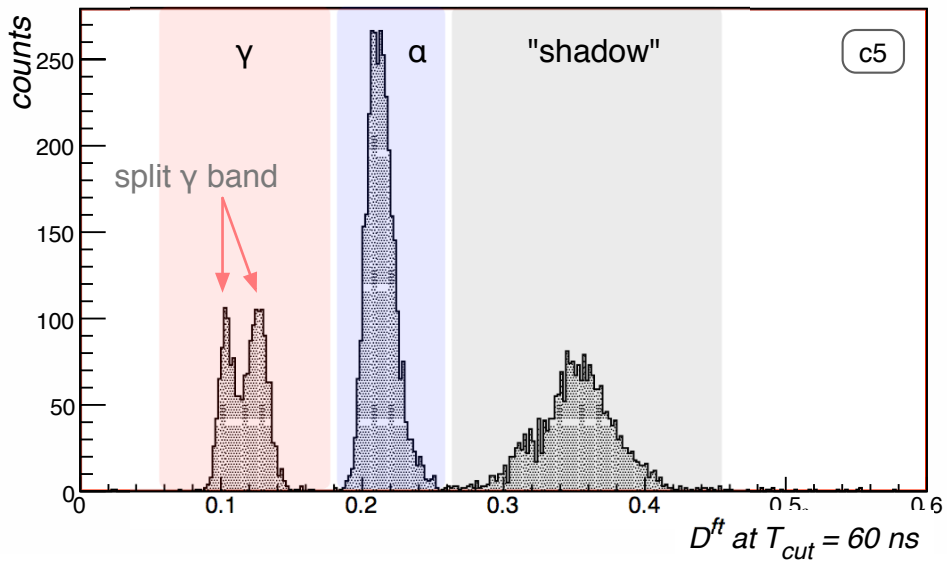

Figure 7.15: This projection onto the discrimination parameter axis at $T_{cut} = 60ns$ shows a split in the gamma band.

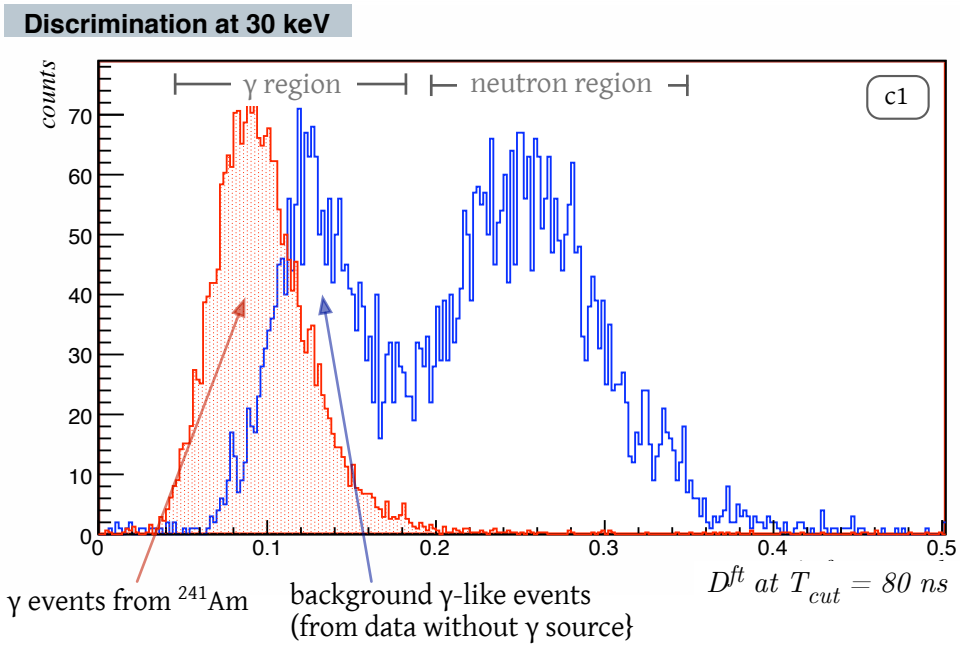

Figure 7.16: Data taken with the neutron source is in blue, data taken with the Americium gamma source is in red. The gamma-like events in the neutron data are background muons and photons; their peak is shifted with respect to the pure gamma event peak from the Americium data. (The Americium data peak is scaled down to fit into the plot.)

7.6 Discussion

7.6.1 Concentration dependence of the photo electron yield

One of the reasons the scintillation in xenon doped liquid argon was studied was the expected increase in photo electron yield. Such an increase could clearly be seen, its concentration dependence however deserves discussion, because taking the concentrations measured in the mass spectrometer as a reference, there seems to be no correlation whatsoever between the concentration and the light yield.

The results of the concentration measurement, despite the large uncertainties on them, certainly reflect the xenon concentration in the sample containers, but that concentration might not coincide the with actual xenon concentration in the Dewar at the time of data taking. Making some assumptions as to the continuity of the energy transfer processes discussed in section 7.4.2 on page 80, the most reliable indicator for the effective xenon concentration in the scintillator at the time of measurement is the shape of the recorded pulses, which should change continuously with the xenon concentration. One can further expect the pulse duration to become shorter with increasing xenon concentration, because more xenon means all energy transfer processes that involve xenon happen with a higher frequency. The order of xenon concentrations can then be inferred from figure 7.8: c6, c1, c5, c2, c4, c3. This does not coincide with the mass spectrometer measurement, where the order is c1, c2, c6, c5, c4, c3.Furthermore, the measured and the expected concentrations differ by a factor of up to 5.8 and their order is also not compatible.

The reason for this discrepancy is that the measured samples were taken from two different pipes which sampled from two different heights in the detector. This conclusion is reached the following way:

One would expect that the samples taken from pipe C are diluted because the pipe has an opening into the outer volume. Looking at table 7.6, which shows the expected and the measured concentrations for all samples again, the discrepancy could however not have been caused by a concentration difference between the inner and the outer argon volume. The concentrations taken from pipe C are considerably higher than those

concentration label	calculated concentration	measured concentration	factor	pipe
c1	88	< 90	$\sim$1	E
c2	352	297 $\pm$60	$\sim$1	E
c3	500-700	3341 $\pm$350	5.6	C
c4	250-350	1411 $\pm$126	4.7	C
c5	125 - 175	871 $\pm$110	5.8	C
c6	60 - 90	357 $\pm$160	4.8	C

Table 7.6: The concentrations calculated under the assumption that all xenon inserted into the system is dissolved in the argon of the active volume, the concentrations measured in the mass spectrometer, the factor by which they differ and the pipe through which the sample was taken.

taken from pipe E, and both are higher than the expected (calculated) concentrations.

Closer inspection of the expected and measured concentrations reveals that the factors by which they differ are approximately equal for those samples taken from the same pipe. Furthermore, the factor is bigger for the samples taken from pipe C at the bottom of the dewar than it is for those taken through pipe E from the center of the dewar.

A strong xenon concentration gradient towards the bottom of the dewar could be the explanation for those findings. Such a gradient would hardly be noticeable in gamma pulse shapes, because the gamma source is at a fixed position and the radiation does not travel very far in the detector[9] and can interact several times. The pulse shapes average over the concentrations in the radiation's reach; if some interact in an area with low and some in one with high concentration, or the same photon interacts several times in different parts of the detector, the pulse shapes in the end will be a mixture of light from one and from the other, so that they seem to come from an average concentration. A small difference between the gamma events from the Americium source and background gamma/muon events could indeed be observed.

Neutrons can undergo multiple scatterings in the detector and enter the detector at different positions, so that the "averaging out" effect hides a possible concentration gradient. The statistics achieved in the neutron measurements are anyway not good enough to make an effect apparent even if there were one.

In the case of alpha radiation, the situation is quite different. The ^{222}Ra is distributed throughout the argon, the interaction is point like and the statistics are good. An alpha particle emitted in a high concentration area will make a pulse that looks like a high xenon concentration pulse. An alpha particle emitted in a low concentration area will make a pulse that looks like a low xenon concentration pulse. If there are areas of different xenon concentration in the scintillator, then there will be different looking pulse shapes. And indeed, in the "fast to total" scatterplots there is a "shadow band" above the α-band. Such a band occurs in none of the data sets taken in pure argon[10].

[9] The mean free pathlength for 60 keV gammas is 1.7 cm, for 200 keV gammas it is 6.5 cm[29].

[10] In some data sets a certain number of events, but not quite a band, can be seen *below* the alpha band, these events can be attributed to degraded alphas from Radon daughters absorbed in the reflection

The shadow band is above the normal alpha band, indicating it has a stronger fast component. This is the case for pulse shapes from a higher xenon concentration. If xenon sinks to the bottom, then the same should be true for Radon, which is even heavier but present in a much smaller concentration so that the build up of a gradient will be slower. This has been observed during measurements of Radon in liquid Nitrogen[11]. This could explain the time dependence observed for the fraction of events in the shadow band, as seen in figure 7.13 on page 93. With time, more and more Radon sinks to the bottom of the Dewar where the xenon concentration is the highest, thus more pulse shapes with a strong fast component are produced.

The split in the gamma band is much harder to observe, because the separation is not very good and either the events from a source outweigh the background events by several orders of magnitude, or there are no source events at all. However, in figure 7.16 on page 94 the background events also appear above the regular gamma band, indicating they stem from an area of higher concentration. It is not conclusive whether the split in the band is actually due to two different particle kinds (muons and gammas) which interact differently with the argon-xenon mixture, or due to the suspected xenon concentration gradient.

foil.

[11] Dr. Grzegorz Zuzel, private communication.

Figure 7.16 on page 94 however shows only one band of gamma-like events, and many of those are certainly also from Americium gammas, just this time from outside of the detector[12], while all the gamma events from the internal source form a band around a smaller value of D^{ft}, leaving the concentration gradient theory as the more likely one. It should be mentioned though that the highest energy events from the internal Thorium source, which have a longer path in the liquid argon, form a peak which with the current statistics is congruent with the internal Americium one.

In summary:

- The concentration measurement done in the mass spectrometer does not reflect the true xenon concentration in the system, probably because of a strong concentration gradient towards the bottom of the Dewar.
- The calculated xenon concentrations are also not reliable because it is uncertain how the xenon is distributed and how much of the xenon was removed with each emptying cycle.
- The order of the average xenon concentrations can still be inferred by looking at the "averaging" gamma pulse shapes.

In the order of concentrations dictated by the order of the second peaks as well as the crossing times with the pure argon pulse shape, figures 7.17 and 7.18 depict the Thorium 84 keV γ-peak position in the spectrum and the fraction of the signal intensity within the first 300 ns. The intensity fraction plot reflects the reasoning that lead to this ordering of the concentrations: the fraction of the pulse's intensity in a fixed time slot rises continuously with the concentration. The reason the fraction is lower for the first concentration than it is in pure argon is just that the c6 pulse shape does not yet cross the pure argon pulse shape at 300 ns.

The light yield plot can be understood when keeping in mind the temporal order in which the measurements were done. The measurements c1 and c2 were first and both have a higher light yield than all the others. The remaining measurements have much lower light yields, even though the pulse shapes suggest they correspond to similar concentrations as c1 and c2. The xenon gas bottle was left connected to the system between c2 and c3, and not flushed again before filling to concentration c3. Ambient air probably entered the pipes and was flushed into the system, leading to strong quenching of the scintillation light.

An alternative explanation would be that the pulse shapes and light yields have a very erratic dependence on the xenon concentration. I find this unlikely, but further measurements with an improved determination of the xenon concentration are necessary to make a definitive statement. The behaviour of xenon in liquid argon could be studied

[12]Because the events are from an AmBe source positioned next to the detector, compare section 4.2 on page 35.

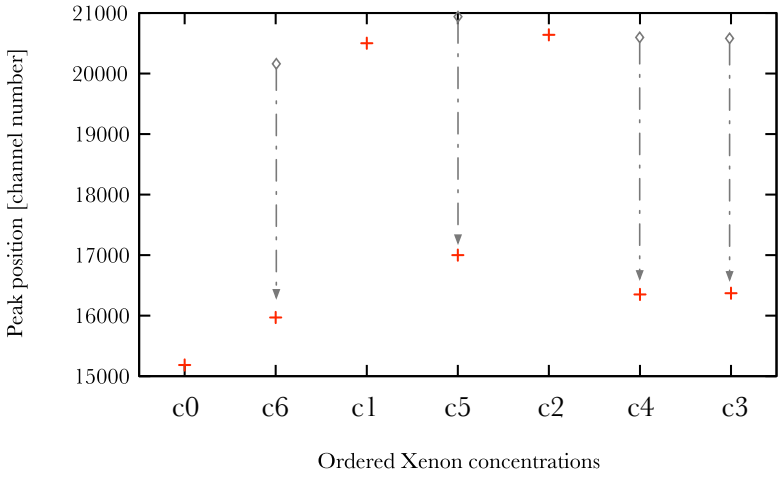

Figure 7.17: The position of the Thorium 84 keV gamma peak in the spectrum. All measurements done with xenon in the system show a peak at higher channel numbers than in pure liquid argon, indicating a higher photo electron yield. The relative positions of the data points are similar for the 60 keV Americium gamma peak. The serious drop in light yield from c2 to c3 and all subsequent concentrations can be explained by air entering the system during filling of xenon.

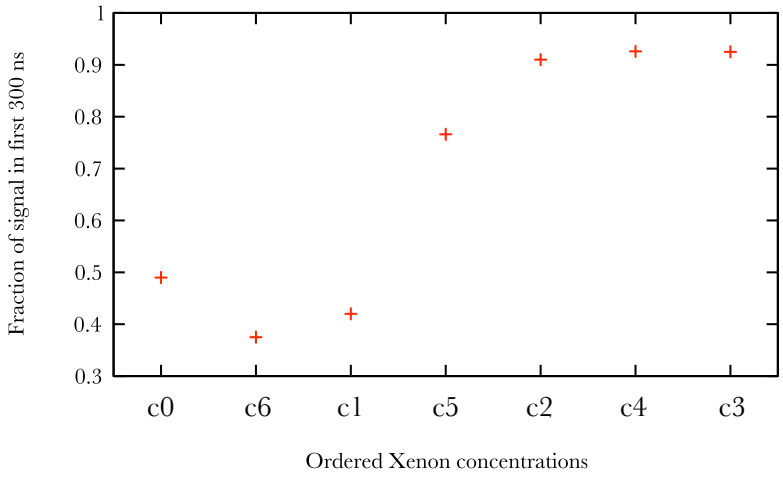

Figure 7.18: The fraction of the signal intensity in the first 300 ns. The order of concentrations follows the crossing times in figure 7.8.

by preparing such a mixture and taking samples from different heights over a time interval of two weeks. An online xenon concentration measurement would largely reduce the uncertainty involved with taking samples after taking data with a source in the system and storing the sample until concentration measurement in the mass spectrometer. For that, the mass spectrometer could be permanently connected to the system with a small flux of argon-xenon mixture flowing through it at all times.

7.6.2 Particle discrimination power

The argon-xenon data was evaluated only with the "fast to total" filter, because Gatti's filter is problematic to use here. With a split alpha and gamma band, finding ideal pulse shapes to calculate the weights is nearly impossible, at least if one is aiming for a better accuracy than the "fast to total" filter has.

The best discrimination between alpha and gamma events was reached with concentration c2 and $T_{cut} = 48ns$. Table 7.7 shows the distance parameter in pure argon (c0) and argon-xenon c2 again: The distance parameter is slightly bigger for c2, though

	c0		c2	
	α	γ	α	γ
μ	0.65	0.26	0.26	0.14
σ	0.036	0.0027	0.01	0.008
d	6.19 $\pm$0.1		6.5$\pm$0.2	

Table 7.7: Alpha-gamma discrimination with the "fast to total" filter in pure argon (c0) and xenon doped argon (c2).

within the respective errors they are nearly the same. This means that the pulse shapes having a higher similarity, which is detrimental to the discrimination power, is compensated by the higher light yield. Not only the overall higher light yield, but also the condensation of intensity into a few times the fast time intervall contributes to the better discrimination power by exponentiating the light yield gain in that time slot and thus leading to less statistical fluctuations in the region most important for the performance of the "fast to total" filter. Without the improved light yield a discrimination power comparable to that in pure argon cannot be reached even when with less xenon the pulse shapes keep more of their individual features, as can be seen for concentration c5 (compare table 7.5 on page 91).

Table 7.5 on page 91 also shows that the best choice of T_{cut} has to be found for each xenon concentration separately, though the very fact the pulse shapes change with the concentration points to the same conclusion already. If doped argon were to be used in an experiment, the xenon concentration would have to be kept perfectly constant over time and to ensure correct labelling of the events. In addition, a homogeneous xenon distribution would have to be ensured.

7.7 Summary

By doping the liquid argon with small amounts of xenon, the photo electron yield could be improved and the signal duration reduced, in accordance with what has been reported in literature. While the reduced signal duration is of advantage with regards to the dead time of the detector, and the increased light yield proved useful with regards to discrimination, the unification of the pulse shapes is critical. An ideal xenon concentration may be found where the increase in light yield and the unification of the pulse shapes are such to allow maximum discrimination power. More, and especially more exact, measurements are necessary to find it though.

Many effects that were observed in the xenon doped argon could not conclusively be explained with the data gathered, those are the "shadow band" above the alpha band, the split up of the gamma band, the unequal change in the pulse shapes of the three particle types studied with the xenon concentration, the contradictory measurements of the xenon concentration itself and, in connection to that, the photo electron yield behaviour. The measurements certainly could be improved using a setup constructed with pulse shape studies in doped liquid argon in mind.

Follow-up measurements are planned using a movable, point-like alpha-source to study the behaviour of the alpha and the "shadow" band. Such a measurement could decide the question whether the events that form the shadow band are from an area of higher xenon concentration or not. The question of the distribution of xenon certainly has to be answered before xenon doped argon can be considered for use as a detector medium.

It has been shown that a homogeneous and stable xenon concentration is crucial to the possibility of pulse shape discrimination, and that the assumption of a homogeneous xenon distribution needs to be validated.

Chapter 8

Conclusion

The goal of this work was to study how well discrimination between different kinds of ionizing radiation is possible using pulse shape discrimination in a liquid argon scintillator, to test two discrimination algorithms and to study the effects of xenon doping on the pulse shapes.

The best possible discrimination that could be reached, if it was possible to build an ideal detector, was determined from simulated pulses. This Monte Carlo simulation showed that it is in principle possible to reach a discrimination power between gamma-like and neutron-like events of 2.5 miss-identifications in 10^6 events for pulses of 70 detected photons with equal acceptance for both particle types. It was also shown that while keeping a discrimination power of 1 miss-identification in 10^6 gamma-like events it is possible to go down to pulses of 20 detected photons while losing only 40% of the neutron-like events. At the same 70 detected photons, the discrimination power at equal acceptance on both sides between alpha and gamma-like events is $2 \cdot 10^{-3}$.

The presence of ^{39}Ar requires the discrimination power to be good enough to place all events of its beta decay into the proper band, which is the gamma band here. The WIMP signal is expected to show in the neutron band, so that the gamma-neutron discrimination power is a good indicator for the background suppression that can be achieved. The simulation showed that with $1 \cdot 10^6$ decay events from ^{39}Ar in an energy window of 10 to 25 keV[1], the discrimination power reachable by pulse shape discrimination is good enough to recognise all of those events when at least $2 \cdot 10^3$ photons/MeV can be detected. The photo electron yield of the LArGe@MPI-K setup already approaches that number[1].

The study of the two discrimination algorithms showed that the Gatti filter preformes slightly better than the "fast to total" filter. However, it requires the sometimes difficult to get knowledge of the ideal pulse shapes. The "fast to total" filter is simple in its application and, in the case of the pulse shapes in liquid argon, very stable under slight variation of the fast time interval.

[1]The discrimination reached in LArGe however is not that good because of detector effects like noise and non-linearities in the recording of the pulse shape.

On the experimental side, the discrimination power between neutron and gamma induced events measured in the LArGe@MPI-K setup was two orders of magnitude worse than that simulated. However, the simulation takes into account only pulses of a fixed number of detected photons, while in the experiment pulses with a certain range of detected photons are used, so that the simulation gives an upper limit on the discrimination power[2]. The experimentally found discrimination power is only an upper limit as well, because the supposed gamma events in the neutron band could actually be neutron-induced ones. This demonstrates that even in a detector that was not built explicitly for studying pulse shapes, a reasonable discrimination power can be achieved.

The experimental alpha-gamma separation was so good that the peaks did not overlap. The alpha pulses consisted of more than 2500 photo electrons, while the simulation was done only up to 200 detected photons[3], so that a comparison with the simulation is not meaningful here.

The Gatti filter proved slightly superior in the discrimination of alpha and gamma events, but was problematic to use in the neutron and gamma discrimination where the onset of gamma events with less than 60 keV energy could not be determined precisely enough, demonstrating how important the knowledge of the right onset time is to this filter. Using a more powerful onset finding algorithm could probably solve the problem. The "fast to total" filter worked reliably on events over all energies used.

LArGe@MPI-K was successfully modified to allow xenon doping. Doping the liquid argon with xenon led to drastic changes in the pulse shapes and to interesting features in the discrimination parameter scatter-plots. The pulse shape changes could be motivated by considering energy transfer steps between the argon and the xenon atoms and fits to the pulse shapes showed that all shapes encountered with different xenon concentrations can be described by the theory developed. It was shown that, in a certain concentration range, the higher light yield makes up for the unification of the pulse shapes, so that the same or better discrimination power as in pure liquid argon can be reached. It was also shown that the unification of the pulse shapes goes so far that from about 200 ppm on the pulse shapes are so similar that the discrimination power becomes worse.

The additional features the discrimination parameter scatter-plots displayed, namely the "shadow band" close to the alpha band and the split in the gamma band, together with inconsistent results of concentration measurement and pulse shape evolution, suggest that the xenon did not become distributed homogeneously in the detector. If it turns out that no homogeneous distribution can be reached in a tank of this size, then xenon doped argon is out of the question as detector medium for most large-scale experiments.

More measurements are necessary to quantify the results of the argon-xenon studies. Especially the pulse shape fits could yield more relevant results about energy transfer processes with more data available. Even though xenon doped argon is a comparatively simple system of only two noble gas atoms, the energy transfer mechanisms are intricate

[2]Since a smaller value of the discrimination power is better, an upper limit means the discrimination power is better or equal to that quoted.

[3]One photo electron corresponds to one detected photon.

and deserve further studies. More exact and independent measurements should be done to clarify the xenon distribution in the system and more sophisticated methods should be used for filling xenon and for removing argon-xenon samples.

argon doped xenon could be a promising detector medium if the technical difficulties with achieving a homogeneous spacial distribution can be solved. A homogeneous distribution is not only crucial for doing pulse shape discrimination, but also when the light yield increase is a motivation for using xenon doped argon instead of pure argon in a calorimeter.

The experience gained through these investigations will be used in a second, larger LArGe setup that is being built in the Gran Sasso underground laboratory to gain more experience with the operation of bare germanium crystals in liquid argon. Pulse shape analysis of the liquid argon scintillation signals will be used there to diagnose and study sources of background and the interaction of argon as well as fission fragment ions with the germanium crystals. Possible sources of background identified there can then be avoided in the GERDA setup.

Acknowledgements

I would like to thank Prof. Wolfgang Hampel for accepting me as a diploma student and for the cordial introduction to the neutrino group at MPI-K, my thesis adviser Dr. Stefan Schönert for giving me the chance to study such an interesting subject and for valuable advice given many times, Dr. Peter Peiffer for patiently explaining to me the intricacies of the LArGe setup, for joint efforts on data collection and evaluation and for many stimulating discussions, Sergei Vasiliev for introducing me to the ROOT frameworks and for many discussions about detector effects, Anatoly Smolnikov for helping me improve the scientific validity of the data plots and insisting on the importance of correct and meaningful labelling, Dr. Grzegorz Zuzel for setting up the mass spectrometer and taking so much time troubleshooting and showing me how to operate it, Oleg Chkvorets for helpful discussions and Adam Diehl for proofreading.

Appendix A

Equation for the pulse shapes in Xenon doped Argon

The rate equations can be written in the following way:

$$\frac{d}{dt}\overrightarrow{N}(t) = \begin{pmatrix} \lambda_1 & 0 & 0 & 0 & 0 \\ 0 & \lambda_2 & 0 & 0 & 0 \\ a & a & \lambda_3 & 0 & 0 \\ 0 & 0 & c & \lambda_4 & 0 \\ 0 & 0 & 0 & e & \lambda_5 \end{pmatrix} \cdot \overrightarrow{N}(t) \tag{A.1}$$

with

$$\overrightarrow{N}(t) = \begin{pmatrix} [(Ar_2^*)_s] \\ [(Ar_2^*)_t] \\ [Xe^*]({}^1P_1) \\ [Xe^*]({}^3P_1) \\ [Xe_2^*] \end{pmatrix} \tag{A.2}$$

and with the eigenvalues

$$\lambda_1 = -(\frac{1}{\tau_s} + a) \tag{A.3}$$

$$\lambda_2 = -(\frac{1}{\tau_t} + a) \tag{A.4}$$

$$\lambda_3 = -(b + c) \tag{A.5}$$

$$\lambda_4 = -(d + e) \tag{A.6}$$

$$\lambda_5 = -\frac{1}{\tau_{Xe}} \tag{A.7}$$

Then the components of the eigenvectors to each of these are

$$\begin{array}{lllll}
\sigma_{11}=1 & \sigma_{21}=0 & \sigma_{31}=0 & & \\
\sigma_{12}=0 & \sigma_{22}=1 & \sigma_{32}=0 & & \\
\sigma_{13}=\frac{a}{\lambda_1-\lambda_3} & \sigma_{23}=\frac{a}{\lambda_2-\lambda_3} & \sigma_{33}=1 & & \\
\sigma_{14}=\frac{c\cdot\sigma_{13}}{\lambda_1-\lambda_4} & \sigma_{24}=\frac{c\cdot\sigma_{23}}{\lambda_2-\lambda_4} & \sigma_{34}=\frac{c}{\lambda_3-\lambda_4} & \sigma_{44}=1 & \\
\sigma_{15}=\frac{e\cdot\sigma_{14}}{\lambda_1-\lambda_5} & \sigma_{25}=\frac{e\cdot\sigma_{24}}{\lambda_2-\lambda_5} & \sigma_{35}=\frac{e\cdot\sigma_{34}}{\lambda_3-\lambda_5} & \sigma_{45}=\frac{e}{\lambda_4-\lambda_5} & \sigma_{55}=1
\end{array}$$

Where σ_{mn} is the nth component of the eigenvector to λ_m.

The general solution to equation A.1 is

$$\overrightarrow{N}(t)=\sum_{i=1}^{5} n_i\cdot\overrightarrow{\sigma_i}\cdot e^{\lambda_i t} \tag{A.8}$$

and the n_i are normalizing factors which using the initial conditions

$$\overrightarrow{N}(t=0)=\big[A,B,C,D,0\big] \tag{A.9}$$

$$\frac{A}{B}=R \tag{A.10}$$

$$A+B+C+D=1 \tag{A.11}$$

can be determined as

$$\begin{aligned}
n_1&=R\cdot B\\
n_2&=B\\
n_3&=C-(n_1\cdot\sigma_{13}+n_2\cdot\sigma_{23})\\
n_4&=(R+1)\cdot B-C-(n_1\cdot\sigma_{14}+n_2\cdot\sigma_{24}+n_3\cdot\sigma_{34})\\
n_5&=-(n_1\cdot\sigma_{15}+n_2\cdot\sigma_{25}+n_3\cdot\sigma_{35}+n_4\cdot\sigma_{45})
\end{aligned}$$

Equation A.8 contains the information about the behaviour in time of the number density of all five components involved. Each one of them can decay under photon emission, so that they all contribute to the final photon PDF (or photon-intensity function[1]).

If the only reduction of the number density of a given component is through radiative decay then the photon PDF is the negative of the differential with respect to time of the number-density function, because every time the number density decreases, a photon is emitted. For an exponential decay with lifetime $\lambda=1/\tau$, the number-density function is

$$N(t)=N(t=0)\cdot e^{-\lambda\cdot t} \tag{A.12}$$

so the light-intensity function becomes

$$I(t)=N_0\lambda\cdot e^{-\lambda\cdot t} \tag{A.13}$$

[1]The photon-intensity function here is equal to the PDF, because through condition A.11 it is already normalized.

However, several of the number-density functions from equation A.8 are of the form

$$N(t) = N_0 \cdot e^{-(p+q)\cdot t} \tag{A.14}$$

with the rate q associated with radiative decay and the rate p associated with another number-density reducing process. Effectively, this means that N_0 is not constant in time, but decreases as the competitive process reduces the number of states available to decay radiatively.[2] The number-density function can be re-written as

$$N(t) = N_0' \cdot e^{-q\cdot t} \tag{A.15}$$

with

$$N_0' = N_0 \cdot e^{-p\cdot t}. \tag{A.16}$$

Since the intensity function is only concerned with the radiative decay, the time derivative may be taken under the assumption that N_0' is constant, so

$$I(t) = N_0 \cdot e^{-p\cdot t} \cdot q \cdot e^{-q\cdot t} \tag{A.17}$$

$$= N_0 \cdot q \cdot e^{-(p+q)\cdot t} \tag{A.18}$$

The desired photon PDF is the sum over the intensities each component contributes. The contribution of Xe_2^* for example is

$$I_{Xe_2^*} = \frac{1}{\tau_{Xe}} \cdot n_5 \cdot e^{\lambda_5 \cdot t}$$

and the contribution of $Xe^*(^1P_1)$ is

$$I_{Xe^*(^1P_1)} = b(n_1\sigma_{13}e^{\lambda_1 t} + n_2\sigma_{23}e^{\lambda_2 t} + n_3 e^{\lambda_3 t})$$

The final result for the photon PDF, sorted by exponentials to make the convolution with the gaussian apparatus function more convenient, is then

$$\begin{aligned} I(t) = &(\frac{n_1}{\tau_s} + bn_1\sigma_{13} + dn_1\sigma_{14} + \frac{n_1}{\tau_{Xe}}\sigma_{15})\ e^{\lambda_1 t} \\ &+ (\frac{n_2}{\tau_t} + bn_2\sigma_{23} + dn_2\sigma_{24} + \frac{n_2}{\tau_{Xe}}\sigma_{25})\ e^{\lambda_2 t} \\ &+ (bn_3 + dn_3\sigma_{34} + \frac{n_3}{\tau_{Xe}}\sigma_{35})\ e^{\lambda_3 t} \\ &+ (dn_4 + \frac{n_4}{\tau_{Xe}}\sigma_{45})\ e^{\lambda_4 t} \\ &+ \frac{n_5}{\tau_{Xe}}\ e^{\lambda_5 t} \end{aligned} \tag{A.19}$$

[2] Such a situation is well known from chemical rate equations when one kind of atom can, for example, form several kinds of molecules. The solutions, that is the the number density functions of each component, are well known. Here, however, the function of interest is the photon-intensity, not the number-density, warranting the elaboration on the solution.

The above function may be written as

$$I(t) = \sum_{i=0}^{5} a_i \, e^{\lambda_i t} \tag{A.20}$$

when the a_i are the expression in the brackets in front of the exponentials.

Convolution with a gaussian function leads to

$$I^{exp}(t) = \frac{1}{2} \sum_{i=0}^{5} a_i \, e^{(\frac{\lambda_i^2}{4h^2} - \lambda_i t)} \cdot [1 - erf(\frac{\lambda_i}{2h} - ht)] \tag{A.21}$$

with $h^2 = 1/(2\sigma^2)$ and σ the standard deviation, meaning here the time spread of the photo electrons. This is the function used for the fits.

Bibliography

[1] M.G. Boulay, A. Hime, *"Direct WIMP detection using scintillation time discrimination in liquid Argon"*, arXiv:astro-ph/0411358v1 (2004).

[2] M. Laffranchi, A. Rubbia, *"The ArDM project: a Liquid Argon TPC for Dark Matter Detection"*, J.o.P. Vol. 65 (2007).

[3] S. R. Elliot, P. Vogel, *"Double Beta Decay"*, Annu. Rev. Nucl. Part.Sci. Vol. 52:115–51 (2002).

[4] Timothy J. Sumner, *"Experimental Searches for Dark Matter"*, Living Rev. Relativity 5 URL: http://www.livingreviews.org/lrr-2002-4(retrieved on Sept. 4 2007) (2002).

[5] L.M.Krauss, *"Dark Matter candidates: What's Cold, .. and What's Not"*, arXiv:hep-ph/07020051v1 (2007).

[6] H.H. Loosli, *"A dating method with ^{39}Ar"*, Earth and Planetary Science Letters Vol. 63 pp. 51-62 (1983).

[7] A. McDonald, S. Schoenert et al., *"Astrophysical Neutrino Telescopes"*, Rev.Sci.Instrum.75:293-316 (2004).

[8] Y. Ramachers, *"WIMP direct detection overview"*, arXiv:astro-ph/0211500v1 (2002).

[9] J.A.Peacok, *"Cosmological Physics"*, Cambridge University Press (1999).

[10] S. Goswami, *"Solar neutrino experiments - an overview"*, Proc Indian Natn Sci Acad, 70, A, No. 1 (2004).

[11] N. Ferrari, *"WARP: a double phase argon programme for dark matter detection"*, J.o.P. Vol. 39 pp.111-113 (2006).

[12] D. N. Spergel, et al., *"Wilkinson Microwave Anisotropy Probe (WMAP) Three Year Observations: Implications for Cosmology"*, arXiv:astro-ph/0603449v2 (2007).

[13] XENON Collaboration, *"XENON: a 1 tonne Liquid Xenon Experiment for a Sensitive Dark Matter Search"*, arXiv:astro-ph/0407575 (2002).

[14] K. Zuber, *"Neutrino Physics"*, IoP Series in High Energy Physics, Cosmology and Gravitation (2004).

[15] GERDA collaboration, *"The GERmanium Detector Array (Gerda) for the search of neutrinoless $\beta\beta$ decays of ^{76}Ge at LNGS"*, Nucl.Phy. B (Proc. Suppl.) V145 pp.242–245 (2005).

[16] H.V. Klapdor-Kleingrothaus, A. Dietz et al., *"Latest results from the HEIDELBERG-MOSCOW double beta decay experiment"*, Eur. Phys. J. A 12, 147–154 (2001).

[17] R. N. Mohapatra, P. B. Pal, *"Massive Neutrinos in Physics and Astrophysics"*, World Scientific Lecture Notes in Physics Vol.72 (2004).

[18] C. Brassard, *"Liquid ionization detectors"*, Nucl. Instr. Meth. V162 pp.29-47 (1979).

[19] N.H. Gale, *"Lifetimes of the first excited states of B^{10}, O^{14} and $F17$ - Analysis of delayed coincidence lifetime measurements"*, Nucl. Phys. V.38 pp.252-258 (1962).

[20] C.R. Gruhn, M.D. Edmiston, *"Geminate Recombination of α-Particle-Excited Carriers in Liquid Argon"*, Phys. Rev. Lett. Vol.40 No.6 p.407 (1978).

[21] N. Ishida, et.al., *"Attenuation length measurements of scintillation light in liquid rare gases"*, Nucl. Instr. Meth. A384 pp.380-386 (1997).

[22] S. Kubota et. al., *"Dynamical behavior of free electrons in the recombination process in liquid argon, krypton and xenon"*, Phys. Rev. B V.20 No.8 (1979).

[23] R.S. Mulliken, *"Potential curves of diatomic rare-gas molecules and their ions"*, J. Chem. Phys. V.52 No.10 (1970).

[24] E. Shibamura et al., *"Drift velocities of electrons, satuaration characteristics of ionization and W-values for conversion electrons in liquid Argon, liquid Argon-gas mixtures and liquid Xenon"*, Nucl. Instr. Meth. 131 pp. 249-258 (1975).

[25] G.M. Seidel, R.E. Lanou, W. Yao, *"Rayleigh scattering in rare-gas liquids"*, Nucl. Instr. Meth. A489 pp.189-194 (2002).

[26] U. Sowada, J. Warman, M. de Haas, *"Hot-electron thermalization in solid and liquid argon, krypton and xenon"*, Phys Rev B Vol.25 No.5 (1982).

[27] M. Miyajima, T. Takahashi et.al., *"Average energy expended per ion pair in liquid argon"*, Phys. Rev. A V9 No.3 (1974).

[28] J. Thomas, D.A. Imel, *"Recombination of electron-ion pairs in liquid argon and liquid xenon"*, Phys Rev A V.36 No. 2 (1987).

[29] *"The NIST physics database/Photon cross sections"*, http://www.physics.nist.gov/cgi-bin/Xcom/xcom2 Retrieved: October 2007.

[30] W.Gornik, S.Kindt, E. Matthias, D. Schmidt, *"Two-photon excitations of xenon atoms and dimers in the energy region of the $5p^5 6p$ configuration"*, J. Chem. Phys. Vol.75 No.68 (1981).

[31] *"The NIST physics database."*, http://physics.nist.gov/PhysRefData/Handbook/Tables/xenontable5.htm Retrieved: August 2007.

[32] R. Brodmann, G. Zimmerer, *"Xenon 5d emission in pure Xenon and Xenon doped Argon"*, Chem phys Lett V56 No3 p.434 (1978).

[33] E. Conti, G. Carugo, A. Intravaia, *"Time behaviour of the scintillation light in mixtures of liquid argon and xenon"*, Nucl. Instr. Meth. A382 pp.475-478 (1996).

[34] O. Cheshnovsky, B. Raz, J. Jortner, *"Emission Spectra of Deep Impurity States in Solid and Liquid Rare Gas Alloys"*, J. Chem.Phys. V.57 No.11 (1972).

[35] S. Kubota, M. Hishida et.al., *"The suppression of the slow component in xenon-doped liquid argon scintillation"*, Nucl. Instr. Meth. A327 p.71 (1993).

[36] P. Laporte et.al, *"Xenon luminescence in high pressure argon: spectroscopy and kinetics"*, Chem. Phys. Vol. 177 pp. 257-269 (1993).

[37] M. Suzuki, M. Hishida, J. Ruan(Gen), S. Kubota, *"Light output and collected charge in xenon-doped liquid argon"*, Nucl. Instr. Meth. A327 67-70 (1993).

[38] G. Baldini, *"Ultraviolet Absorption of Solid Argon, Krypton and Xenon"*, Phys. Rev. V128 No.4 p.1562 (1962).

[39] G. Baldini, *"Trapped Excitons in Dilute Rare-Gas Alloys"*, Phys. Rev. V137 No.2A p.508 (1965).

[40] O. Cheshnovsky, B. Raz, J. Jortner, *"Temperature dependence of rare gas molecular emission in the vacuum ultraviolet"*, Chem. Phys. Lett. V.15 No.4 (1972).

[41] A. Gedanken et.al., *"Electronic energy transfer phenomena in rare gases"*, J. Chem. Phys. V.57 No. 8 (1972).

[42] M. Suzuki, S. Kubota, *"Mechanism of proportional scintillation in Argon, Krypton and Xenon "*, Nucl. Instr. Meth. V164 pp197-199 (1979).

[43] N. Thonnard, G.S. Hurst, *"Time-dependent study of vacuum-ultraviolet emission in Argon"*, Phys. Rev. A V.5 No. 3 (1972).

[44] D. Beaglehole, *"Reflection studies of excitons in liquid and solid Xenon"*, Phys. Rev. Lett. V.15 No.13 p.551 (1965).

[45] S. Kubota, A. Nakamoto et.al., *"Evidence of the existence of exciton states in liquid argon and exciton-enhanced ionization from xenon doping"*, Phys Rev B V13 No.4 (1976).

[46] S. Kubota, M. Hishida and J.Raun(Gen), *"Evidence for a triplet state of the self-trapped exciton states in liquid argon, krypton and xenon"*, J. Phys. C V.11 (1978).

[47] P. Laporte et al., *"Argon, Krypton and Xenon excimer luminescence: From the dilute gas to the condensed phase"*, J. Chem. Phys. V.91 No. 3 (1989).

[48] E. Morikawa et. al., *"Argon, krypton and xenon excimer luminescence: From the dilute gas to the condensed phase"*, J. Chem. Phys V. 91 No. 3 (1989).

[49] E.S. Peterson, B. J. Schwartz, C.B. Harris, *"The dynamics of exciton tunneling and trapping in condensed xenon on ulstrafast time scales"*, J. Chem. Phys. 99 (3) (1993).

[50] S. Rice, J. Jortner, *"Do exciton states exist in the liquid phase?"*, J. Chem. Phys. V.44 No. 12 p. 4470 (1966).

[51] B. Raz, J. Jortner, *"Wannier type impurity excited states in liquid rare gases "*, Chem. Phys. Lett. V.4 No.8 p.511 (1970).

[52] L. Resca, R. Resta, S. Rodriguez, *"Nonstructural theory of exciton states in solid rare gases"*, Phys Rev B Vol18 No2 (1978).

[53] N. Schwentner, E.-E. Koch, J. Jortner, *"Electronic Excitations in Condensed Rare Gases"*, Springer Tracts in Modern Physics 107 (1985).

[54] T. Doke, H. Crawford et.al., *"LET dependence of scintillation yields in liquid Argon"*, Nucl. Instr. Meth. A269 pp.291-296 (1988).

[55] T. Doke, A. Hitachi, et.al., *"Absolute Scintillation Yields in Liquid Argon and Xenon for Various Particles"*, Jpn. J. Appl. Phys. Vol. 41 pp.1538-1545 (2002).

[56] A. Hitachi, T. Doke, A. Mozumder, *"Luminescence quenching in liquid argon under charged-particle impact: Relative scintillation yield at different linear energy transfers"*, Phys Rev B, Vol. 46 No. 18 p. 11463 (1992).

[57] A. Hitachi, et al., *"Effect of ionization density on the time dependence of luminescence from liquid argon and xenon"*, Phys Rev B Vol27 No.9 (1983).

[58] A. Hitachi, T. Takahashi et al., *"Effect of ionization density on the time dependence of luminescence from liquid argon and xenon"*, Phys Rev B V27 No.9 (1983).

[59] S. Kubota, et.al., *"Liquid and solid Argon, Krypton and Xenon scintillators"*, Nucl Instr. Meth Vol.196 pp.101-105 (1982).

[60] M. Miyajima, T. Takahashi et al., *"A self-triggered liquid xenon drift chamber by the use of proportional ionization or proportional scintillation "*, Nucl. Instr. Meth. V.160 p.239 (1979).

[61] D.F. Muller et al., *"Nonlinear excitation of rare-gas liquid mixtures in the ultraviolet"*, Phys. Rev. A Vol. 25 No. 2 p.1004 (1982).

[62] E. Gatti, F. Martini, *"A new linear method of discrimination between elementary particles in scintillation counters"*, Nucl. Electr. Vol.2 pp. 265-276, IAEA Vienna (1962).

[63] J.P. Peiffer, *"Liquid argon as active shielding and coolant for bare germanium detectors: A novel background suppression method for the GERDA $0\nu\beta\beta$ experiment"*, PhD Thesis at the University of Heidelberg (2007).

[64] D.G. Motta, *"Feasibility analysis of prototype measurements of a novel approach for real-time spectroscopy of low energy solar neutrinos"*, PhD Thesis at the University of Heidelberg (2004).